

The background is a vibrant blue. In the upper right, there is a large, semi-transparent circular graphic composed of several concentric rings. The outermost ring features a series of small, light-blue circles. Below this graphic, the text 'III-2' is prominently displayed in a large, white, serif font. Underneath the main title, the words 'Materials Sciences' are written in a smaller, white, sans-serif font. The bottom half of the page is filled with a fine, light-blue dot pattern that creates a textured effect.

# III-2

Materials Sciences



BL7U

## Electron-Phonon Coupling Investigation in Highly Oriented Pyrolytic Graphite by Angle-Resolved Photoelectron Spectroscopy

S. Tanaka<sup>1</sup>, M. Matsunami<sup>2,3</sup> and S. Kimura<sup>2,3,4</sup>

<sup>1</sup>The Institute of Scientific and Industrial Research, Osaka University, Ibaraki 567-0047, Japan.

<sup>2</sup>UVSOR Facility, Institute for Molecular Science, Okazaki 444-8585, Japan.

<sup>3</sup>School of Physical Sciences, The Graduate University for Advanced Studies (SOKENDAI), Okazaki 444-8585, Japan.

<sup>4</sup>Graduate School of Frontier Biosciences, and Department of Physics, Osaka University, Suita 565-0871, Japan.

Electron-phonon coupling (EPC) plays an important role in solid state physics. The EPC has been analyzed via the self-energy  $\Sigma^{el-ph}(E, T)$  in the quasiparticle spectral function, which is determined with the integral of the Eliashberg function  $\alpha^2 F(\hbar\omega, q)$  with the energy and momentum of the phonon, by using the angle-resolved photoelectron spectroscopy (ARPES). Here, we demonstrate an experimental method in which the elemental process of EPC, that is a scattering of the electron by the phonon in the solid, can be investigated [1].

Figure 1(a) presents a series of surface-normal ( $\pm 5^\circ$ ) photoelectron spectra for HOPG (highly oriented pyrolytic graphite) at 50 K in the region near the Fermi level with several photon energies ( $h\nu$ ). The feature that we focus on here is the step-like edges located at either 154 meV or 67 meV with respect to the Fermi level, those are clearly demonstrated by the differentials of the photoelectron intensity with the binding energy along with that of a gold film as shown in Fig. 1(b). The  $\pi$ -band of the graphite crosses the Fermi level at the K(H) point, and no electronic states are located near the Fermi level at the  $\Gamma$ (A) point, that is observed in the present spectra. We therefore conclude that the observed electron emission is due to EPC and that the energy of the step matches the energy of the phonon that is involved. The 154- and 67-meV steps are ascribed to the transverse optical (TO), and the out-of-plane acoustic (ZA) and/or out-of-plane optical (ZO) phonon of graphite at the K(H)-point, respectively. Figure 1(c) plots the intensities of the steps at 154 and 67 meV in the surface-normal photoelectron spectra as a function of the photon energy. These intensities represent the electron-scattering intensities from K(H) to  $\Gamma$ (A) by the phonons at the K(H) point in the Brillouin zone. The black (red) solid line is the Lorentzian curve, where the center and width energies are 11.05 and 0.92 eV (6.0 and 1.2 eV), respectively. This  $h\nu$ -dependence indicates that the final photoexcitation state is definitely defined by the photon energy and that this state determines the phonon branch that can scatter the electron. Note that this photon-energy dependence clearly demonstrates that we are observing EPC among the electrons in bands of the solid. The photoexcitation process that

accompanies electron-phonon scattering is widely known as the “indirect transition” that is often observed in semiconductor materials.

The transition probabilities of the indirect transition can be formulated as

$$W_{0,k \rightarrow f,k'} = \frac{2\pi}{\hbar} \frac{\langle f, k' | \hat{H}_{EPC} | i, k \rangle \langle i, k | e \cdot \hat{A} | 0, k \rangle^2}{(\hbar\omega_i - \hbar\omega)^2} \delta(\hbar\omega - \hbar\omega_{0f} - \hbar\omega_s) + \frac{2\pi}{\hbar} \frac{\langle f, k' | e \cdot \hat{A} | i', k' \rangle \langle i', k' | \hat{H}_{EPC} | 0, k \rangle^2}{(\hbar\omega_{i'f} - \hbar\omega)^2} \delta(\hbar\omega - \hbar\omega_{0f} - \hbar\omega_s)$$

where the matrix elements of the optical transition and EPC among the electronic bands in graphite are included. This is the first measurement of the matrix elements of the EPC by ARPES. Additional insights about electron-phonon scattering in the solid will be gained from further research using this method. A comparison with the results of theoretical calculations of the intensity of the electron-phonon interaction while resolving the energy and momentum of all the contributing electronic states and phonons will lead to deeper insight into EPC in solids.

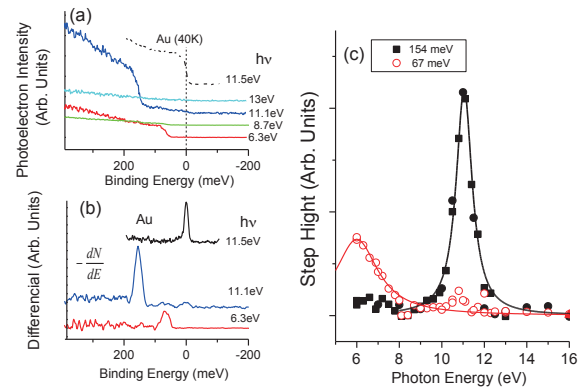


Fig. 1. (a) Surface-normal photoelectron spectra of graphite at 50K. (b) Differentials of photoelectron intensity with the binding energy. (c) Height of the steps observed in the photoelectron spectra as a function of the photon energy.

[1] S. Tanaka, M. Matsunami, and S. Kimura, *Sci. Rep.* 3, 3031; DOI:10.1038/srep03031 (2013).

BL1B

## Experimental Study of Electronic States on Solids Using THz Beamline

A. Irizawa

*The Institute of Science and Industrial Research, Osaka University, Ibaraki 567-0047, Japan*

The optical study is one of the most powerful techniques for the investigation of electronic states on solids. There can be obtained the great deal of information about the electronic band structure, the symmetry of crystal structure, and the dielectric property. In the respect of experimental affinity, the optical study is extremely compatible with the multiple conditions such as low temperature, high magnetic field, and high pressure. In the case of strongly correlated electron systems, it is well known that the temperature is one of the decisive factors for the electronic state. The considerable types of phase transition are induced by the change of the temperature. Particularly, the multiferroic compounds can be controlled of its physical properties mutually by the external fields such as magnetic, electronic, and elastic ones. The other particular condition, the pressure will directly affect the electron-electron interactions through the change of lattice constants. The beamline 1B in UVSOR is the new one adjusted for the investigations at low temperature and at extremely low-energy region of THz. There is Martin-Puplett type interferometer moved from BL6B and the cryostat covering the temperature between 10 K and 300 K. In this report, I tried to use this newly installed beamline and aimed to get more low energy spectra for samples we use to deal. In the beginning, I prepared some typical compounds having absorption bands in THz region for transmittance experiment.

However, the experiments were resulted in preliminary ones. There were several problems in the alignment process of optical axis. Several upper stream mirrors were lost their original positions after an electrical power down. Also step motion motors for mirror alignment were not fixed even in motion controlled mode. Therefore, every machine time after several month was dedicated for find the light. Fortunately a visible light was also on the same optical axis, we can explore the THz light following it as a loadstar. On the way, I believed to find the THz light but it might not be true one. There were two different type spectra, both the synchrotron light and a black body like light. The later one with rather broad spectrum might be originated in thermally activated mirrors or something near the optical axis (unproved).

Next time, those problems accompanied by the first time experiment will be fixed and the study might be proceeded.

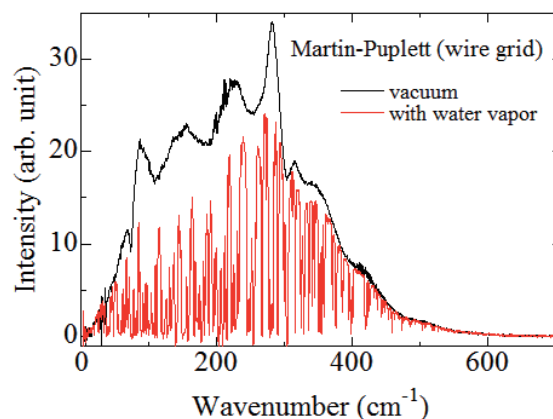


Fig. 1. Difference of light source spectra through blank (vacuum) and water vapor (air). (But the light was said to be 'another' origin.).

BL1B

## Terahertz Spectra of Nano Porous Gold

T. Awano

Department of Electronic Engineering, Tohoku Gakuin University, Tagajo 985-8537, Japan

It is well known that bulk Au is inert. However, Au nanoparticles with several-nanometer-scale sizes are catalytically active for several chemical reactions such as the decomposition of formaldehyde and oxidation of CO. The catalytic activity depends on the size of nanoparticles. The nanoparticles with diameters in the range of 2 to 5 nm show the highest activity for oxidation. Nanoporous Au (NPG) with 10–50 nm pore size also shows catalytic activity for oxidation.

Recently, TiO<sub>2</sub> is being widely used for photocatalysis of various materials. TiO<sub>2</sub> has a different activity with crystal structure for different wavelengths. It has been reported that composite materials of TiO<sub>2</sub> with Au or Pt nanoparticles enhance TiO<sub>2</sub> catalytic activity. TiO<sub>2</sub> plays an active role in the decomposition of water to generate OH radicals. It is supposed that the plasmonic electromagnetic effect of Au or Pt enhances the catalytic activity of TiO<sub>2</sub>. In addition, since pores of NPG are able to trap the TiO<sub>2</sub> particles on its surface, NPG seems to be a photocatalytic nanocomposite because of enhancement of the catalytic activity by the electromagnetic effect. We have found that NPG acts as a promoter to produce OH radicals using TiO<sub>2</sub>. We report optical properties of NPG in this paper to investigate electromagnetic and plasmonic origin of the promoter effect [1].

Figure 1 shows THz-reflectivity spectra of the NPG films on gold-evaporated substrate measured at BL1B. These spectra were connected with other spectral range between millimeter wave and UV. Dielectric constants were obtained by K-K analysis. Plasmon fitting by classical Drude model in energy loss function spectra is shown in Fig. 2. In the Drude model,

$$\epsilon = \epsilon_{\infty} \left( 1 - \frac{\omega_p^2}{\omega^2 + \gamma^2} + i \frac{\gamma \omega_p^2}{\omega(\omega^2 + \gamma^2)} \right)$$

$$\omega_p = \sqrt{\frac{4\pi N e^2}{m^* \epsilon_{\infty}}}$$

where  $\omega_p$  is the plasma frequency,  $\gamma$  is dumping factor and  $\epsilon_{\infty}$  is dielectric constant at high frequency. Energy loss function,  $\text{Im}(1/\epsilon)$ , is proportional to absorption intensity by transverse wave. The plasmon fitting parameters are summarized in Table 1. Systematic decrease of the plasma frequency with pore size increment was observed. Plasma frequency of bulk gold is 8.6eV, therefore, these  $\omega_p$  for pore samples are much small. The promoter effect seems to be related with small values of these parameters. The origin of pore size dependence of the promoter effect is still not clear.

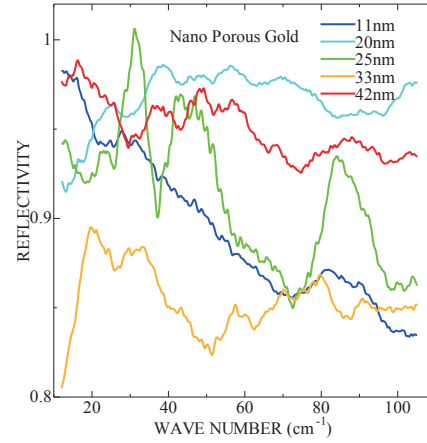


Fig. 1. Reflectivity spectra of nano-porous gold films on Au/SiO<sub>2</sub> glass substrates.

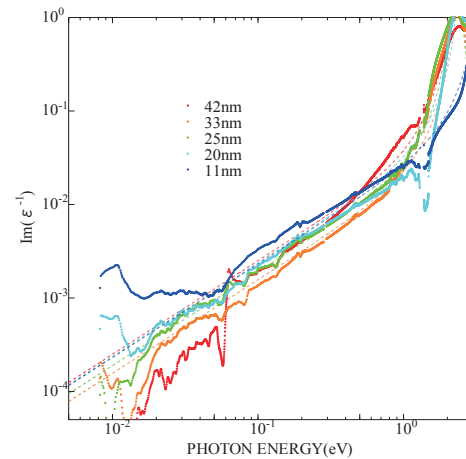


Fig. 2. Drude curve fitting of the energy loss function spectra of NPG membranes on quartz substrates. Dashed lines show fitting curves for each pore size sample.

Table 1. Plasmon parameters.

pore size (nm)	$\omega_p$ (eV)	$\gamma$ (eV)	$\epsilon_{\infty}$
42	2.3	0.06	2.2
33	2.4	0.01	9
25	2.3	0.025	4
20	2.6	0.02	8
11	3.6	0.03	10

[1] S. Kuwano-Nakatani, Y. H. Han, T. Takahashi and T. Awano, *Advanced Electromagnetics* 2 (2013) 5.

BL2A

## Fluorescence Yield XANES Measurement of Thin Film by Silicon-Drift Detector

H. Murata<sup>1</sup>, K. Okada<sup>2,3</sup>, D. Kobayashi<sup>2</sup>, K. Hirose<sup>2</sup> and T. Yamamoto<sup>3</sup>

<sup>1</sup>Advanced Key Technologies Division, National Institute for Materials Science, Tsukuba 305-0044, Japan

<sup>2</sup>Institute of Space and Astronautical Science, Japan Aerospace Exploration Agency, Sagami-hara 252-5210, Japan

<sup>3</sup>Faculty of Science and Engineering, Waseda University, Shinjuku 169-8555, Japan

X-ray absorption near edge structure (XANES) is a powerful tool to reveal local environments of materials with an elemental selectivity. Since it is difficult to prepare the suitable thin samples for transmission mode in soft X-ray region, two alternative techniques, total electron yield (TEY) and fluorescence yield (FY) were usually employed for measurements. FY method gives bulk-sensitive information while TEY does surface-sensitive one. [1] For FY method, there are two suitable sample conditions. One is thin and concentrated, and the other is thick and diluted. Otherwise FY spectra were distorted by the “self-absorption effect”. In addition, counting loss of a detector also affects XANES spectra.

Recently, a silicon-drift detector (SDD), which is high-efficient and energy-dispersive detector, was introduced in UVSOR and now we can measure XANES by both TEY and partial fluorescence yield (PFY) at the same point sequentially. In this study, we reported Si-K XANES of SiO<sub>2</sub> film measured by both of TEY and PFY.

Si-K XANES spectra were measured at BL2A in UVSOR by TEY with drain current and PFY with SDD. The X-ray fluorescence spectra were deconvoluted with gauss functions. Incident X-ray beam was monochromatized with a InSb-(111) ( $2d = 7.481 \text{ \AA}$ ) double crystals monochromator. The samples were SiO<sub>2</sub> glass, Si powder and a SiO<sub>2</sub> film formed on *p*-Si (SiO<sub>2</sub>/*p*-Si). The thickness of the film was 1  $\mu\text{m}$ .

Figure 1(a) shows Si-K XANES of SiO<sub>2</sub>/*p*-Si and references. The component of SiO<sub>2</sub> was observed in both of the TEY and the PFY spectra of SiO<sub>2</sub>/*p*-Si. In the PFY spectrum, it was also found that a contribution derived from *p*-Si around 1840 eV (indicated an arrow). This indicated that PFY spectra reflect on information below 1  $\mu\text{m}$  from the surface for Si-K XANES.

Compared between the TEY and the PFY spectra, the white line in the PFY spectrum of SiO<sub>2</sub>/*p*-Si was underestimated even if the contribution of *p*-Si was removed. This was the mainly caused by the counting loss of SDD since dead time was around 10 % at the white line, as shown in Fig. 1(b).

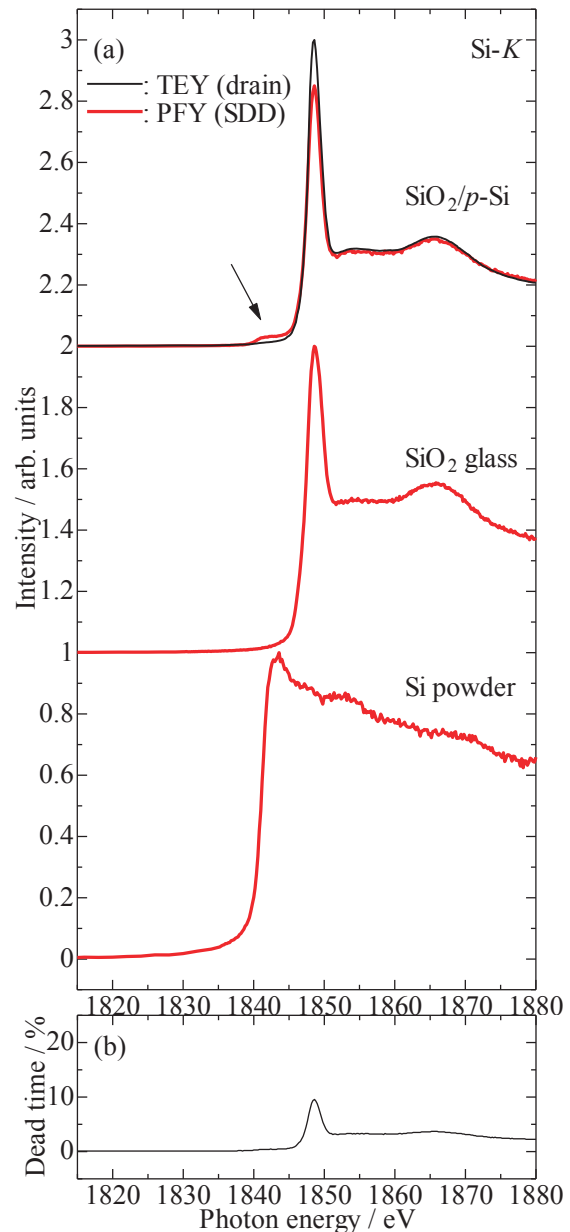


Fig. 1. (a) Si-K XANES of the SiO<sub>2</sub>/*p*-Si and references. (b) Dead time of SDD for SiO<sub>2</sub>/*p*-Si.

[1] T. Yamamoto and K. Kawabata, UVSOR Activity Report **40** (2009) 126.

BL2A

## Soft X-Ray Photoluminescence and Photoluminescence Excitation Spectra of AlGdN around Gd $M_{IV}$ Edge

K. Fujita<sup>1</sup>, K. Fukui<sup>1</sup> and K. Yamamoto<sup>2</sup><sup>1</sup>Department of Electrical and Electronics Engineering, University of Fukui, Fukui 910-8507, Japan<sup>2</sup>Far-Infrared Region Development Research Center, University of Fukui, Fukui 910-8507, Japan

III-V nitride semiconductors doped with the rare earth elements are promising light emitting devices in a wavelength range from visible to ultraviolet.  $Gd^{3+}$  ion is known as the light emitting material having  $\sim 3.9$  eV emission line by  ${}^6P_{7/2}$  (lowest excited state)  $\rightarrow$   ${}^8S_{7/2}$  (ground state)  $4f$  intra- transition. This emission energy (3.9 eV) is higher than the band gap energy of GaN, so we should use AlN or AlGa<sub>2</sub>N as the host semiconductor materials for Gd. In previous work [1], a sharp 3.9 eV line emission was clearly observed from AlGdN, and its photoluminescence (PL) excitation (PLE) spectra in a energy range between 3 and 7 eV showed that the emission process was host excitation. We also showed that PLE spectra of this 3.9 eV line around Al K edge (1.55  $\sim$  1.6 keV) and Gd  $M_{IV}$  edge (1.2  $\sim$  1.25 keV) show very similar to total electron yield (TY) spectrum [2]. They indicate that there is a process which transfers energy from band-to-band transition in the matrix to  $4f$  intra-transition of  $Gd^{3+}$  ion. They also indicate that this 3.9 eV emission does not observed by the intra-atomic  $4f$  to  $4f$  excitation of  $Gd^{3+}$ , but clearly observed by the allowed intra-atomic  $3d$  to  $4f$  excitation. Then, we carried out soft X-ray (SX) PL measurements around both Al K edge and Gd  $M_{IV}$  edge and their PLE measurements with TY measurements to investigate the relaxation process of excited inner core electrons.

AlGdN thin film was grown in a MBE system with a RF-plasma assisted radical cell on the Si-face of (0001)-oriented 6H-SiC substrate. The thickness of the sample is about 120 nm. Concentration of  $Gd^{3+}$  ions is 13% (Al<sub>0.87</sub>Gd<sub>0.13</sub>N). All SX-PL, PLE and TY measurements were carried out at room temperature (RT) with a silicon drift detector (SDD).

Figure 1 shows the PL spectra of AlGdN at RT. The excitation energy is 1215 eV. Peaks less than 1000 eV including the largest peak around 900 eV and above the excitation energy are SX emission lines of Cu sample holder and “sum peaks” by SDD itself, respectively. Emission line due to  $Gd^{3+}$  intra-atomic transition is found around 1200 eV as a small peak. This peak is observed only when the excitation photon energy is near and higher than Gd  $M_{IV}$  edge energy. PLE spectrum of this peak and TY spectrum are plotted in Fig. 2(a) and (b), respectively. It is found that the spectrum feature of PLE spectrum

is very similar to that of TY spectrum which is clearly explained by the  $3d^{10}4f^7 \rightarrow 3d^94f^8$  transition array [3].

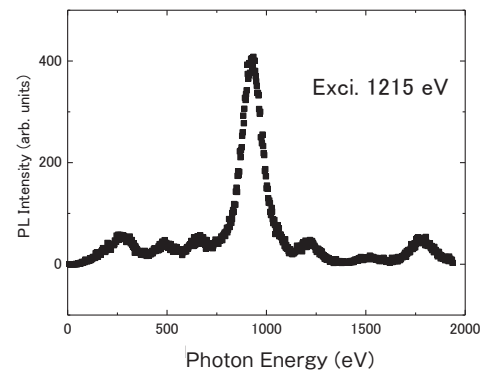


Fig. 1. PL spectrum of Al<sub>0.87</sub>Gd<sub>0.13</sub>N at RT.

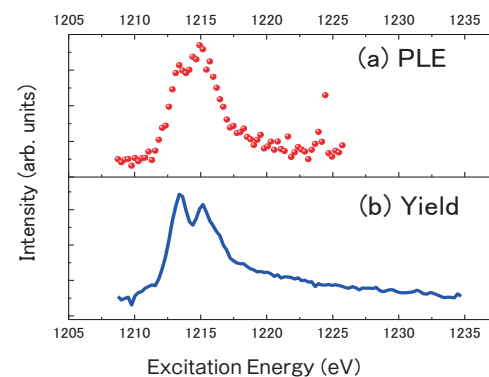


Fig. 2. PLE (a) and TY (b) spectra of Al<sub>0.87</sub>Gd<sub>0.13</sub>N at RT.

- [1] K. Fukui *et al.*, Phys. Stat. Sol. (c) **7** (2010) 1878.  
 [2] K. Fujita *et al.*, UVSOR Activity Report **40** (2012) 95.  
 [3] C. Bonnelle *et al.*, J. Phys. B **10** (1977) 795.

BL2A

## Chemical State Analyses of Ag Species Loaded on Ga<sub>2</sub>O<sub>3</sub> Photocatalysts

T. Yoshida<sup>1</sup>, M. Yamamoto<sup>2</sup>, N. Yamamoto<sup>2</sup> and S. Yagi<sup>1</sup>

<sup>1</sup>*EcoTopia Science Institute, Nagoya University, Furo-cho, Chikusa-ku, Nagoya 464-8603*

<sup>2</sup>*Department of Applied Chemistry, Graduate School of Engineering, Nagoya University, Nagoya 464-8603*

CO<sub>2</sub> reduction is important not only for the energy storage as usable and value-added products but for the abatement of CO<sub>2</sub> as a greenhouse gas. Especially, photocatalytic reduction of CO<sub>2</sub> with water is environment-friendly and attractive as the artificial photosynthesis. It has been reported that Ga<sub>2</sub>O<sub>3</sub> shows photocatalytic activity for CO<sub>2</sub> reduction with water to produce CO as well as for water splitting to H<sub>2</sub> and O<sub>2</sub>, and Ag loading on Ga<sub>2</sub>O<sub>3</sub> (Ag/Ga<sub>2</sub>O<sub>3</sub>) promotes the CO<sub>2</sub> reduction [1].

In the present study, Ag L<sub>3</sub>-edge XAFS measurements were performed to clarify the chemical states and the local structures of Ag species in Ag/Ga<sub>2</sub>O<sub>3</sub> samples.

The reaction tests were carried out with a fixed-bed flow reactor. Photocatalysts (mass: 0.2 g) were put into the reactor cell under flowing CO<sub>2</sub> gas. When we exposed this reactor cell to UV light for 1 h, a NaHCO<sub>3</sub> aqueous solution was added to this reactor cell in dark condition. After an hour, UV light irradiation was started. Analysis of products was performed using a thermal conductivity detector gas chromatography (TCD-GC, Shimadzu GC-8A).

X-ray absorption fine structure (XAFS) measurements were carried out at the beam line 2A station of UVSOR-II at the Institute for Molecular Science and the beam line 6N1 station of Aichi Synchrotron Radiation Center. Ag L<sub>3</sub>-edge XANES spectra of the samples were measured at room temperature in total electron yield mode and the fluorescent X-ray yield mode with a silicon drift detector (Vortex Electronics).

The results of photocatalytic reduction of CO<sub>2</sub> with water are summarized in Table 1. All samples exhibited photocatalytic activity for CO<sub>2</sub> reduction to produce CO, H<sub>2</sub> and O<sub>2</sub>. The amount of CO production over 0.1 wt% Ag/Ga<sub>2</sub>O<sub>3</sub> is larger than that over bare Ga<sub>2</sub>O<sub>3</sub>. It is confirmed that the Ag loading promotes CO<sub>2</sub> reduction.

Figure 1 shows Ag L<sub>3</sub>-edge XANES spectra of silver-loaded gallium oxide samples (Ag/Ga<sub>2</sub>O<sub>3</sub>) together with those of Ag and Ag<sub>2</sub>O reference samples. The spectrum feature in the post-edge region reflects the local structure around the target Ag atom, that is, the coordination symmetry and electronic state of the Ag atom. The XANES spectrum of 1 wt% Ag/Ga<sub>2</sub>O<sub>3</sub> [Fig.1 (b)] exhibits a sharp absorption (whiteline) at 3354 eV due to the oxidized Ag as well as the fine resonance peaks at 3380, 3399 eV characteristic of the metallic Ag. This result suggests that Ag metal particles are partially oxidized in 1 wt% Ag/Ga<sub>2</sub>O<sub>3</sub>. Note that the absorption peaks due to the

Ag metal and oxides are weak in the spectrum of 0.1 wt% Ag/Ga<sub>2</sub>O<sub>3</sub> and indistinct broad feature is observed. It seems that the Ag particles are atomically dispersed by connecting directly to Ga<sub>2</sub>O<sub>3</sub>.

Table 1. The results of photocatalytic reduction of CO<sub>2</sub> with water over Ga<sub>2</sub>O<sub>3</sub> and Ag loaded Ga<sub>2</sub>O<sub>3</sub> catalysts.

photocatalyst	amount of CO ( $\mu\text{mol/h}$ )	amount of H <sub>2</sub> ( $\mu\text{mol/h}$ )
Ga <sub>2</sub> O <sub>3</sub>	0.2	2.5
0.1 wt% Ag/Ga <sub>2</sub> O <sub>3</sub>	2.1	5.2
1 wt%	1.1	0.8

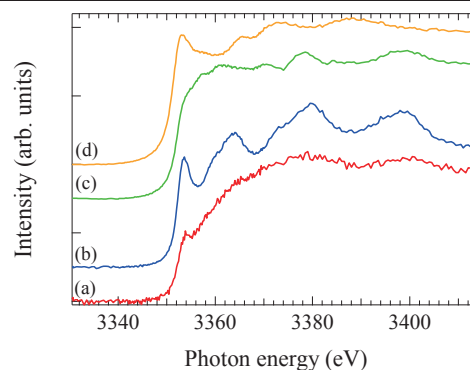


Fig. 1. Ag L<sub>3</sub>-edge XANES spectra of (a) 0.1 wt% Ag/Ga<sub>2</sub>O<sub>3</sub>, (b) 1 wt% Ag/Ga<sub>2</sub>O<sub>3</sub>, (c) Ag foil and (d) Ag<sub>2</sub>O.

[1] K. Koci, K. Mateju, L. Obalova, S. Krejcikova, Z. Lacny, D. Placha and L. Capek, *Appl. Catal., B: Environ.* **96** (2010) 239.

BL2A

## Local Structure Investigation of FAU Zeolite Prepared from Si Based Waste Materials

M. Sato<sup>1</sup>, M. Togo<sup>2</sup>, Y. Inoue<sup>2</sup>, K. Hara<sup>2</sup> and A. Nakahira<sup>1,2</sup>

<sup>1</sup>Kansai Center for Industrial Materials Research, Tohoku University, Osaka 599-8531, Japan

<sup>2</sup>Department of Material Science, Osaka Prefecture University, Osaka 599-8531, Japan

Blast furnace slag (BF slag) is one of the industrial waste materials, and efficient use of the BF slag has been sought for a long time. BF slag is obtained as a by-product in an iron manufacturing process, and generation amount is about 25 million tons per year in Japan. It has been widely used as mixture material and fine aggregate for cement, road bed, source of rock wool, dressing and ground improvement materials because of its hydraulic property. Since the consumption amount of BF slag is smaller than its generation amount, however, additional efficient use of BF slag has been strongly desired.

In a previous study, LTA Na-P1 and FAU type zeolite were successfully synthesized using BF slag and some kinds of waste glass. To synthesize the FAU zeolite in a single phase, optimum aging time about 150 hours was necessary, and the ratio between Na-P1 and FAU zeolite changed strongly depending on the aging time as shown in Fig. 1. Therefore, Si-K and Al-K edge XAFS was measured to investigate the effect of aging time to the local structure around both atoms.

BF slag, waste glass, NaAlO<sub>2</sub> and NaOH were used as starting materials. Si/Al ratio was controlled at around 2. The starting materials and 2 mol/L NaOH solution were encapsulated into a Teflon vessel, and aged for several periods. After aging, they were hydrothermally treated at 368 K for 72 hours. After that, obtained products were also filtered and dried at 323 K for overnight.

Al-K and Si-K edge XANES spectra of obtained samples before and after hydrothermal synthesis were measured by fluorescence mode using InSb double-crystal monochromator for Si-K and KTP double-crystal monochromator for Al-K at BL-2A station of UVSOR.

Figure 2 shows Al-K edge XANES spectra of samples before hydrothermal treatment. Obtained spectra of samples were resembled with starting material and no changes were observed by aging. This result indicates that the local structure around Al atom does not changed during the aging. On the other hand, Al-K edge XANES spectra of the sample after hydrothermal treatment were resembled to that of commercial FAU zeolite. Similar results were obtained in the case of Si-K edge XANES spectra.

From these results, the aging does not affect to the local structure of Al and Si in sample and it is suggested that the frameworks of zeolite is determined at the point of nucleation during

hydrothermal synthesis.

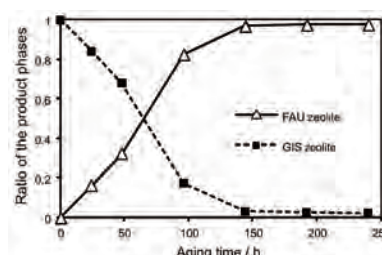


Fig. 1. Relationship between generation phase and aging time.

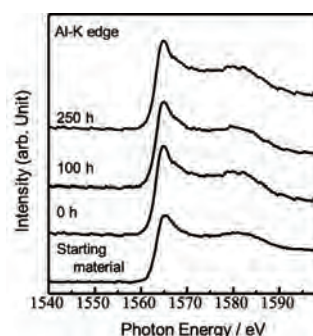


Fig. 2. Al-K edge XANES spectra of samples, which before hydrothermal synthesis, prepared at different aging period.

BL2A

## Partial Fluorescence Yield XANES Measurements for Ultra-Dilute Dopants by Silicon-Drift Detector

H. Murata<sup>1</sup>, T. Taniguchi<sup>1</sup> and T. Yamamoto<sup>2</sup>

<sup>1</sup>Advanced Key Technologies Division, National Institute for Materials Science, Tsukuba 305-0044, Japan

<sup>2</sup>Faculty of Science and Engineering, Waseda University, Shinjuku 169-8555, Japan

Fluorescence yield (FY) method of X-ray absorption near edge structure (XANES) is suitable for ultra-dilute dopants. In hard X-ray region, it is possible to measure 10 ppm dopants [1]. On the other hand, FY has following difficulties in soft X-ray region: low fluorescence yield and overlap of characteristic X-ray. Recent progress of light sources and detectors, such as top-up mode and energy dispersive silicon drift detector (SDD), made us enable to measure XANES of ultra-dilute dopants even in soft X-ray region. In UVSOR, a SDD was introduced for soft X-ray spectroscopy.

Cubic boron nitride (*c*-BN) has a similar crystal structure and features to diamond. It is a good matrix for soft X-ray spectroscopy since it consists of only light elements. It was interesting that a large rare-earth cation, Ce<sup>3+</sup>, is substituted for N-site with surrounding B vacancies [2] and thus it is essential to investigate local environments of dopants in *c*-BN. In this report, we present an attempt of XANES measurements for ultra-dilute dopants in *c*-BN by partial fluorescence yield (PFY) with SDD.

S-K XANES spectra were measured by PFY with SDD at BL2A in UVSOR. The X-ray fluorescence spectra were deconvoluted by gauss functions. We also consider the component of elastic scattering. Incident X-ray beam was monochromatized with a InSb-(111) ( $2d = 7.481 \text{ \AA}$ ) double crystals monochromator. The sulfur-doped *c*-BN (*c*-BN:S) samples were synthesized under high-pressure and high-temperature conditions. Samples were mounted by carbon tape on Al sample holder.

Figure 1 shows typical X-ray fluorescence spectra of *c*-BN:S at different incident energy. Besides characteristic X-ray from the sample, B-K, N-K and S-K, it was also observed additional characteristic X-ray, C-K, O-K, Fe-L and so on. These derived from the optical and measurement system, such as a chamber, a monochromator and carbon tape, for example.

Since the sample contains only trace sulfur, the S-K signals were weak, about 1 cps at the peak. However, long dwell time (20 sec/points, 3 h/spectra) enabled us to obtain good XANES spectra, as shown in Fig. 2. It was noted that total electron yield method with drain current could not detect S-K XANES at all. A detailed analysis of local environments of sulfur in *c*-BN is in progress using first-principles calculations.

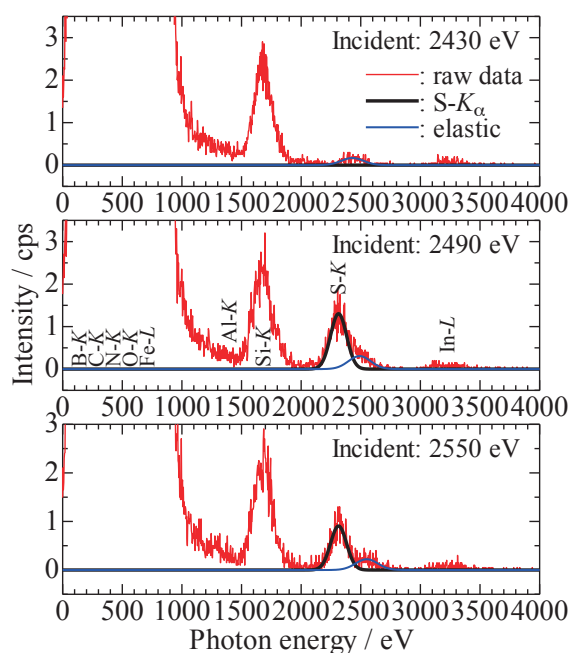


Fig. 1. Typical X-ray fluorescence spectra of *c*-BN:S measured by SDD at different incident energy.

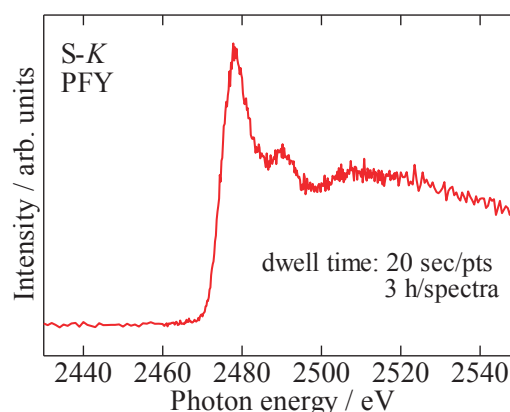


Fig. 2. S-K XANES of *c*-BN:S measured by PFY with SDD

[1] I. Tanaka *et al.*, Nat. Mater. **2** (2003) 541–545.

[2] R. Ishikawa *et al.*, Phys. Rev. Lett. **110** (2013) 065504.

BL2A

## Evaluation of Local Structures of Si for LTA Nano-Zeolite on the Grinding Process

A. Nakahira<sup>1,2</sup>, T. Tagami<sup>1</sup>, H. Kanayama<sup>1</sup>, H. Sakaguchi<sup>1</sup>, K. Hara<sup>1</sup>, Y. Inoue<sup>1</sup>, M. Sato<sup>2</sup>  
and H. Aritani<sup>3</sup>

<sup>1</sup>Faculty of Engineering, Osaka Prefecture University, Gakuencho, Sakai 599-8531, Japan

<sup>2</sup>Osaka Center, IMR, Tohoku University, Gakuencho, Sakai 599-8531, Japan

<sup>3</sup>Saitama Institute of Technology, Fukaya 369-0293, Japan

Zeolites have the unique 3D micropore networks. They are one of aluminosilicate minerals commonly used as various commercial adsorbents and other applications. For example, zeolites are in fact widely used in petroleum industry as a catalyst for the preparation of advanced materials. Furthermore, they are used to extract nitrogen purification from air to increase oxygen content for both industrial and medical purposes. Recently, in addition, they are applicable to water purification, and also Cs purification in nuclear accidents. However, in order to expand the applications of zeolite in various industrial fields, furthermore modification of microstructures and morphology is needed for zeolites. [1-3] For example, a lot of attentions are focused on the synthesis of the finely nanosized zeolite powders by various novel processing. Although many novel processing are attempted to synthesize the nano-sized zeolite powders, the finely nano-sized zeolite powders were synthesized by the mechanical mixing processing in this study. And the local structures were investigated for finely nano-sized zeolite powders prepared by the mechanical mixing processing.

Commercial LTA type zeolite was prepared. Nano-sized zeolite was synthesized by the following method. The powder of this LTA type zeolites powder was milled for 30 min and 120min by the mechanical milling method with the high energy forces. After the milled and ground nano-sized LTA type zeolite powder were characterized by XRD method, FT-IR and TG-DTA. The microstructures of nano-sized LTA type zeolite powder were observed by SEM. The local structures around Si for the products of nano-sized LTA type zeolite powder were characterized by measuring X-ray adsorption near edge structure (XANES) at BL02A in UV-SOR.

The evaluation of XRD for ground fine-zeolite and reference LTA was carried out. XRD results showed that after the mechanical mixing processing for 30 min and 120min the ground products were also identified to be LTA type. The results indicated that the obtained fine-zeolite products were LTA type zeolites. Products obtained after the mechanical mixing processing had the average particle of a few hundred nanometer in diameter, suggesting the nano-sized LTA zeolite powders were successfully

obtained by after the mechanical mixing processing for 2 hs

Figure 1 shows the XANES spectra of zeolites and reference materials. As shown in Fig. 1, XANES spectra of sample obtained after the mechanical mixing processing for 30 min to 120 min the same spectra as the LTA without mechanical mixing. These results suggest nano-sized LTA zeolite powders possess the good crystallinity and also the same local structure of Si after the mechanical mixing processing.

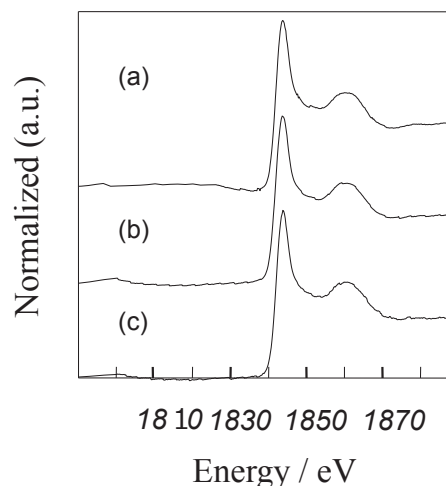


Fig. 1. Si XANES spectra of zeolites and reference materials. (a)commercial LTA, (b)30min, and (c)120min.

[1] C. D. Chang, A. J. Silvestri, *Journal of Catalysis* **47** (1977) 249–259.

[2] T. Wakihara, R. Ichikawa, J. Tatami, A. Endo, K. Yoshida, Y. Sasaki, K. Komeya and T. Meguro, *Cryst. Growth Des.* **11** (1977) 955–958.

[3] A. Nakahira, S. Nishimura, H. Aritani, T. Yamamoto S. Ueda, *J. Mater. Sci.* **36** (2001) 1885–89.

BL2A

## Ag-L and P-K Edge XAFS Measurement of Antibacterial HAp

M. Sato<sup>1</sup>, H. Sakaguchi<sup>2</sup>, Y. Inoue<sup>2</sup> and A. Nakahira<sup>1,2</sup>

<sup>1</sup>Kansai Center for Industrial Materials Research, Tohoku University, Osaka 599-8531, Japan

<sup>2</sup>Department of Material Science, Osaka Prefecture University, Osaka 599-8531, Japan

Hydroxyapatite ( $\text{Ca}_{10}(\text{PO}_4)_6(\text{OH})_2$ , HAp) is a chief component of our hard tissue and it shows excellent biocompatibility and osteoconductivity. Therefore, it has been widely used as an alternate of hard tissue in an orthopedic surgical procedure. However, bacterial infection has been a major problem in orthopedic surgery. Therefore, the development of a new implant which can prevent a bacterial infection during surgery is strongly desired.

There are many studies to provide an antibacterial effect for implant by the doping of some kinds of metal elements. In these elements, silver, copper and zinc are understood to show and excellent antibacterial effect with very small amount of use.

In this study, Ag doped HAp were prepared by conventional hydrothermal process, and local structure around P and Ag atom was investigated by XAFS measurement.

0.1 mol/L  $\text{Ca}(\text{NO}_3)_2$ ,  $(\text{NH}_4)_2\text{HPO}_4$  and  $\text{AgNO}_3$ , solutions were used as starting materials. These solutions were mixed up each other becoming the ratio of Ca to P of 1.67 and the ratio of Ag changed from 0.5 to 10 mol% for Ca of HAp in a Teflon vessel, and pH of mixed solution was adjusted to 10. After mixing, they were hydrothermally treated at 423 K for 24 hours. Obtained solutions were filtered and dried at 323 K for overnight.

Ag-L and P-K edge XANES spectra of obtained Ag-HAp powders were measured in a total electron yield mode and fluorescence mode by SDD detector using InSb double-crystal monochromator at BL-2A station in UVSOR. For XAFS measurement, commercial HAp,  $\text{AgNO}_3$  and  $\text{Ag}_3(\text{PO}_4)$  were used as references.

From the XRD analysis, HAp generated for all samples as a main phase. In addition, metal Ag was generated for the sample prepared at the ratio of Ag more than 2 mol% for Ca of HAp. ICP measurement showed that the actual amount of Ag in obtained sample is about one tenth of additive amount.

Figure. 1 shows P-K edge XANES spectra of samples prepared in Ag ratio of 0.5 and 1 mol%. Since obtained P-K edge XANES spectra of sample was resembled that of commercial HAp, it is clarified that the local structure around P atom does not change by doping of Ag. From this result, the possibility of Ag substitution into HAp structure was suggested.

On the other hand, since we did not obtain the clear spectra for Ag-L edge of sample in this measurement, we will study continuously to obtain the clear Ag-L edge XAFS spectrum.

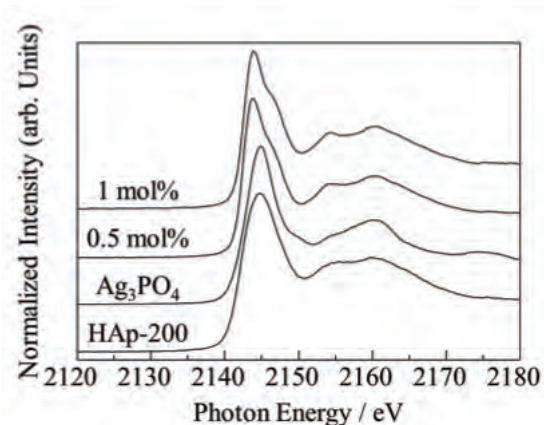


Fig. 1. P-K edge XANES spectra of obtained samples.

[1] M. Sato, S. Yamamoto, Y. Nishio, Y. Takamatsu and A. Nakahira, UVSOR Activity Report **38** (2011)115.

[2] M. Sato, Y. Kawabe, S. Misu, S. Hayashi and A. Nakahira, UVSOR Activity Report **39** (2012)81.

[3] M. Sato, T. Nagayasu, S. Hayashi and A. Nakahira, UVSOR Activity Report **40** (2013)126.

BL2A

## Investigation of Local Structure of Ca-Based Materials Synthesized from Granulated Blast Furnace Slag

M. Sato<sup>1</sup>, M. Togo<sup>2</sup>, T. Morinaga<sup>2</sup>, S. Fujihara<sup>2</sup> and A. Nakahira<sup>1,2</sup>

<sup>1</sup>Kansai Center for Industrial Materials Research, Tohoku University, Osaka 599-8531, Japan

<sup>2</sup>Department of Material Science, Osaka Prefecture University, Osaka 599-8531, Japan

Blast furnace slag (BF slag) is one of the industrial waste materials and generates about 25 million tons per year in Japan. BF slag mainly consisted from SiO<sub>2</sub>, CaO and Al<sub>2</sub>O<sub>3</sub>. Fe, Ti and Mn are included as trace elements. By focusing on this composition of BF slag, it can be recognized that the ratio of Si, Ca and Al is close to a tobermorite, and the ratio of Si and Al is also close to a zeolite.

In a previous study, tobermorite, Ca-based layered double hydroxide (LDH) and calcium phosphate were successfully synthesized using BF slag. In these materials, tobermorite is one of the most important calcium silicate materials and has been widely used architectural materials such as autoclaved lightweight concrete (ALC) and fire-resistant building materials. Tobermorite has layer structure of that SiO<sub>4</sub> tetrahedra sandwiches CaO sheet and cation exchange ability by substituting a part of Si by Al ion.

It has been clarified that the Al substituted tobermorite has selectivity for cation such as alkali metal and alkali-earth metal ions.

Since tobermorite also has a high selectivity for Cs ion, it has been suggested that can use for handling of nuclear waste. Therefore, XAFS measurement was conducted to investigate a local structure around Si and Al atom of obtained tobermorite.

BF slag, quartz powder and CaO powder were used as starting materials. BF slag was ball-milled to become particle size less than 75 μm. Ca/(Si+Al) ratio was controlled in the range from 0.8 to 1.2 by addition of quartz or CaO powder. Mixed powder and distilled water was encapsulated into a Teflon vessel, and then it was hydrothermally treated at 453 K for 24 and 48 h with rotation speed of 20 rpm. After that, obtained products were filtered and dried at 323 K for overnight.

Al-K and Si-K edge XANES spectra of obtained samples were measured by fluorescence mode by SDD using InSb double-crystal monochromator for Si-K and KTP double-crystal monochromator for Al-K at BL-2A station of UVSOR.

From the Si-K edge XANES spectra, the spectrum of sample prepared at Ca/(Si+Al) = 1.0 was resembled with that of commercial tobermorite, and significant change of spectrum by rotation during a hydrothermal synthesis did not observed.

Figure 1 shows Al-K edge XANES spectra of sample prepared by hydrothermal synthesis using BF slag. Obtained spectra showed similar trend to Si-K edge XANES spectra, and local structure around Al

atom changed depending on the ratio between Ca and Si+Al. These results suggested that the Al-substituted tobermorite was synthesized by using BF slag, and the possibility to use tobermorite as not only architectural materials, but also environmental purification materials was indicated.

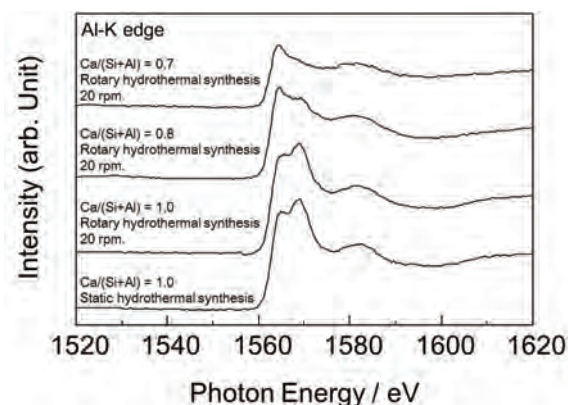


Fig. 1. Al-K edge XANES spectra of samples prepared by static and rotary hydrothermal synthesis at 453 K for 48 h.

BL2A

## Structural Evaluation of Novel Piezoelectric Ceramics

A. Nakahira<sup>1,2</sup>, H. Kanayama<sup>1</sup>, T. Tagami<sup>1</sup>, S. Togo<sup>1</sup>, S. Fujihara<sup>1</sup>, T. Morinaga<sup>1</sup>,  
M. Sato<sup>2</sup> and H. Aritani<sup>3</sup>

<sup>1</sup>Faculty of Engineering, Osaka Prefecture University, Gakuencho, Sakai 599-8531, Japan

<sup>2</sup>Kansai Center, IMR, Tohoku University, Gakuencho, Sakai 599-8531, Japan

<sup>3</sup>Saitama Institute of Technology, Fukaya 369-0293, Japan

Piezoelectric ceramics are widely used as piezoelectric, electro-optic and non-linear optic devices in modern society. Among piezoelectric ceramics, PZT ( $\text{Pb}(\text{Zr}_x\text{Ti}_{1-x})\text{O}_3$ ) is used extensively in the world, but it contains lead damaging human health and environment. In order to solve this problem of PZT, the development of lead-free piezoelectric ceramics are desired. Much attention is attracted to niobium based complex oxide,  $\text{KNbO}_3$  with the perovskite-type structure as one of the promising ceramics instead of PZT ceramics [1-3].  $\text{KNbO}_3$  ceramics have the higher curie temperature (435 °C) and energy conversion rate (0.69) of  $\text{KNbO}_3$  than that of another post PZT materials.

$\text{KNbO}_3$  was synthesized by the electrode reaction process in KOH solution as electrolyte using metal niobium plate ( $10 \times 20 \times 0.2$  mm) as an anode and carbon (C) rod ( $\phi 5 \times 100$  mm) as cathode. The distance between Nb and C electrodes was about 40 mm in the beaker. The reaction was continued until Nb plate was completely dissolved under 100 mA /  $\text{cm}^2$  of current density supplied direct current power. Then, the precipitation obtained during the reaction was filtered and collected by centrifugation. The solid product was frequently washed and air-dried at 50 °C. For the comparison,  $\text{KNbO}_3$  (KN-ref) as a reference material was prepared by the solid reaction process at 1150 to 1250 °C. Products were characterized with some techniques such as XRD, FT-IR, TG/DTA and the microstructures were observed with SEM. The local structures around K for the products of the solid product powder were characterized by measuring X-ray adsorption near edge structure (XANES) at BL02A station of UVSOR in Okazaki.

As a result of XRD diffraction patterns and SEM images, finely nano-sized  $\text{KNbO}_3$  powder was synthesized in 1 M KOH solution. SEM observations indicated that obtained  $\text{KNbO}_3$  powder with several hundred nanometer in diameter were synthesized. On the contrary,  $\text{KNbO}_3$  (KN-ref) as a reference material prepared by the solid reaction process had the particle size with 5 to 10 micrometer in diameter, i.e.

micro-sized  $\text{KNbO}_3$  (KN-ref) powders. These results suggest that the fine nano-sized  $\text{KNbO}_3$  powders were successfully obtained from the electrode reaction process.

Figure 1 shows the XANES spectra of synthesized by the electrode reaction process products (nano KN) and a reference material ( $\text{KNbO}_3$  : KN-ref). XANES spectra of sample obtained the same spectra as the reference micron-sized  $\text{KNbO}_3$  (KN-ref). These results suggest the fine nano-sized  $\text{KNbO}_3$  powders synthesized by the electrode reaction process possess the good crystallinity and also the same local structure of K-edge as the reference  $\text{KNbO}_3$  (KN-ref).

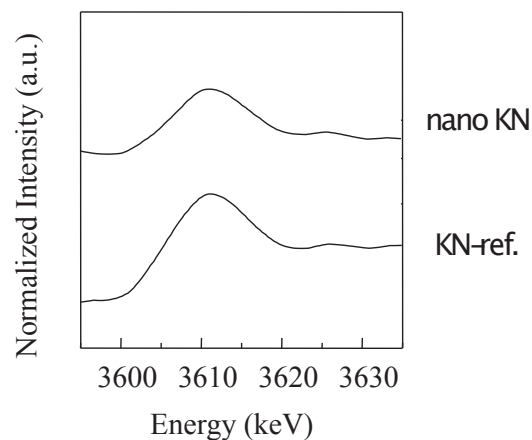


Fig. 1. K-edge XANES spectra of nano-sized  $\text{KNbO}_3$  and a reference material (micro-sized  $\text{KNbO}_3$  (KN-ref)).

[1] T. R. ShROUT *et al.*, Journal of Electroceramics **19** (2007) 111-124.

[2] I. Nowak *et al.*, Chemical Reviews **99** (1999) 3603-3624.

[3] C. H. Lu *et al.*, Materials Letter **34** (1998) 172-176.

BL3B

## Intrinsic Luminescence and Energy Transfer from Self-Trapped Excitons in Scandium Borates upon Vacuum UV Excitation

N. Kodama, A. Abe, Y. Morisawa, T. Sakashita and T. Takahashi  
Faculty of Engineering and Resource Science, Akita University, Akita 010-8502, Japan

The intrinsic luminescence characteristics were investigated for self-trapped excitons (STEs) in polycrystalline samples of the binary scandium borates  $\text{LaSc}_3(\text{BO}_3)_4$  (LSB),  $\text{YSc}(\text{BO}_3)_2$  (YSB), and  $\text{LuSc}(\text{BO}_3)_2$  (LuSB), in which absorption of vacuum ultraviolet (VUV) light by the host can facilitate efficient energy transfer from the STEs to  $\text{Re}^{3+}$  ( $\text{Re}^{3+} = \text{Sm}^{3+}$ ,  $\text{Gd}^{3+}$ , or  $\text{Tb}^{3+}$ ) ions.

Emission and excitation spectra were measured at temperatures in the range 7.8–293 K using the Ultraviolet Synchrotron Orbital Radiation (UVSOR) facility. All of the borates were found to exhibit intense intrinsic emissions in the UV region under VUV excitation at 70 and 160 nm, and the decay times were determined. These emissions were assigned to recombination of STEs possibly associated with bandgap excitations, or to molecular transitions in the  $\text{BO}_3^{3-}$  group. The emission spectra for undoped LSB under VUV excitation at temperatures of 7.8–293 K were characterized by three distinct broad bands at 253 nm (I), 323 nm (II), and 379 nm (III), as shown in Fig. 1(a). These features are similar to those found in the emission spectra for single-crystal LSB. The emission spectra for undoped YSB and LuSB at 293 K are shown in Fig. 1(b). For undoped YSB, two broad emission bands were present in the temperature range 15–293 K, the first centered at 258 nm (I) and the second at 320 nm (II). Undoped LuSB exhibited a single strong broad emission at 250 nm in the temperature range 14.9–293 K.

For undoped LSB, the decay times for emissions I, II, and III were less than 10 ns, 115 ns and 3.4  $\mu\text{s}$ , respectively. For undoped YSB, the decay time for emissions I and II were 120 and 550 ns, respectively. By analogy with the STE states in alkali halides [1], the fast decay components II in LSB and I in YSB originate from singlet STE states with center and/or off-center configurations. The fast component I in LSB may have the same origin, and may also have a contribution from energy transfer to impurities or defects near the STE. In contrast, the slow components III in LSB and II in YSB are thought to originate from a triplet STE with an off-center configuration. Energy transfer from the STEs to  $\text{Re}^{3+}$  ions at temperatures between 7.8 or 14.9 and 293 K was evidenced by a decrease in STE emissions and shortened decay times in LSB doped with  $\text{Sm}^{3+}$ ,  $\text{Gd}^{3+}$  or  $\text{Tb}^{3+}$ , and YSB doped with  $\text{Gd}^{3+}$ . The STE emission intensity decreased with increasing  $\text{Re}^{3+}$  concentration (1–40 at.%), accompanied by the

appearance of intense emissions associated with  $\text{Re}^{3+}$  at 7.8 K for  $\text{Sm}^{3+}$ -doped LSB (Fig. 2(a)), and at 14.9 K for  $\text{Tb}^{3+}$ -doped LSB (Fig. 2(b)). This suggests efficient energy transfer from the STEs to the  $\text{Re}^{3+}$  ions.  $\text{Re}^{3+}$  doping also caused a decrease in the decay times for the STE emissions, which is consistent with the decrease in the time-averaged STE emission intensity. This provides further evidence for energy transfer from the STEs to the  $\text{Re}^{3+}$  ions. In the case of LSB at a temperature of 293 K, the energy transfer rates determined from time-resolved measurements were  $1.6 \times 10^6 \text{ s}^{-1}$  (STE II) and  $7.0 \times 10^4 \text{ s}^{-1}$  (STE III) for 5 at.%  $\text{Gd}^{3+}$  doping, and  $2.1 \times 10^6 \text{ s}^{-1}$  (STE II) and  $8.0 \times 10^4 \text{ s}^{-1}$  (STE III) for 5 at.%  $\text{Tb}^{3+}$  doping.

The observed energy transfer rates are within an order of magnitude of estimates based on dipole-dipole or dipole-quadrupole energy transfer. For both LSB and YSB, the ratio of the STE II and III emission intensity in doped samples to that in undoped samples gradually increased with temperature. This temperature dependence is shown in Fig. 3 for  $\text{Sm}^{3+}$ - and  $\text{Tb}^{3+}$ -doped LSB, and suggests that energy transfer from STEs to  $\text{Re}^{3+}$  ions is thermally activated and probably related to exciton mobility.

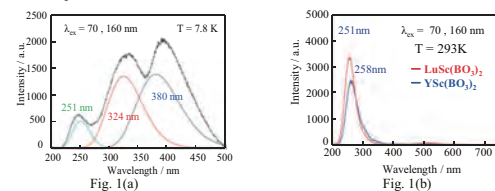


Fig. 1. Emission spectra for undoped samples at excitation wavelengths of 70 and 160 nm: (a) LSB at 7.8 K, and (b) YSB and LuSB at 293 K.

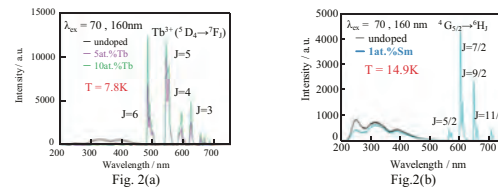


Fig. 2. Emission spectra for samples at 15 K and excitation wavelengths of 70 and 160 nm: (a) undoped and  $\text{Sm}^{3+}$ -doped LSB, and (b) undoped and  $\text{Tb}^{3+}$ -doped LSB.

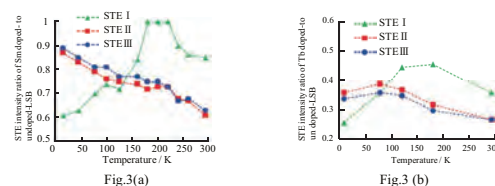


Fig. 3. Temperature dependence of ratio of STE intensity for doped LSB to that for undoped LSB: (a)  $\text{Sm}^{3+}$  doping, and (b)  $\text{Tb}^{3+}$  doping.

[1] K. Kan'no *et al.*, *Pure & Appl. Chem.* **69** (1997) 1227.

BL3B

## Analysis of Optical Properties for Pr<sup>3+</sup>-Doped Y<sub>3</sub>Sc<sub>2</sub>Al<sub>3</sub>O<sub>12</sub>

S. Watanabe<sup>1</sup>, K. Ogasawara<sup>1</sup>, S. Ishii<sup>2</sup> and M. Kitaura<sup>2</sup>

<sup>1</sup>*School of Science and Technology, Kwansei Gakuin University, Sanda 669-1337, Japan*

<sup>2</sup>*Department of Physics, Faculty of Science, Yamagata University, Yamagata 990-8560, Japan*

The  $4f-4f$  and  $4f-5d$  transitions of lanthanide (Ln<sup>3+</sup>) ions have drawn attention for potential application as luminescent materials. The garnet-type oxides are chemically and structurally stable among inorganic compounds. Therefore, to date, Ln<sup>3+</sup>-doped garnet-type oxides have been widely used as commercial materials. The analysis of the optical properties due to the  $4f-4f$  and  $4f-5d$  transitions, however, remains limited, since they originate in the complicated multiplet structures. In addition, the many-body effects and relativistic effects coexist in these issues. In this study, the optical properties of Pr<sup>3+</sup>-doped Y<sub>3</sub>Sc<sub>2</sub>Al<sub>3</sub>O<sub>12</sub> have been investigated, experimentally and theoretically.

Pr<sup>3+</sup>-doped Y<sub>3</sub>Sc<sub>2</sub>Al<sub>3</sub>O<sub>12</sub> polycrystalline sample was prepared by the solid-state reaction. The concentration of Pr<sup>3+</sup> ion was 1 mol%. The experimental excitation spectrum at 10 K was measured monitoring the emission at 333 nm. We analyzed the  $4f^2-4f^15d^1$  transitions of Pr<sup>3+</sup> ions in Y<sub>3</sub>Sc<sub>2</sub>Al<sub>3</sub>O<sub>12</sub> based on first-principles many-electron configuration interaction calculations [1, 2].

Figure 1 shows the experimental excitation spectrum and theoretical absorption spectrum for Pr<sup>3+</sup>-doped Y<sub>3</sub>Sc<sub>2</sub>Al<sub>3</sub>O<sub>12</sub>. The fundamental absorption of Y<sub>3</sub>Sc<sub>2</sub>Al<sub>3</sub>O<sub>12</sub> host crystal is located above 6.7 eV. This result agrees with the excitation spectrum of non-doped Y<sub>3</sub>Sc<sub>2</sub>Al<sub>3</sub>O<sub>12</sub> host crystal. Compared to the theoretical  $4f^2-4f^15d^1$  absorption spectrum of Pr<sup>3+</sup>, the peaks at 4.2 – 6.0 eV can be attributed to the  $4f^2-4f^15d^1$  transitions of Pr<sup>3+</sup> ions. The configuration analysis of many-electron calculations clearly indicates that the separations among main peaks are due to crystal field splitting of the Pr- $5d$  levels, while splitting between the main peaks and subpeaks is due to spin-orbit interaction of the Pr- $4f$  levels. The subpeaks are due to transitions to two-electron excitation states based on a shake-up process.

Figure 2 shows the emission spectra for Pr<sup>3+</sup>-doped Y<sub>3</sub>Sc<sub>2</sub>Al<sub>3</sub>O<sub>12</sub> measured at 10 K under excitation at various photon energies. The sharp peaks at 480 – 800 nm originate in the  $4f^2$  intraconfiguration transitions of Pr<sup>3+</sup> ions, which can be attributed to the  $^3P_0 \rightarrow ^3H_J$  transitions. The broad bands at 300 – 400 nm are considered to be either the excitonic emission of Y<sub>3</sub>Sc<sub>2</sub>Al<sub>3</sub>O<sub>12</sub> host crystal or the  $5d-4f$  emission of Pr<sup>3+</sup> ions. Unfortunately, we have little information on these bands. Further spectroscopy experiments in the UV-VUV region are needed to assign the origins of these two bands.

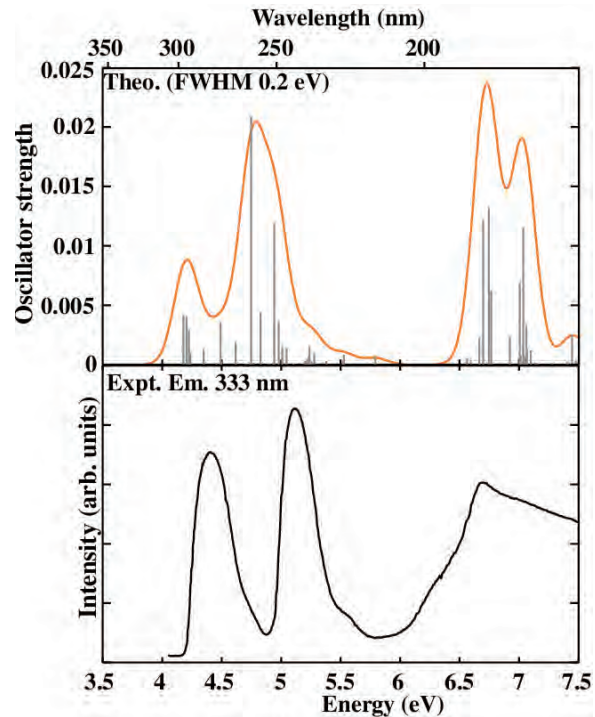


Fig. 1. Experimental excitation spectrum and theoretical absorption spectrum for Pr<sup>3+</sup>-doped Y<sub>3</sub>Sc<sub>2</sub>Al<sub>3</sub>O<sub>12</sub>.

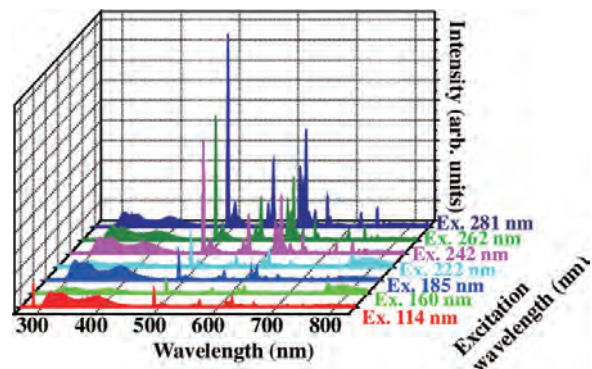


Fig. 2. Emission spectra for Pr<sup>3+</sup>-doped Y<sub>3</sub>Sc<sub>2</sub>Al<sub>3</sub>O<sub>12</sub>.

[1] K. Ogasawara *et al.*, Phys. Rev. B **64** (2001) 143.

[2] S. Watanabe *et al.*, Phys. Rev. B **81** (2010) 125128.

BL3B

## Optical Spectra and Electronic Structure of SrCeO<sub>3</sub> Crystals

H. Numata<sup>1</sup>, M. Kitaura<sup>1</sup>, S. Watanabe<sup>2</sup>, K. Ogasawa<sup>2</sup>, S. Kurosawa<sup>3,4</sup>, K. Yubuta<sup>3</sup>,  
A. Ohnishi<sup>1</sup> and M. Sasaki<sup>1</sup>

<sup>1</sup>Department of Physics, Faculty of Science, Yamagata University, Yamagata 990-8560, Japan

<sup>2</sup>Department of Chemistry, School of Science and Technology, Kwansai University, Sanda 669-1337, Japan

<sup>3</sup>Institute for Materials Research, Tohoku University, Sendai 980-8679, Japan

<sup>4</sup>New Industry Creation Hatchery Center, Tohoku University, Sendai 980-8679, Japan

CeO<sub>2</sub> is characterized by so-called mixed valency, which is caused by mixing between  $4f^0$  and  $4f^1L^{-1}$  configurations in the ground state, where  $L^{-1}$  denotes the hole in the valence band mainly composed of O-2p orbitals [1]. This feature comes from hybridization between the Ce-4f and O-2p orbitals. Indications of the mixed valency have been found in photoemission and X-ray absorption spectra [2]. On the other hand, it has been pointed out that the reflectivity spectrum also exhibits an evidence for the mixed valency: A prominent reflectivity peak around 13 eV has been assigned to an appearance of  $4f^2L^{-2}$  configuration.

SrCeO<sub>3</sub> is also regarded as a mixed valent compound [3], because of similarities in photoemission and X-ray absorption spectra. In addition, this material is known as one of typical proton conductors. Despite the important material in both of basic science and industrial application, the fundamental optical constant spectra such as absorption and reflectivity spectra, and its electronic structure have been few reported so far. One of the reasons for this is the difficulty for the crystal growth of SrCeO<sub>3</sub>. Recently, we have succeeded the crystal growth of SrCeO<sub>3</sub> by using a Floating zone technique.

In the present study, we have measured reflectivity and absorption edge spectra of SrCeO<sub>3</sub> crystals at 300 K. The results are shown in Fig. 1(a). As indicated by a red solid curve, the fundamental absorption starts at 2.2 eV. This energy is lower than that determined from the diffuse reflection spectrum [4]. The reflectivity spectrum (red solid curve) consists of three parts: 3.4-6.3 eV (part I), 6.3-16.5 eV (part II), and 16.5-40 eV (part III). Referred to the calculated energy band structure, the part I, II, and III are assigned to O-2p→Ce-4f, O-2p→Ce-5d, Ce-5p→Ce-5d transitions, respectively. The agreement between experimental and theoretical spectra is good, as shown in Figs. 1(a) and 1(b). Several peaks in the part II are due to the crystal field splitting of the Ce-5d orbital. In the part III, a peak appears around 27.9 eV. Considering the  $5p^55d^1$  configuration of a Ce<sup>3+</sup> ion, it is expected that the transition between <sup>1</sup>P<sub>1</sub> and <sup>1</sup>S<sub>0</sub> multiplets occurs in the part III. Thus, we assign the 27.9 eV peak to the <sup>1</sup>S<sub>0</sub>→<sup>1</sup>P<sub>1</sub> transition. Drastic increase in reflectivity can be seen below 3.4 eV. This would be influenced by the reflection at the back of the crystal, because it occurs in the energy

region below the fundamental absorption edge. Since the absorption coefficient is negligibly weak below 3.4 eV, the monochromatic synchrotron radiation light can penetrate inside the crystal.

As mentioned above, it is expected that the experimental reflectivity spectrum exhibits a peak due to the excitation of the  $4f^2L^{-2}$  configuration. Actually, Fig. 1(a) shows such a peak around 12 eV. On the other hand, Fig. 1(b) also exhibits a prominent peak around 11.9 eV. Since the 11.9 eV peak is connected to the critical point of the joint density of state, it is not likely to attribute the 11.9 eV peak in Fig. 1(a) to the excitation of the  $4f^2L^{-2}$  configuration.

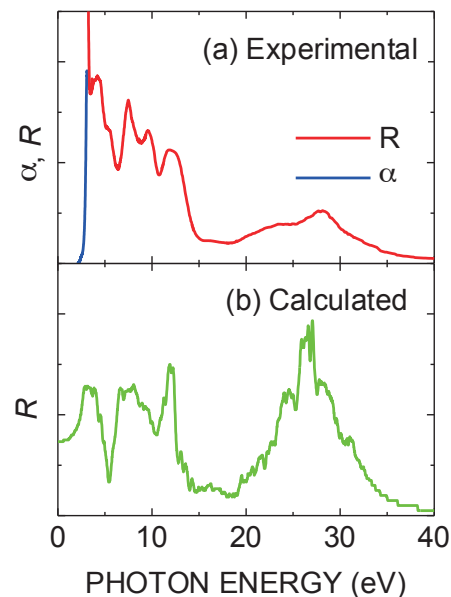


Fig. 1. (a) Reflectivity (red line) and absorption edge (blue line) spectra of SrCeO<sub>3</sub> crystals, measured at 300 K. (b) Theoretical reflectivity spectrum (green line).

[1] A. Fujimori *et al.*, Phys. Rev. B **28** (1983) 2281.

[2] M. Niwano *et al.*, J. Phy. Soc. Jpn. **57**(1988) 1489.

[3] M. Matsumoto *et al.*, J. Electron Spectrosc. Relat. Phenom. **78** (1996) 179.

[4] F. Goubin *et al.*, Chem. Mater. **16** (2004) 662.

BL3B

## Energy Transfer from $\Gamma^-$ Centers to $\text{Au}^-$ Centers in Co-doped $\text{NaCl}:\Gamma^-$ , $\text{Au}^-$ Crystals

T. Kawai and K. Yuasa

Graduate School of Science, Osaka Prefecture University, Sakai 599-8531,

Alkali halide crystals have the wide band-gap up to the vacuum ultra violet energy region and are a suitable candidate host for doping of impurity ions. Though many experimental investigations have been performed on alkali halide crystals doped with impurity ions, energy transfer between two kind of impurity ions in co-doped alkali halide crystals are comparatively less studied [1, 2]. In this study, we have investigated the energy transfer from  $\Gamma^-$  centers to  $\text{Au}^-$  centers in NaCl crystals co-doped with  $\Gamma^-$  and  $\text{Au}^-$  ions.

Figure 1 shows the absorption spectrum of  $\text{NaCl}:\text{Au}^-$  and the luminescence spectrum of  $\text{NaCl}:\Gamma^-$  at room temperature (RT). In  $\text{NaCl}:\text{Au}^-$ , the A, C,  $\text{D}_1$ , and  $\text{D}_2$  absorption bands due to the  $\text{Au}^-$  centers are observed at 4.18, 5.54, 6.25, and 7.10 eV, respectively [3]. In  $\text{NaCl}:\Gamma^-$ , the luminescence band due to the one-center type localized exciton appears at 5.32 eV [4]. The 5.32 eV luminescence band in  $\text{NaCl}:\Gamma^-$  has an overlap with the C absorption band at 5.54 eV in  $\text{NaCl}:\text{Au}^-$ . The fact indicates the potential of the energy transfer from the  $\Gamma^-$  center to the  $\text{Au}^-$  center in co-doped  $\text{NaCl}:\Gamma^-$ ,  $\text{Au}^-$  crystals.

Figure 2 shows the excitation spectra in  $\text{NaCl}:\text{Au}^-$ ,  $\text{NaCl}:\Gamma^-$ , and co-doped  $\text{NaCl}:\Gamma^-$ ,  $\text{Au}^-$  crystals at RT. The 5.32 eV luminescence band in  $\text{NaCl}:\Gamma^-$  is efficiently excited in the energy region between 6.5 and 7.2 eV, where the absorption band due to one-center type localized exciton is located. In  $\text{NaCl}:\text{Au}^-$ , the luminescence band at 3.99 eV, which corresponds to the A' luminescence band due to the  $\text{Au}^-$  centers, is efficiently excited at the A, C,  $\text{D}_1$ , and  $\text{D}_2$  absorption bands. In the co-doped  $\text{NaCl}:\Gamma^-$ ,  $\text{Au}^-$  crystal, the excitation spectrum for the A' luminescence band at 3.99 eV has the broad band around 6.66 eV in addition to the A, C,  $\text{D}_1$ , and  $\text{D}_2$  bands. Since the 6.66 eV band corresponds to the excitation band for the 5.32 eV luminescence band in  $\text{NaCl}:\Gamma^-$ , the fact implies the existence of the energy transfer from the  $\Gamma^-$  center to the  $\text{Au}^-$  center in the co-doped  $\text{NaCl}:\Gamma^-$ ,  $\text{Au}^-$  crystal.

From the absorption intensity of respective absorption bands, the concentrations of the  $\Gamma^-$  and  $\text{Au}^-$  centers in the co-doped  $\text{NaCl}:\Gamma^-$ ,  $\text{Au}^-$  crystal are estimated to be about  $3.0 \times 10^{19}$  and  $1.0 \times 10^{15} \text{ cm}^{-3}$ , respectively. Thus, the average distance between the  $\Gamma^-$  center and its nearest neighboring  $\text{Au}^-$  center is about 2.0 nm. The distance of 2.0 nm indicates the potential of the energy transfer mechanism of Förster type. In order to clarify the energy transfer

mechanism from the  $\Gamma^-$  center to the  $\text{Au}^-$  center in the co-doped  $\text{NaCl}:\Gamma^-$ ,  $\text{Au}^-$  crystals, the measurements of the decay kinetics of the luminescence are needed.

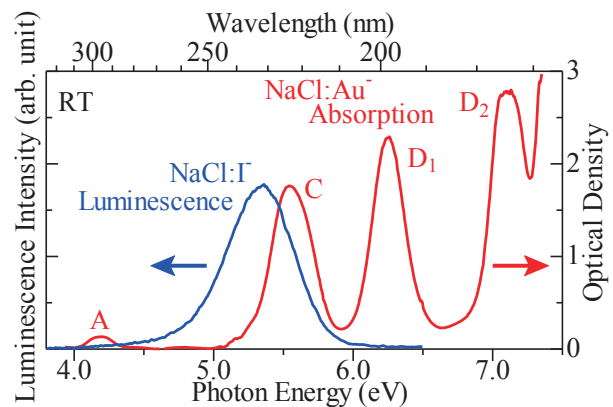


Fig. 1. Luminescence spectrum (blue) of  $\text{NaCl}:\Gamma^-$  and absorption spectrum (red) of  $\text{NaCl}:\text{Au}^-$  at RT.

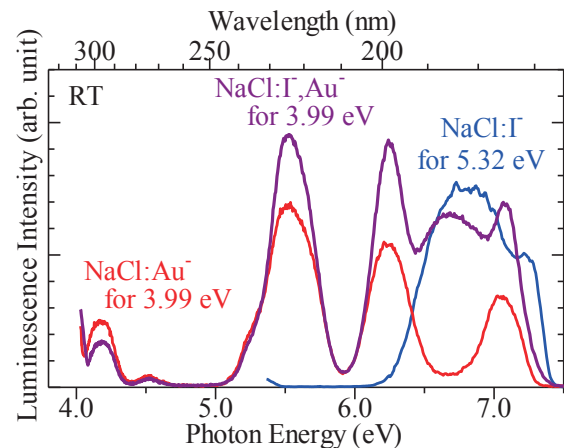


Fig. 2. Excitation spectra of  $\text{NaCl}:\text{Au}^-$  (red),  $\text{NaCl}:\Gamma^-$  (blue), and co-doped  $\text{NaCl}:\Gamma^-$ ,  $\text{Au}^-$  (purple).

[1] A. F. Muñoz and J. O. Rubio, Phys. Rev. B **38** (1988) 9980.

[2] A. Méndez, *et al.*, J. Lumin. **79** (1998) 269.

[3] F. Fischer, Z. Physik **231** (1970) 293.

[4] I. Akimoto, *et al.*, Phys. Status Solidi C **6** (2009) 342.

BL3B

## Photoluminescence Study on Structural Deformation of LaAlO<sub>3</sub> Induced by Ion Implantation

M. Harima, Y. Horii, T. Morimoto and Y. Ohki

Waseda University, 3-4-1 Ohkubo, Shinjuku-ku, Tokyo 169-8555, Japan

High permittivity (high- $k$ ) materials such as LaAlO<sub>3</sub> or YAlO<sub>3</sub> are expected as a gate insulator in advanced MOS devices. In the manufacturing process of semiconductors, ion implantation through a gate dielectric to a Si substrate is often used to adjust the threshold voltage of a metal oxide semiconductor (MOS) device [1]. However, ion implantation may induce localized electronic states in the forbidden band and defects resulting from degradation of crystallinity.

In the present study, the effects of implantation of P<sup>+</sup> or B<sup>+</sup> ions on the structural change of single crystal LaAlO<sub>3</sub> were examined. Before and after ion implantation, optical absorption, photoluminescence (PL) and X-Ray diffraction (XRD) were measured.

In Fig. 1, an optical absorption edge is seen at about 5.6 eV. This edge, which corresponds to the band gap energy of LaAlO<sub>3</sub>, is scarcely affected by the ion implantation.

Figure 2 shows PL spectra. As shown in Fig. 2(a), a broad PL peak due to the oxygen vacancy appears at around 2.8 eV [2]. The intensity of this PL, which is also detectable in amorphous samples [3], scarcely changes after the ion implantation. In addition, three sharp PL peaks were detected at 1.62, 1.65, and 1.69 eV as shown in Fig. 2(b). The intensities of the three PLs become smaller by ion implantation. These PLs are due to Cr<sup>3+</sup> that are present in LaAlO<sub>3</sub> as impurities [4]. It is known that this type of PL appears only when the samples are crystalline [5]. These results indicate that the ion implantation degrades the crystallinity of LaAlO<sub>3</sub>.

Figure 3 shows in-plane XRD spectra. The XRD peak intensity at  $2\theta = 23.5^\circ$  is decreased by the ion implantation. One important thing is that the depth measurable by XRD is too shallow to evaluate the crystallinity of the area where ions had passed through. In this regard, PL measurements can cover the whole ion-implanted area.

To conclude, it has become clear that deformation of crystal structure of LaAlO<sub>3</sub> is induced by ion implantation.

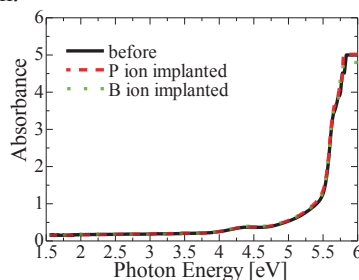
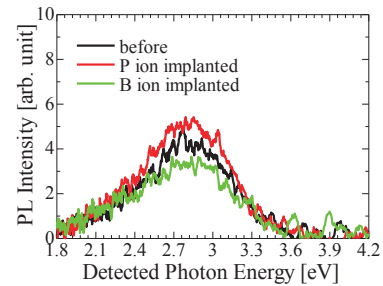
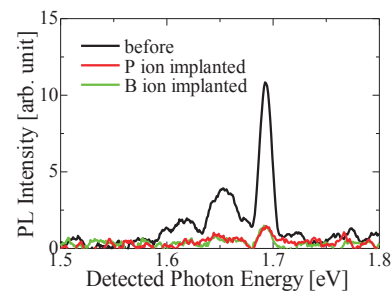


Fig. 1. Optical absorption spectra observed before and after the implantation of P<sup>+</sup> or B<sup>+</sup> ions at a fluence of  $10^{15}$  cm<sup>-2</sup>. Note that the three spectra overlap each other.



(a)



(b)

Fig. 2. PL spectra induced by the irradiation of 5.0-eV (a) and 6.4-eV (b) photons observed before and after the implantation of P<sup>+</sup> or B<sup>+</sup> ions at a fluence of  $10^{15}$  cm<sup>-2</sup>.

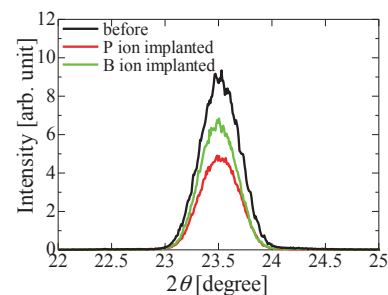


Fig. 3. In-plane XRD patterns observed before and after the implantation of P<sup>+</sup> or B<sup>+</sup> ions at a fluence of  $10^{15}$  cm<sup>-2</sup>.

[1] B. Razavi and T. Kuroda, *Design of Analog CMOS Integrated Circuits* (Tokyo; Maruzen, 2003).

[2] E. Hirata *et al.*, *Jpn. J. Appl. Phys.* **49** (2010) 091102.

[3] H. Nishikawa *et al.*, *Phys. Rev. Lett.* **72** (1994) 2101.

[4] D. Yamasaka *et al.*, *Jpn. J. Appl. Phys.* **52** (2013) 071501.

[5] J. Heber *et al.*, *Z. Phys.* **246** (1971) 261.

BL3B

## Observation of VUV Emission from Er/Nd:LuF<sub>3</sub> Crystals

S. Kurosawa<sup>1,2</sup>, J. Pejchal<sup>2</sup>, M. Kitaura<sup>3</sup>, K. Fukui<sup>4</sup>, K. Nakagawa<sup>5</sup>, S. Watanabe<sup>6</sup>,  
A. Ohnishi<sup>3</sup>, K. Ogasawara<sup>6</sup>, M. Hasumoto<sup>7</sup> and M. Sakai<sup>7</sup>

<sup>1</sup>Institute for Materials Research, Tohoku University, Sendai 980-8679, Japan

<sup>2</sup>New Industry Creation Hatchery Center, Tohoku University, Sendai 980-8679, Japan

<sup>3</sup>Department of Physics, Faculty of Science, Yamagata University, Yamagata 990-8560, Japan

<sup>4</sup>Department of Electrical and Electronics Engineering, University of Fukui, Fukui 910-8507, Japan

<sup>5</sup>Graduate School of Human Development and Environment, Kobe University, Kobe 657-8501, Japan

<sup>6</sup>School of Science and Technology, Kuwansei University, Sanda 669-1337, Japan

<sup>7</sup>UVSOR facility, Institute for Molecular Science, Okazaki 444-8585, Japan

The development of new fast radiation detection systems employing the vacuum ultraviolet (VUV) scintillators has been started in the recent past. In these systems, the fast VUV scintillators can be coupled with advanced VUV photodetectors, such as position-sensitive gas electron multipliers (GEM), micro-pixel chambers or VUV-sensitive photomultipliers with CsI-coated photocathodes [1,2]. One of the candidates considered for the VUV scintillator is the Nd-doped BaLu<sub>1.2</sub>Y<sub>0.8</sub>F<sub>8</sub> (BaYLuF). The fast VUV emission around 185 nm with a decay time of several nanoseconds is due to the allowed 5d-4f transition of the Nd<sup>3+</sup> ion. Even more favorable properties, such as significantly elevated scintillation efficiency and emission shifted to even shorter wavelengths were found for LuF<sub>3</sub> single crystals [3]. Shorter emission wavelength usually matches better the sensitivity of the mentioned VUV photodetectors.

Recently, we tried to improve the energy transfer from the host matrix to the Nd<sup>3+</sup> luminescence center by Tm-codoping. As the Tm<sup>3+</sup> 5d-4f emission spectrum coincides with the Nd 4f-5d absorption band, the energy would migrate over the Tm<sup>3+</sup> 5d levels to the Nd<sup>3+</sup> ones. This was successfully proved [4], even though the improvement of the overall scintillation efficiency was not significant.

Since Er<sup>3+</sup> has also emission lines in the VUV region, other co-dopant effect with Er is investigated in this study; LuF<sub>3</sub> codoped with 1-mol% Er / Nd 1-mol% and 1 mol% Er doped LuF<sub>3</sub> samples were grown by micro-pulling down method. In order to show the energy transfer, we measured the emission spectra using BL3B beam line at UVSOR.

Figure 1 shows the emission spectra of the LuF<sub>3</sub>Er1% sample excited at 135nm at 9K and LuF<sub>3</sub>Er1%Nd1% excited at 145nm at 9K. The result for Er-doped sample shows presence of both low-spin and high-spin transitions at 160 and 165nm, respectively. For the ErNd codoped sample no Er<sup>3+</sup> emission is observed at all, even though the sample is excited in the Er<sup>3+</sup> absorption band. This proves the energy transfer from the Er<sup>3+</sup> to Nd<sup>3+</sup> ions.

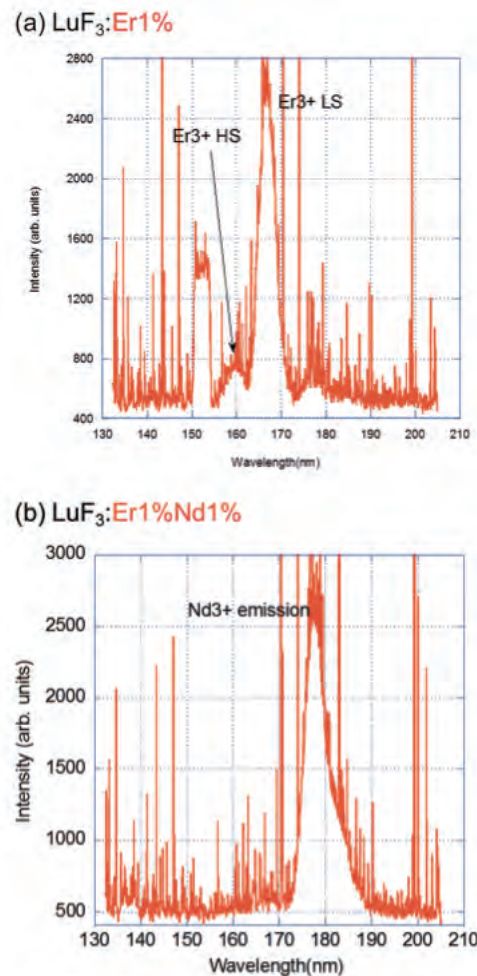


Fig. 1. Emission spectra of the LuF<sub>3</sub>Er1% sample excited at 135nm at 9K (a) and LuF<sub>3</sub>Er1%Nd1% excited at 145nm at 9K (b).

- [1] R. Chechik, A. Breskin, Nucl. Instr. and Meth. A **595** (2008) 116-131 and references therein.  
 [2] S. Kurosawa, J. Pejchal *et al.*, J. Instrumentation **7** (2012) C03013.  
 [3] T. Yanagida, N. Kawaguchi, K. Fukuda *et al.*, Nucl. Instr. Meth. A **659** (2011) 258-261.  
 [4] J. Pejchal, K. Fukuda, M. Nikl *et al.*, IEEE Trans. Nucl. Sci. **59** (2012) 2177-2182.

BL3B

## Optical Spectroscopy of Rare-Earth Doped $Y_3Al_5O_{12}$ (RE=Ce, Eu, Tb, Pr) Single Crystals

M. Yamaga, K. Takagi, T. Kishita, D. Susuki and H. Watanabe

Department of Mathematical and Design Engineering, Gifu University, Gifu 501-1193, Japan

Current white LEDs with high efficiency and brightness are composed of an InGaN-based blue LED and a yellow phosphor in the powder form of  $Ce^{3+}$ -doped  $Y_3Al_5O_{12}$  (Ce:YAG). As the emission from Ce:YAG lacks the red component of the spectrum, the white light has a low color-rendering value. In order to obtain warm white light and an appropriate color rendering value, it is required to add the red emission by codoping  $Ce^{3+}$  and other rare-earth ions, such as  $Pr^{3+}$ ,  $Eu^{3+}$  and  $Tb^{3+}$ . Such enhancement of the red component may be achieved through energy transfer between  $Ce^{3+}$  and codoped ions.

Rare-earth doped YAG single crystals were prepared using the Czochralski method by NIMS. Optical measurements at 300 K were done at BL3B.

Figure 1 shows the optical absorption spectra of Ce:Pr:YAG, Ce:Eu:YAG, Ce:Eu:Tb:YAG, and Ce:YAG. The absorption spectrum of  $Ce^{3+}$  in YAG consists of four bands with peaks at 205, 228, 340 and 458 nm, being due to the  $4f \rightarrow 5d$  transitions of  $Ce^{3+}$ . In Ce:Pr:YAG, the intense broad bands at 237 and 290 nm other than the  $Ce^{3+}$  bands are due to the  $4f \rightarrow 5d$  transitions of  $Pr^{3+}$ . The fairly weak lines around 600 nm is assigned to the  $^3H_4 \rightarrow ^1D_2$  transition of  $Pr^{3+}$ . The intense broad band below 240 nm in Ce:Eu:YAG is due to the charge transfer transitions to  $Eu^{3+}$  or the  $4f \rightarrow 5d$  transitions of  $Eu^{3+}$ , whereas the fairly weak line at 400 nm is due to the  $^7F_0 \rightarrow ^5D_3$  transition of  $Eu^{3+}$ . In Ce:Eu:Tb:YAG, a new intense broad band with a peak at 270 nm other than the broad bands in Ce:Eu:YAG is due to the  $4f \rightarrow 5d$  transitions of  $Tb^{3+}$ .

Figure 2 shows the emission spectra observed in (a) Ce:YAG, (b) Ce:Pr:YAG, (c) Ce:Eu:YAG, and (d) Ce:Eu:Tb:YAG. Excitation at 340 and 458 nm in the  $Ce^{3+}$  absorption bands for (a) Ce:YAG produced the broad emission bands with double peaks due to the  $5d \rightarrow 4f$  ( $^2F_{5/2}$ ,  $^2F_{7/2}$ ) transitions of  $Ce^{3+}$ . In (b) Ce:Pr:YAG, excitation at 610 nm, corresponding to the  $^3H_4 \rightarrow ^1D_2$  transition of  $Pr^{3+}$ , produced the several sharp emission lines in the range from 610 to 830 nm, being assigned to the  $^1D_2 \rightarrow ^3H_J$  ( $J=4,5,6$ ) transitions. The emission spectrum excited at 291 nm consists of two broad bands at 320 and 380 nm, several sharp weak lines in the wide range from 490 to 830 nm, and the weak  $Ce^{3+}$  emission band. On the other hand, excitation at 458 nm produced the weak  $Pr^{3+}$  emission lines at 610, 640 and 830 nm other than the intense  $Ce^{3+}$  emission band. In (c) Ce:Eu:YAG, the emission spectrum excited at 220 nm consists of the weak sharp lines at 592, 609, 630, and 709 nm due to the  $^5D_0 \rightarrow ^7F_J$  ( $J=1,2,3,4$ ) transitions of  $Eu^{3+}$ . In (d)

Ce:Eu:Tb:YAG, excitation at 271 nm produced the intense sharp lines at 385 nm and (490, 550, 590 and 625) nm and the weak  $Ce^{3+}$  emission band. These sharp lines are assigned to the  $^5D_3 \rightarrow ^7F_6$  and  $^5D_4 \rightarrow ^7F_J$  ( $J=6,5,4,3$ ) transitions in this series. The emission spectrum excited at 220 nm consists of the sharp lines from both  $Eu^{3+}$  and  $Tb^{3+}$  and the  $Ce^{3+}$  emission band.

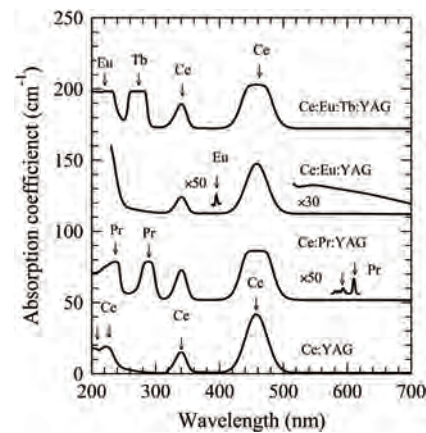


Fig. 1. Absorption spectra for rare-earth doped YAG crystals.

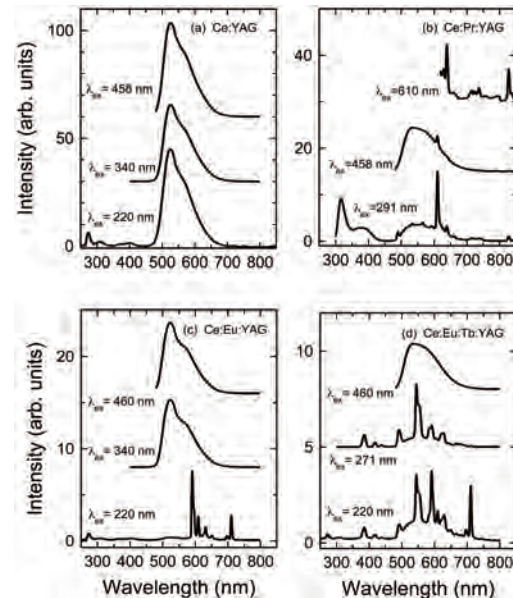


Fig. 2. Emission spectra for rare-earth doped YAG crystals.

BL3B

## Optical Properties of Amorphous Carbon Nitride Thin Films

D. Itoh<sup>1</sup>, K. Fukui<sup>1</sup> and K. Yamamoto<sup>2</sup>

<sup>1</sup>Department of Electrical and Electronics Engineering, University of Fukui, Fukui 910-8507, Japan

<sup>2</sup>Far-Infrared Region Development Research Center, University of Fukui, Fukui 910-8507, Japan

Amorphous Carbon Nitride ( $a\text{-CN}_x$ ) is known to have interesting mechanical, electrical and optical properties. In the case of optical properties, it is expected that  $a\text{-CN}_x$  becomes cheap white LED material, because photoluminescence (PL) of  $a\text{-CN}_x$  spreads over the visible (VIS) region. However, PL spectrum of  $a\text{-CN}_x$  has sample preparation condition dependences. Recently, it is found that laser irradiated  $a\text{-CN}_x$  thin film after depositing shows much higher PL intensity than that of as-deposited  $a\text{-CN}_x$  thin film [1]. Then, we have been measuring laser irradiated  $a\text{-CN}_x$  to investigate its luminescence mechanism and growth condition dependences by using combined excitation emission (CEE) spectroscopy.

All samples are deposited on Si substrates by the RF-sputtering method at Ryukoku University. Their thickness is about 1  $\mu\text{m}$ . Laser-irradiation time to as-deposited samples is 240 minutes by using He-Cd laser (325 nm) with 20 mW. All CEE spectra have been measured at BL3B [2].

Figures 1 and 2 show CEE spectra at 20 K of as deposited ( $a\text{-CN}_x(\text{A})$ ) and laser irradiated  $a\text{-CN}_x$  thin films ( $a\text{-CN}_x(\text{L})$ ), respectively. Higher intensity regions are represented by warm colors. PL spectra widely spread in VIS region, though their width becomes narrower after laser irradiation. Photon energies of PL peak and PL excitation of both  $a\text{-CN}_x(\text{A})$  and  $a\text{-CN}_x(\text{L})$  are  $\sim 3.3$  eV and 4.5, 5.5 eV, respectively. However, maximum intensity of  $a\text{-CN}_x(\text{L})$  is 90 times larger than that of  $a\text{-CN}_x(\text{A})$ .

Figure 3 shows emission spectra of  $a\text{-CN}_x(\text{A})$  and  $a\text{-CN}_x(\text{L})$  at the excitation energies of 4.6 eV and 5.5 eV. Asymmetric line shape of each spectrum can be decomposed by two Gaussian type emission bands. Higher energy side band has its peak at 3.5 eV in all spectra. However, lower energy side peak shifts from 2.9 eV to 3.1 eV after laser irradiation. These higher and lower energies are correspond to the energy gaps between  $\pi^*$  and  $\pi$ ,  $\sigma^*$  and  $N_{\text{LP}}$  (nitrogen lone pair) bands, respectively, following from Nitta's band diagram [3]. According to C 1s XPS results, contribution of  $sp^2$  bonding decreases and that of  $sp^3$  one increases after laser irradiation. Since these XPS results are probably explain as the decrease of the overlap between  $\sigma^*$  and  $\pi^*$  bands, and increase energy gap of  $N_{\text{LP}}\text{-}\sigma^*$  [4] after laser irradiation. Then, it is supposed that the degree of hybridization of  $\sigma^*$  and  $\pi^*$  bands is important to understanding the effect of the laser irradiation.

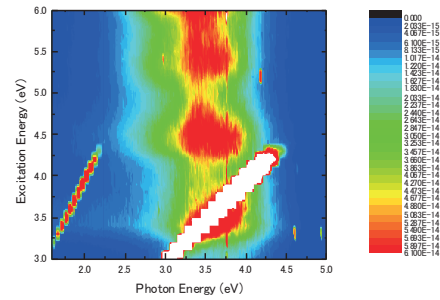


Fig. 1. CEE Spectrum of as-deposited  $a\text{-CN}_x$ .

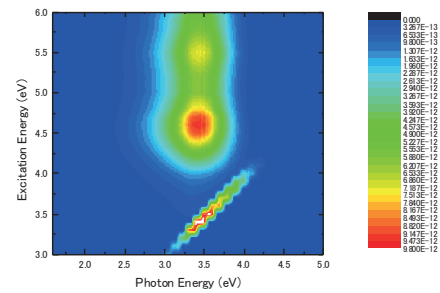


Fig. 2. CEE Spectrum of laser irradiated  $a\text{-CN}_x$ .

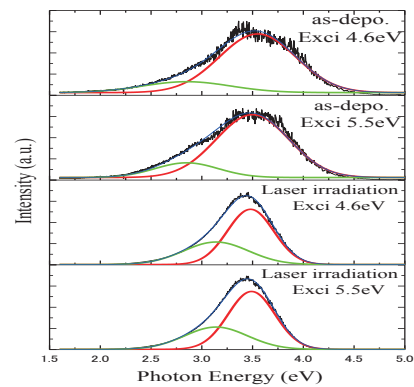


Fig. 3. Emission Spectra of as-deposited and laser irradiated  $a\text{-CN}_x$  at the excitation energies of 4.6 and 5.5 eV.

- [1] M. Satake *et al.*, 2013 JSAP Autumn Meeting 28p-PB3-11.
- [2] K. Fukui *et al.*, J synchrotron Rad. **21** (2014) 452.
- [3] S. Nitta, Oyo Buturi **69** (2000) 7 (in Japanese).
- [4] Y. Zhang *et al.*, Sci. Rep. **3** (2013) 1943.

BL4U

## The Effect of PFI on the Microstructural Aggregates of PEDOT:PSS by Scanning Transmission X-Ray Microscopy

M. W. Lin<sup>1</sup>, H. W. Shiu<sup>1</sup>, Y. L. Lai<sup>1</sup>, T. F. Guo<sup>2</sup> and Y. J. Hsu<sup>1</sup>

<sup>1</sup>National Synchrotron Radiation Research Center, Hsinchu, Taiwan 300, Republic of China

<sup>2</sup>Department of Photonics, National Cheng Kung University, Tainan, Taiwan 701, Republic of China

A spin-casted conducting polymer PEDOT:PSS (poly(3,4-ethylenedioxythiophene): poly(styrenesulfonate)) forms a hole-injection layer with a gradient work function tuned by self-organization of the PFI, which resulted in a remarkably improved device efficiency of organic light-emitting diodes and organic photovoltaics. From previous X-ray photoelectron spectroscopy (XPS) measurements, we found the sulfide component is increased, while the PSS concentration decreases after the addition of PFI. However, the PFI is rich at the surface and its concentration gradually decreases with depth. We therefore investigated whether if the morphology change of PFI aggregation on surface is caused by the interplay between PEDOT:PSS and PFI. To study the chemical morphology with several blended polymers, the Scanning Transmission X-ray microscopy (STXM) measurements were utilized to explore the heterogeneous structure and chemical properties of PEDOT:PSS:PFI composited polymers at S *L*-edge.

Near-edge X-ray absorption fine structure (NEXAFS) taken at S *L*-edge (Figs. 2(a) and (b)) in beamline BL4U identifies major characteristic peaks for PEDOT:PSS and PFI unambiguously (Chemical structures are shown in Fig. 1). The spectra of PEDOT:PSS display strong intensity in the energy range between 170 to 175 eV which are associated with the sulfonic acids groups, energy range between 165 to 170 eV corresponding to sulfur atoms in PEDOT (Fig. 2(a)). In Fig. 2(b), the PFI has a strong absorption between 170 to 175 eV, which are associated with the sulfonic acids in PFI. The 3D optical density (OD) images were acquired to discriminate the composition and structure change caused by PFI. Figure 3 (a) and (b) exhibit OD images of PEDOT:PSS and PEDOT:PSS:PFI, extracted from 3D images, respectively. Despite several large spots caused by dusts, the obtained imaging at 166.8 eV (which is characteristic peak of PEDOT) for PEDOT:PSS:PFI film (Fig. 3 (b)) has denser dark particles in compared to pure PEDOT:PSS film (Fig. 3 (a)). As a result, the addition of PFI tends to aggregate on surface. The obtained data indicates that the blending of PFI on PEDOT:PSS generates high concentration of PFI-covered surface and cause the re-distribution of sulfonic acids group in PEDOT:PSS. The OD images for PEDOT:PSS and PEDOT:PSS:PFI are hence different. Also, the results from STXM greatly

resembles with our XPS findings, the adding PFI re-arrange the distribution of PEDOT:PSS. It should be noted that the obtained OD image was not divided by the pre-edge image (for example at 160 eV) due to the beamlight around 160 eV to 180 eV exists periodic distribution of dark and bright. Again, the periodic distribution minimizes the absorption contrast attributed by the sample. Nonetheless, from the STXM results, we still found the PFI changes the distribution of PEDOT:PSS. The result is important to explain how the PFI influence the interplay of PEDOT:PSS compositions.

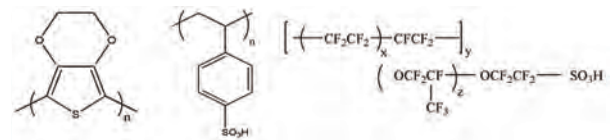


Fig. 1. The chemical structures of conducting polymers used in this study.

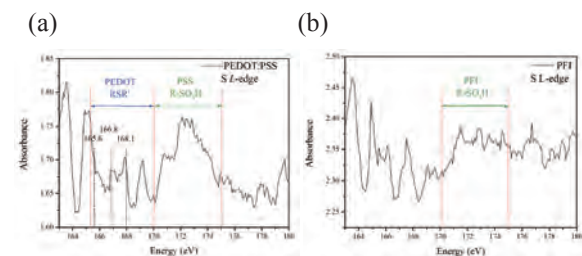


Fig. 2. S *L*-edge NEXAFS of the (a) PEDOT:PSS and (b) PFI.

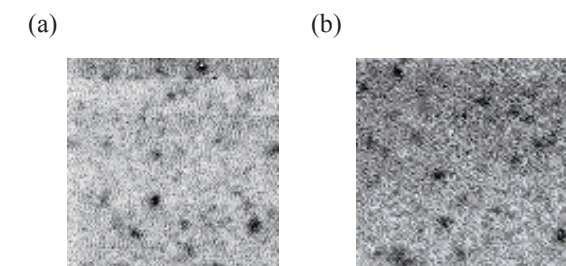


Fig. 3. The OD image for S *L*-edges extracted from 3D images of (a) PEDOT:PSS and (b) PEDOT:PSS:PFI.

[1] T. W. Lee, Y. Chung, O. Kwon, and J. P. Park, *Adv. Funct. Mater.* **17** (2007) 390.

BL4U

## Observation of the Origin of $d^0$ Magnetism in ZnO Nanostructures Using X-Ray-Based Microscopic and Spectroscopic Techniques

S. B. Singh<sup>1</sup>, Y. F. Wang<sup>1</sup>, J. W. Chiou<sup>2</sup>, W. F. Pong<sup>1</sup>, T. Ohgashi<sup>3</sup> and N. Kosugi<sup>3</sup>

<sup>1</sup>Department of Physics, Tamkang University, Tamsui 251, Taiwan

<sup>2</sup>Department of Applied Physics, National University of Kaohsiung, Kaohsiung 811, Taiwan

<sup>3</sup>Editorial Board, UVSOR Facility, Institute for Molecular Science, Okazaki 444-8585, Japan

In present report, efforts have been made to elucidate the origin of  $d^0$  magnetism<sup>1,2</sup> in ZnO nanocactus (NC) and nanowires (NW) using X-ray-based microscopic and spectroscopic techniques. The magnetic hysteresis curve obtained in an applied field revealed that the saturation magnetization in ZnO NC exceeded that of the NW. Figure 1 shows the O  $K$ -edge scanning transmission X-ray microscopy (STXM) and corresponding x-ray absorption near-edge structure (XANES) spectra of the ZnO nanostructures. The experiments were performed at the 4U beamline. The O  $K$ -edge STXM stack mappings were recorded at two randomly selected regions in ZnO NC (NC-1 and NC-2) and NW (NW-1 and NW-2) respectively (see Figs. 1a-d). The insets in the figures also present corresponding scanning electron microscopy images that help to identify the regions and can be used to verify the STXM images. To overcome the signal-to-noise ratio of the XANES spectra obtained from specific mapping areas in the STXM images, the O  $K$ -edge STXM-XANES spectra in Fig. 1(e) were obtained as the sum of the XANES spectra in the regions that are bordered by yellow dashed lines, as shown in NC-1, NC-2, NW-1 and NW-2. According to the dipole-transition selection rule, the features at  $\sim 535$ - $550$  eV are attributed to the electron excitations from O  $1s$ -derived states to  $2p_{xy}$ -derived (along the bilayer) and O  $2p_z$ -derived (along the  $c$  axis) states, which are approximately proportional to the density of the unoccupied O  $2p$ -derived states.<sup>3</sup> The intensities of the O  $K$ -edge STXM-XANES spectra of NC-1 and NC-2 are clearly higher than those of NW-1 and NW-2. The STXM-XANES results consistently demonstrate that the population of defects at the O sites in ZnO NC is larger than in the NW and confirming the enhanced density of states of O  $2p$ -derived states, as the population of defects and dangling bonds at/above  $E_{\text{CBM}}$  or  $E_{\text{F}}$  in ZnO NC exceeds that in the NW. The experimental results are also consistent with the measurements of extended X-ray absorption fine structure spectroscopy, X-ray excited optical luminescence spectroscopy and X-ray magnetic circular dichroism. The STXM-XANES result strongly support the arguments that the origin of magnetization is attributable to the O  $2p$  orbitals rather than the Zn  $3d$  orbitals.

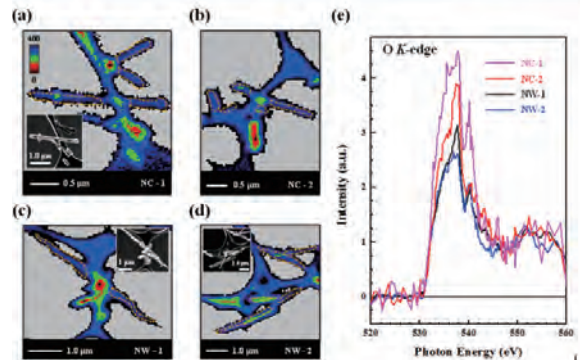


Fig. 1. (a)-(d) O  $K$ -edge STXM images of two selected regions in ZnO NC (NC-1 and NC-2) and NW (NW-1 and NW-2), respectively. (e) corresponding O  $K$ -edge XANES spectra of regions bordered by yellow dashed lines in ZnO NC (NC-1 and NC-2) and ZnO NW (NW-1 and NW-2). The insets show the corresponding SEM images.

- [1] T. A. Dietl *et al.*, Nat. Mater. **9** (2010) 965.
- [2] S. Z. Deng *et al.*, ACS Nano **4** (2010) 495.
- [3] J. W. Chiou *et al.*, Appl. Phys. Lett. **85** (2004) 3220.

BL4U

## STXM Study on Fluorescence Mechanism of Nanocarbon-Silica Composites

S. Kawasaki, Y. Ishii and H. Song

Nagoya Institute of Technology, Gokiso, Showa, Nagoya 466-8555, Japan

In order to solve the energy and environmental problems, we have to reduce our energy consumption. For that purpose, it is highly expected to replace the normal fluorescent lamps by LED lamps. However, it is not a very easy task, because the present white LED light does not have the same photoluminescence profile as normal fluorescent lamps have. To reproduce the good profile, we need fluorescent materials which can emit good white light under weak ultra-violet light produced by LED. Recently, we found that a kind of mesoporous carbon-silica composite can emit very broad white light.[1-3] The detailed mechanism of the PL property is not clarified yet. In order to elucidate the mechanism, electronic structures of nanocarbon fragments included in the light emitting mesoporous carbon-silica composites should be investigated.

We prepared several kinds of chemically modified nanocarbon materials such as oxidized carbon nanotubes, oxidized graphenes, carbon nanotubes including some functional molecules inside their hollow cores and so on. Oxygen K edge X-ray absorption spectra were observed using UVSOR BL4U Scanning Transmission X-ray Microscopy (STXM).

STXM observations of several kinds of nanocarbon materials were performed. Here, I report on the observation of the carbon nanotube sample in which anthraquinone molecules were encapsulated. The encapsulation of anthraquinone was carried out by exposing the SWCNT sample to anthraquinone gas in an evacuated glass tube. The open-end SWCNT sample and the organic molecule powder sample in the evacuated glass tube were heated at 200°C for 10 hours. After the heat-treatment, the SWCNT sample was washed several times with ethanol in order to remove the physically adsorbed organic molecules on the SWCNT surface. The encapsulation was confirmed by XRD and N<sub>2</sub> adsorption experiments. Figure 1 shows STXM spectra of the anthraquinone molecule sample and the carbon nanotube sample in which anthraquinone molecules were encapsulated (A@SWCNT). We could observe a peak of the anthraquinone sample at around 529 eV very clearly. On the other hand, for the A@SWCNT sample, two peaks were observed at around 529.2 eV and 531.5 eV. The latter peak was the absorption peak of polymer microgrids of TEM sample holder which was used to mount the A@SWCNT sample. Therefore, the peak position of anthraquinone molecule shifted from 529 eV to 529.2 eV by encapsulating it in carbon nanotubes. The energy shift

was occurred probably due to the charge transfer from nanotubes to anthraquinone molecules.

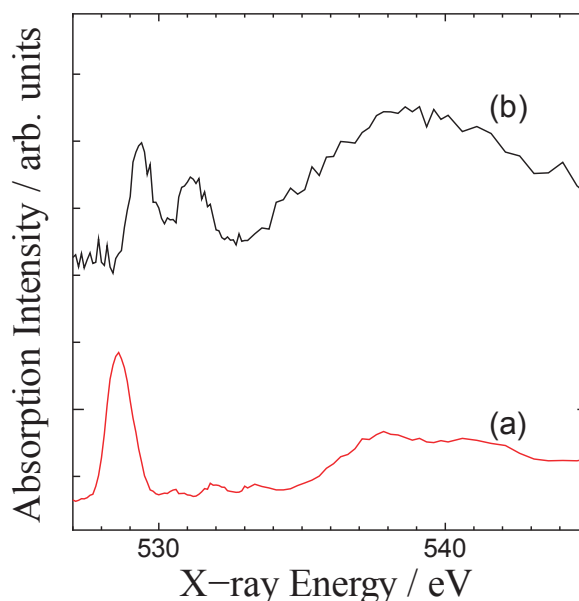


Fig. 1. Oxygen K-edge X-ray absorption spectra of (a) the anthraquinone molecule sample and (b) the A@SWCNT sample.

[1] Y. Ishikawa, S. Kawasaki, Y. Ishii, K. Sato and A. Matsumura, *Jpn. J. Appl. Phys.* **51**, 01AK02, (2012)

[2] Y. Ishikawa, K. Sato, S. Kawasaki, Y. Ishii, A. Matsumura and S. Muto, *physica status solidi (a)* **209** (2012) 1022.

[3] Y. Ishii, A. Matsumura, Y. Ishikawa and S. Kawasaki, *Jpn. J. Appl. Phys.* **50** (2011) 01AF06-1.

BL4U

## X-Ray Linear Dichroism of Sodium Titanate Nanoribbons Measured with *in situ* Azimuthal Sample Rotation in STXM

X. H. Zhu<sup>1</sup>, T. Ohigashi<sup>2</sup>, A. P. Hitchcock<sup>1</sup>, C. Bittencourt<sup>3</sup>, P. Umek<sup>4</sup> and P. Krüger<sup>5</sup>

<sup>1</sup>Brockhouse Institute for Materials Research, McMaster University, Hamilton, ON L8S 4M1, Canada

<sup>2</sup>UVSOR Facility, Institute for Molecular Science, Okazaki 444-8585, Japan

<sup>3</sup>University of Mons, 7000 Mons, Belgium

<sup>4</sup>Institute Jožef Stefan, 1000 Ljubljana, Slovenia

<sup>5</sup>Graduate School of Advanced Integration Science, Chiba University, Chiba 263-8522, Japan

Titanate nanostructures are potential active materials in applications such as lithium ion batteries, gas sensors, photocatalysts, and dye sensitized solar cells [1]. This study used scanning transmission X-ray microscopy (STXM) to investigate the electronic structure of sodium titanate nanoribbons ( $\text{NaTiO}_x\text{-NR}$ ) prepared by hydrothermal treatment of anatase  $\text{TiO}_2$  [2]. We measured the Ti 2p and O 1s absorption spectra and X-ray linear dichroism (XLD) of individual nanoribbons using a newly implemented *in situ* azimuthal sample rotation device. While XLD in  $\text{NaTiO}_x\text{-NR}$  has been studied previously in a full field microscope [3], the ability to examine XLD of an identical nanostructure is an advantage of the STXM approach. Figure 1 is a STXM image of the sample, and images of the 6 orientations at which Ti 2p and O 1s image sequences (stacks) were measured.

Figure 2 presents O 1s spectra of a small portion of one nanoribbon extracted from the aligned optical density (OD) O 1s stacks. Through careful energy calibration an apparent energy shift in the lowest energy band was identified. This shift is caused by differences in the XLD of two adjacent states (split  $t_{2g}$

band). A similar apparent shift in the Ti  $2p_{3/2} \rightarrow t_{2g}$  band was noted previously, and reproduced in this work (not shown). The Ti 2p and O 1s stacks can be reduced to dichroic maps by fitting to spectra characteristic of the sample parallel and perpendicular to the fixed horizontal E-vector, as shown in Fig. 3 for one orientation of the O 1s data. Detailed analysis and comparison to the results of multichannel multiple scattering with atomic multiplet (Ti 2p) and density functional (O 1s) calculations by Krüger (Chiba) is in progress.

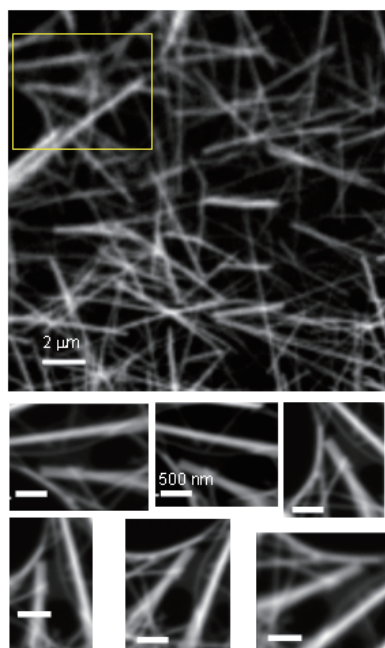


Fig. 1. STXM OD image at 460 eV of the  $\text{NaTiO}_x$  nanorod sample. The yellow box is the area for XLD study using *in situ* azimuthal rotation. Lower panel is average O 1s stacks for the 6 orientations.

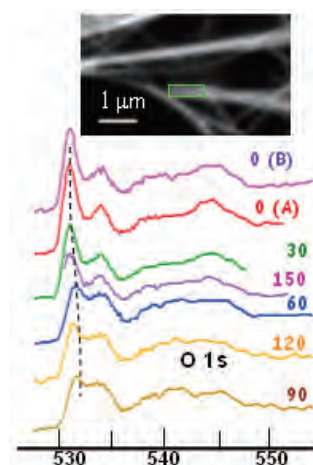


Fig. 2. O 1s spectra as a function of angle between sample and E-vector for the region in the green box.

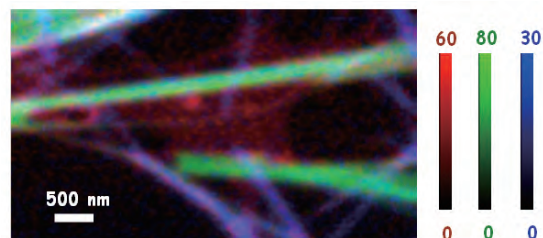


Fig. 3. Color composite of component maps (holey carbon support, parallel, perpendicular) from singular value decomposition analysis of an O 1s stack.

[1] D. Walsh *et al.*, *Titanate and Titania nanotubes*. (Cambridge Univ. Press, 2009)

[2] P. Umek *et al.*, *J. Nanosci. & Nanotech.* 7 (2007) 3502.

[3] P. Guttman *et al.*, *Nature Photonics* 6 (2011) 25.

BL4U

## The Influence of N $2p$ Vacancy on the Electronic Structure of ( $p$ , $n$ )-Type GaN Nanowires Studied by Scanning Transmission X-Ray Microscopy

Y. F. Wang<sup>1</sup>, W. F. Pong<sup>1</sup>, L. W. Tu<sup>2</sup>, J. W. Chiou<sup>3</sup>, T. Ohigashi<sup>4</sup> and N. Kosugi<sup>4</sup>

<sup>1</sup>Department of Physics, Tamkang University, Tamsui 251, Taiwan

<sup>2</sup>Department of Physics, National Sun Yat-Sen University, Kaohsiung 804, Taiwan

<sup>3</sup>Department of Applied Physics, National University of Kaohsiung, Kaohsiung 811, Taiwan

<sup>4</sup>Editorial Board, UVSOR Facility, Institute for Molecular Science, Okazaki 444-8585, Japan

In this report, scanning transmission X-ray microscopy (STXM) was utilized to investigate the effect of N  $2p$  vacancy on the electronic structure of  $p$ - and  $n$ -type GaN, which were grown on the same piece of nanowire top and bottom area, respectively. As shown in Fig. 1, the scanning electron microscope (SEM) measurement revealed that GaN nanowires were  $\sim 1500$  nm long and  $\sim 50$  nm in diameter. Figure 2 presents the N  $K$ -edge STXM and corresponding x-ray absorption near-edge structure (XANES) spectra of the ( $p$ ,  $n$ )-type GaN. The experiments were performed at the 4U beamline. The N  $K$ -edge STXM stack mappings were recorded at two selected regions in GaN nanowire top ( $p$ -type-1 and  $p$ -type-2) and bottom ( $n$ -type-1 and  $n$ -type-2) regions (see Fig. 2a). To overcome the signal-to-noise ratio of the XANES spectra obtained from specific mapping areas in the STXM images, the N  $K$ -edge STXM-XANES spectra in Fig. 2(b) were obtained as the sum of the XANES spectra in the regions that are bordered by white color, as shown in  $p$ -type-1,  $p$ -type-2,  $n$ -type-1, and  $n$ -type-2. According to the dipole-transition selection rule, the features at  $\sim 398$ - $413$  eV are attributed to the electron excitations from N  $1s$ -derived states to  $2p_{x,y}$ -derived (along the bilayer) and N  $2p_z$ -derived (along the  $c$  axis) states, which are approximately proportional to the density of the unoccupied N  $2p$ -derived states.<sup>1</sup> The intensities of the N  $K$ -edge STXM-XANES spectra of  $p$ -type GaN are significantly higher than those of  $n$ -type GaN, which reflects the increase in the number of unoccupied N  $2p$ -derived states. In other words, the STXM-XANES results demonstrate that the population of defects at the N sites in  $p$ -type is larger than in the  $n$ -type and confirming the enhanced density of states of N  $2p$ -derived states, as the population of defects and dangling bonds at/above  $E_{\text{CBM}}$  or  $E_{\text{F}}$  in  $p$ -type GaN exceeds that in the  $n$ -type GaN. The STXM-XANES results intensely support the arguments that the amount of N  $2p$  vacancy affects the electric conductivity, carrier concentration, and carrier mobility of  $p$ -type GaN nanowires.

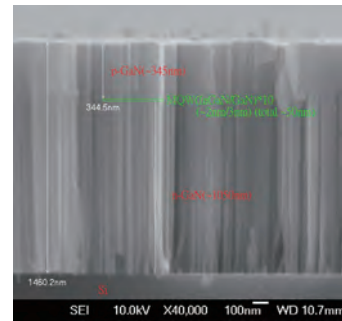


Fig. 1. SEM image of the GaN nanowires. The  $p$ - and  $n$ -type GaN were grown on the nanowire top and bottom area, respectively.

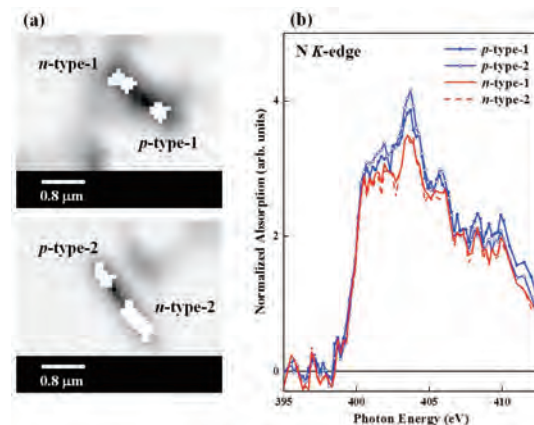


Fig. 2. (a) N  $K$ -edge STXM images of two selected regions in GaN nanowire top ( $p$ -type-1 and  $p$ -type-2) and bottom ( $n$ -type-1 and  $n$ -type-2), respectively. (b) The corresponding N  $K$ -edge XANES spectra of the top ( $p$ -type-1 and  $p$ -type-2) and bottom ( $n$ -type-1 and  $n$ -type-2) regions.

[1] J. W. Chiou *et al.*, Appl. Phys. Lett. **81** (2002) 3389.

BL4U

## Comprehensive Characterization of Monolithic Polymers by Scanning Transmission X-Ray Microscopy (STXM)

D. Arrua<sup>1</sup>, T. Ohigashi<sup>2</sup>, Y. F. Wang<sup>2</sup>, J. Hoon<sup>1</sup>, N. Kosugi<sup>2</sup> and E. Hilder<sup>1</sup>

<sup>1</sup> Australian Centre for Research on Separation Science (ACROSS), School of Chemistry, University of Tasmania, Private Bag 75, Hobart 7001, Australia

<sup>2</sup> UVSOR Facility, Institute for Molecular Science, Okazaki 444-8585, Japan

Monolithic polymers are a new generation of stationary phases for chromatography, offering significant benefits over currently particle-based materials. The main characteristic of these materials is the presence of large through-pores which permits the use of high flow rates at low backpressures [1]. However, improvements in this technology rely on being able to accurately characterize the porous structure and new characterization techniques are needed to better understand the polymer morphology and its optimization. In this sense, the relatively high penetration power of X-rays would allow a comprehensive analysis of the radial and longitudinal heterogeneity of the monolithic materials developed in our research group.

The characterization by STXM of polymer monoliths was performed at the BL4U beamline of the UVSOR synchrotron radiation facility. To obtain a suitable sample for STXM studies, the macroporous methacrylate monolith with encapsulated divinylbenzene (DVB) nanoparticles was embedded with an aliphatic epoxy resin specially designed for STXM analysis [2]. The experiments were performed at the O 1s edge. Figure 1 shows the O 1s NEXAFS spectra for the polymer monolith and the embedding resin. The spectrum for the methacrylate scaffold has a peak at 531 eV which is characteristic of the O 1s  $\rightarrow \pi^*_{C=O}$  transition in esters. The O 1s spectrum of the epoxy resin has little or no absorption at this energy and therefore there is good contrast between the resin and the polymeric scaffold. The DVB nanoparticles were not possible to be observed due to lack of contrast at the O edge.

Figure 2 shows color-coded composite maps of the porous polymer embedded with the epoxy resin. These color coded composites display the spatial distribution of the polymer scaffold relative to the embedding resin.

Ongoing studies in our research group are focused in the characterization of polymer monoliths containing nanostructures with different functionality and the use of other photon energies (e.g. C 1s and N 1s) to get a better understanding of the distribution of the nanostructures within the polymeric scaffold.

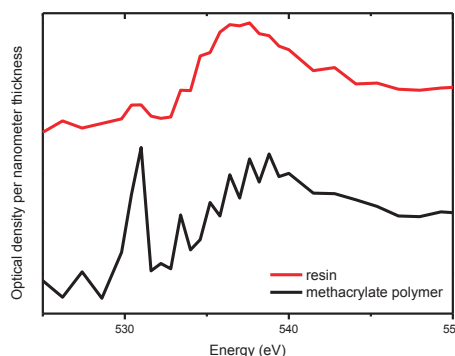


Fig. 1. NEXAFS spectra of the methacrylate scaffold (black) and the TTE epoxy resin (red).

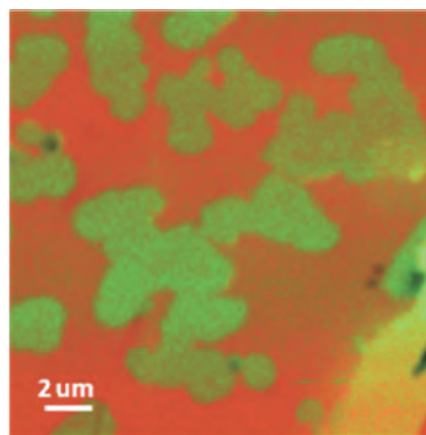


Fig. 2. Color composite of STXM derived component maps of methacrylate-based polymer (green) and TTE resin (orange).

[1] R. D. Arrua *et al.*, *Analyst* **137** (2012) 5179.

[2] A. P. Hitchcock *et al.*, *J. Electron Spectrosc.* **156** (2007) 467.

BL4B

## O K-Edge XAS of Electrocatalytic Manganese Oxide

Y. Aoki<sup>1,2</sup>, K. Kikutani<sup>1</sup>, E. Tsuji<sup>1</sup> and H. Habazaki<sup>1</sup>

<sup>1</sup>Faculty of Engineering, Hokkaido University, Sapporo 060-8628, Japan

<sup>2</sup>PRESTO, JST, Kawaguchi 332-0012, Japan

In naturally occurring photosystem II (PSII), the water oxidation reaction proceeds with extraordinary high catalytic activity, where a  $\mu$ -oxo bridged tetrameric Mn cluster ( $\text{Mn}_4\text{CaO}_5$ ) serves as the multielectron oxidation catalyst within a complex protein environment [1, 2]. Thus, the Mn clusters of photosynthetic organisms have triggered extensive research efforts to develop efficient water oxidation catalysts composed of the inexpensive and abundant element Mn. In a recent year, various manganese oxides, such as  $\text{MnO}_2$ ,  $\text{BaMnO}_3$ ,  $\text{LaMnO}_3$  etc. has been reported to show an excellent electrocatalytic properties for oxygen evolution by electrochemical water splitting [3, 4]. Suntivich *et al* reported that hole on oxygen make an important role for oxygen evolution catalysis of manganese oxide [4]. Such a hole probably evolves by mixing of ligand-to-metal charge transfer state related to the covalency of Mn-O bonding. O K-edge XAS spectroscopy can direct evidence of unoccupied state of solids. Accordingly, it is of fundamental and technological important to study the manganese oxide system by using this technique in order to clarify the relationship between oxygen hole and electrocatalysis. In this study, we investigate O K-edge spectra of various manganese oxide and those of peroxide and superoxide.

Here, the O K-edge spectra of manganese oxides  $\text{KMn}^{\text{VII}}\text{O}_4$ ,  $\text{BaMn}^{\text{IV}}\text{O}_3$  and  $\text{Mn}^{\text{IV}}\text{O}_2$  were measured.  $\text{KMnO}_4$  and  $\text{MnO}_2$  were purchased from Aldrich and  $\text{BaMnO}_3$  was prepared by solid state reaction. The spectra of  $\text{MgO}$ ,  $\text{BaO}_2$  and  $\text{KO}_2$  were measured as a reference of oxide ( $\text{O}^{2-}$ ), peroxide ( $\text{O}^-$ ) and superoxide ( $\text{O}_2^-$ ). The powder specimens were attached to the folder with carbon tape and to measure the adsorption by total electron yield method.

O K-edge XAS spectra of the manganese oxide samples were shown in Fig. 1(a). The Mn atoms in  $\text{MnO}_2$  and  $\text{BaMnO}_3$  take octahedral coordination with oxygen atoms. Therefore, the two peaks near O K-edge at around 529 and 531 eV can be assigned to the transition anti-bonding  $t_{2g}$  and  $e_g$  states, respectively. In case of  $\text{KMnO}_4$ , the Mn-O clusters take tetrahedral coordination, so that the peaks at around 528 and 530 eV can be assigned to the transition to anti-bonding  $t_2$  and  $e$  symmetric states, respectively.

The O K-edge spectra are clearly changed by changing oxidation state of oxide anions, as shown in Fig. 1(b). The peroxide and superoxide show clear pre-edge peak at around 529 eV, provably due to the antibonding O-O states, even though  $\text{MgO}$  does not

show pre-edge features because of strong ionic character of Mg-O bonding.

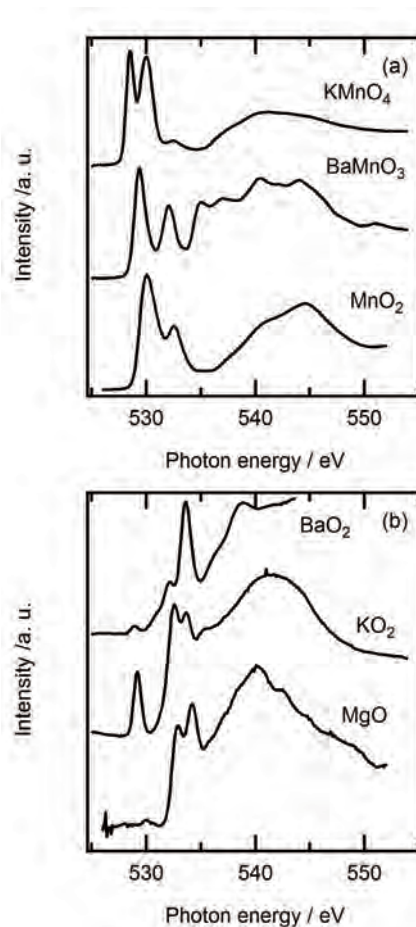


Fig. 1. O K-edge spectra of (a) various manganese oxides and (b) oxides with various oxidation state of O atoms.

[1] J. H. Alstrum-Acevedo *et al.*, *Inorg. Chem.* **44** (2005) 6802.

[2] G. C. Dismukes, R. Brimblecombe, G. A. N. Felton, R. S. Pryadun, J. E. Sheats, L. Spiccia and G. F. Swiegers, *Acc. Chem. Res.* **42** (2009) 1935.

[3] F. Jiao and H. Frei, *Energy Environ. Sci.* **3** (2010) 1018.

[4] J. Suntivichi *et al.*, *J. Phys. Chem. C* **118** (2014) 1856.

BL4B

## Correlation between Oxygen Functional Groups and Magnetic Properties in Graphene Oxides Using X-Ray Magnetic Circular Dichroism

Y. F. Wang<sup>1</sup>, S. B. Singh<sup>1</sup>, J. W. Chiou<sup>2</sup>, W. F. Pong<sup>1</sup>, Y. Takagi<sup>3</sup> and T. Yokoyama<sup>3</sup>

<sup>1</sup>Department of Physics, Tamkang University, Tamsui 251, Taiwan

<sup>2</sup>Department of Applied Physics, National University of Kaohsiung, Kaohsiung 811, Taiwan

<sup>3</sup>Editorial Board, UVSOR Facility, Institute for Molecular Science, Okazaki 444-8585, Japan

In present study, three different samples i.e. graphene oxide (GO), medium reduce graphene oxide (MRGO) and highly reduce graphene oxide (HRGO) were studied using x-ray magnetic circular dichroism (XMCD) technique. Magnetic study (M-H loop) shows room temperature ferromagnetism in GO sample whereas gradual increases of paramagnetic contribution were observed after photo-thermal reduction process (in MRGO and HRGO samples). Figures 1a and 1b display the C and O *K*-edge XMCD spectra respectively, with the photo-helicity of incident x-rays parallel ( $\mu^+$ ) and anti-parallel ( $\mu^-$ ) to the direction of magnetization of the GO sample. The XMCD experiments were performed at the 4B beamline. In Fig. 1a (top panel), spectral features observed in the regions 283-289 eV and 289-315 eV are ascribed to C  $1s \rightarrow \pi^*$  and C  $1s \rightarrow \sigma^*$  transitions, respectively. The difference was observed in both  $\pi^*$ - and  $\sigma^*$ -states when applied the magnetic field in opposite directions (see bottom panel). In Fig. 1b (top panel), spectral features observed in the regions 528-535 eV and 535-545 eV are ascribed to O  $1s \rightarrow \pi^*$  and O  $1s \rightarrow \sigma^*$  transitions, respectively. The XMCD signal was also observed in O *K*-edge when applied the magnetic field in opposite directions (bottom panel, see Fig. 1b). The origin of XMCD signal confirms that oxygen functional groups playing important role in origin of magnetism in GO sample. The presence of various oxygen functional groups were clearly observed in x-ray photoelectron spectroscopy and scanning transmission x-ray microscopy study in GO sample. The presence of oxygen functional groups on GO surface was related to ferromagnetism, whereas consumption of oxygen functional groups after photo-thermal reduction process was related to paramagnetic contribution in MRGO and HRGO samples.

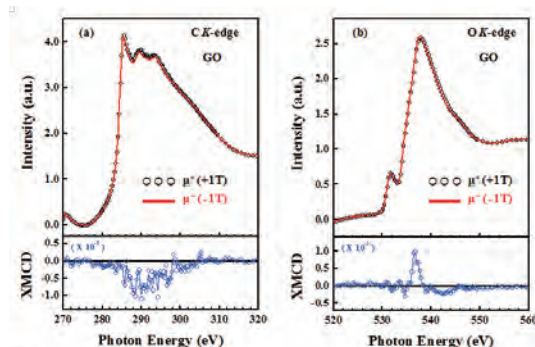


Fig. 1. **a**) (Top panels) display the C *K*-edge x-ray absorption near-edge structure (XANES) spectra of GO sample, with the photo-helicity of incident x-rays parallel ( $\mu^+$ ) and anti-parallel ( $\mu^-$ ) to the direction of magnetization. Bottom panel represents the XMCD spectra of GO sample. **b**) (Top panels) display the O *K*-edge XANES spectra of GO sample, with the photo-helicity of incident x-rays parallel ( $\mu^+$ ) and anti-parallel ( $\mu^-$ ) to the direction of magnetization. Bottom panel represents the XMCD spectra of GO sample.

[1] M. Weser *et al.*, Phys. Chem. Chem. Phys. **13** (2011) 7534.

[2] A. Ganguly *et al.*, J. Phys. Chem. C **115** (2011) 17009.

BL4B

## Investigation on Electrochemical Property of Al<sub>2</sub>O<sub>3</sub>-Coated Li-Excess Mn-Based Layered Positive Electrode Material

T. Okumura<sup>1</sup>, M. Shikano<sup>1</sup>, K. Takada<sup>2</sup> and H. Kobayashi<sup>1,2</sup>

<sup>1</sup>Research Institute for Ubiquitous Energy Devices, National Institute of Advanced Industrial Science and Technology (AIST), Ikeda, 563-8577, Japan

<sup>2</sup>Faculty of Chemistry, Materials and Bioengineering, Kansai University, Suita, 564-8680, Japan

The layered Li<sub>2</sub>MnO<sub>3</sub>-LiMO<sub>2</sub> (*M* = transition metal) materials are one of the promising positive electrode materials for lithium secondary battery. Especially, it has been reported that Li[Mn<sub>0.56</sub>Ni<sub>0.17</sub>Co<sub>0.07</sub>Li<sub>0.2</sub>]O<sub>2</sub> displayed an initial discharge capacity of ca. 280 mAh/g in the voltage range of 2.5 to 4.8 V and maintained a reversible capacity of ca. 250 mAh/g after 50 cycles. On the other hand, the decomposition of the electrolyte proceeded on the positive electrode material above 4.5 V is a problem to be solved for realizing long cycle life. Recently several efforts have been made to improve the cycle performance through surface modification of positive electrode materials, but limited efforts have been made to improve the cycle performance through surface modification of Li-excess Mn-based layered materials. In this paper, the effect of Al<sub>2</sub>O<sub>3</sub>-coating on electrochemical properties was studied in Li<sub>1.20</sub>Mn<sub>0.55</sub>Ni<sub>0.16</sub>Co<sub>0.09</sub>O<sub>2</sub>.

Surface modified-Li<sub>1.20</sub>Mn<sub>0.55</sub>Ni<sub>0.16</sub>Co<sub>0.08</sub>O<sub>2</sub> was prepared by mechanochemical reaction with nano-Al<sub>2</sub>O<sub>3</sub> using NOB-MINI (Hosokawa Micron Co.). The particle morphology was measured by SEM. Crystal and electronic structures were investigated by synchrotron XRD (BL19B2 at SPring-8) and XAFS (BL7C at PF, BL4B at UVSOR, and BL27SU at SPring-8) measurements. The crystal structure and bondlength were determined using the analysis programs RIETAN-FP and REX2000. Electrochemical property was measured using coin-type cells with Li/1M LiPF<sub>6</sub> in EC:DMC(1:2)/samples

The XRD and SEM results showed that the 5wt% Al<sub>2</sub>O<sub>3</sub>-coated sample (Test conditions; 2000 rpm and 5 min.) was well defined layered phase without additional impurity peak and the Al<sub>2</sub>O<sub>3</sub> particles with the order of 10-20 nm were uniformly distributed over the surface of Li<sub>1.20</sub>Mn<sub>0.55</sub>Ni<sub>0.16</sub>Co<sub>0.08</sub>O<sub>2</sub> particles. The hard X-ray XAFS results clarified that both pristine and 5wt% Al<sub>2</sub>O<sub>3</sub>-coated samples showed almost the same valence states of *M* cations. These results indicated that the mechanochemical reaction gave no damage to the bulk structure of Li<sub>1.20</sub>Mn<sub>0.55</sub>Ni<sub>0.16</sub>Co<sub>0.09</sub>O<sub>2</sub>. On the other hands, the soft X-ray XANES results clarified that the surface of Li<sub>1.20</sub>Mn<sub>0.55</sub>Ni<sub>0.16</sub>Co<sub>0.09</sub>O<sub>2</sub> was covered by Al<sub>2</sub>O<sub>3</sub> particles as shown in Fig. 1. Electrochemical tests showed that the cycle dependence of discharge capacity retention at 318 K was improved for the 5wt% Al<sub>2</sub>O<sub>3</sub>-coated sample as shown in Fig. 2. In

this paper, it is revealed that the mechanochemical Al<sub>2</sub>O<sub>3</sub>-coating process is an effective way of improving the cycle performance at high temperature.

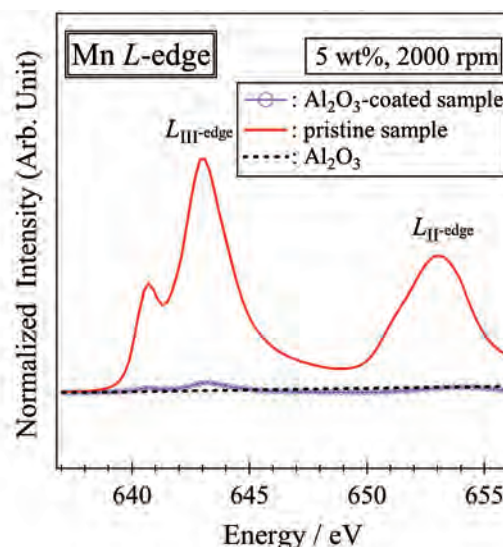


Fig. 1. Mn *L*-edge XANES spectra for pristine and Al<sub>2</sub>O<sub>3</sub>-coated samples together with Al<sub>2</sub>O<sub>3</sub>.

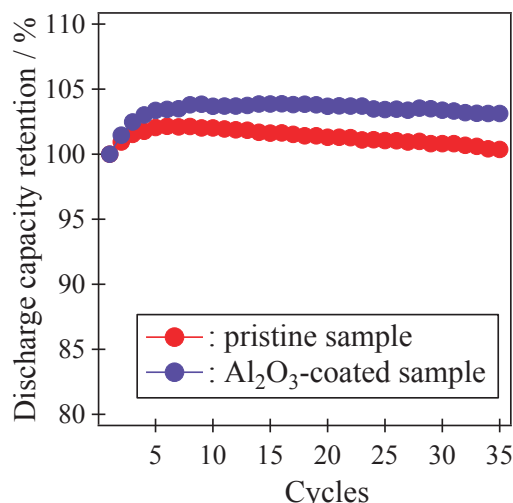


Fig. 2. Cycle dependence of discharge capacity retention at 318 K for pristine and Al<sub>2</sub>O<sub>3</sub>-coated samples.

[1] A. Ito *et al.*, *J. Power Sources* **183** (2008).

[2] H. Kobayashi *et al.*, *Solid State Ionics*  
DOI: 10.1016/j.ssi.2013.09.045.

BL4B

## Valence State Analysis of Mn and Fe Ions in $\text{Bi}_4\text{Ti}_3\text{O}_{12}$

K. Nishimura<sup>1</sup>, T. Yoshioka<sup>1</sup> and T. Yamamoto<sup>1,2</sup>

<sup>1</sup>Faculty of Science and Engineering, Waseda University, Shinjuku 169-8555, Japan

<sup>2</sup>Institute of Condensed-Matter Science, Waseda University, Shinjuku 169-8555, Japan

Dilute Magnetic Materials (DMMs) have been extensively investigated because of their potential applications in spintronics. Recently, it was reported that  $\text{Bi}_4\text{Ti}_3\text{O}_{12}$  doped with dilute Fe ions show both ferroelectric and ferromagnetic properties, i.e., multiferroic property, at room temperature [1]. Although it is essential to know the local environment of doped magnetic ions for the understandings of the mechanism of room-temperature ferromagnetism, such analysis has often been skipped for DMMs. We have studied Mn and Fe codoped  $\text{In}_2\text{O}_3$  by the analysis of X-ray absorption spectra (XAS) [2, 3]. In the current study, the valence state of Mn and Fe ions in  $\text{Bi}_4\text{Ti}_3\text{O}_{12}$  is investigated by the Mn- and Fe- $L_{2,3}$  XAS measurements.

All the samples were synthesized by the solid-state reaction method changing concentrations of doped Mn and Fe ions. Reagent grade powders of  $\text{Bi}_2\text{O}_3$ ,  $\text{TiO}_2$ ,  $\text{Mn}_2\text{O}_3$  and  $\text{Fe}_2\text{O}_3$  were mixed and ground in an agate mortar, which were calcined at 1023 K for 5 hours in air. Resultant powders were remixed and reground, and pressed into a cylindrical pellet form, which were sintered at 1223 K for 5 hours in air.

Mn- and Fe- $L_{2,3}$  XAS were collected at BL4B in UVSOR by total electron yield method. Sample powders were mounted on the first Cu-Be dinode of the electron multiplier using carbon adhesive tape. Synchrotron radiation from the storage ring was

monochromatized by a varied-line-spacing plane grating (800 lines/mm). Energy resolution ( $E/\Delta E$ ) of the incident beam was set to 3000.

Observed Mn- and Fe-  $L_{2,3}$  XAS are shown in Figs. 1(a) and (b), respectively, with those of metal oxides for comparisons. Mn- $L_3$  XAS of Mn-doped  $\text{Bi}_4\text{Ti}_3\text{O}_{12}$  shows similar profile as that of  $\text{MnO}_2$ , which indicates that valence state of Mn ions in  $\text{Bi}_4\text{Ti}_3\text{O}_{12}$  are 4+. On the other hand, that of Fe ions can be determined as 3+ by the same comparisons in Fig. 1(b).

In summary, we have successfully determined the valence states of doped dilute Mn and Fe ions in  $\text{Bi}_4\text{Ti}_3\text{O}_{12}$  by XAS analysis.

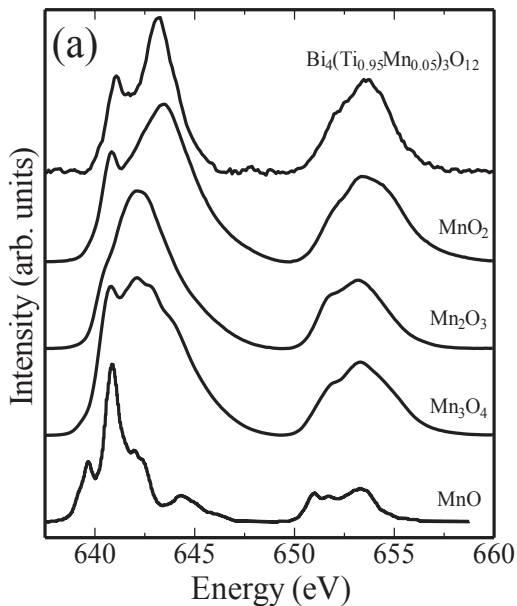


Fig. 1(a). Observed Mn- $L_{2,3}$  XAS of Mn-doped  $\text{Bi}_4\text{Ti}_3\text{O}_{12}$  and those of Mn oxides.

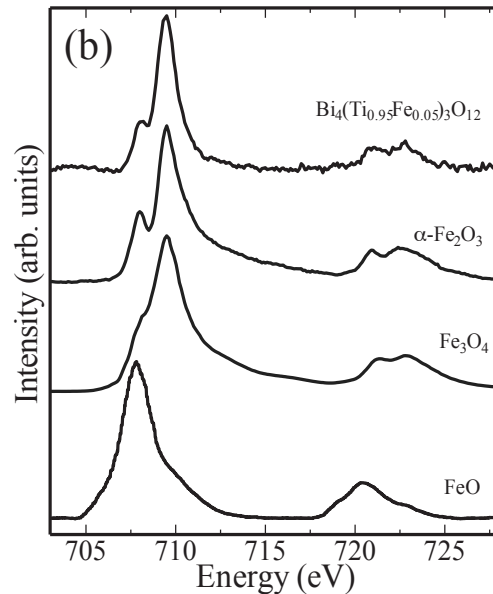


Fig. 1(b). Observed Fe- $L_{2,3}$  XAS of Fe-doped  $\text{Bi}_4\text{Ti}_3\text{O}_{12}$  and those of Fe oxides.

[1] X. Q. Chen *et al.*, Solid State Comm. **150** (2010) 1221.

[2] T. Okazaki *et al.*, Solid State Comm. **151** (2011) 1749.

[3] S. Nishida *et al.*, UVSOR Activity Reports 2012, (2013) 99.

BL5U

## Electronic Structures of the ZrNiSn Half-Heusler Thermoelectric Material

H. Miyazaki<sup>1</sup>, T. Nakano<sup>2</sup>, M. Inukai<sup>2</sup>, K. Soda<sup>3</sup> and Y. Nishino<sup>2</sup>

<sup>1</sup>Center for Fostering Young and Innovative Researchers, Nagoya Institute of Technology, Nagoya 466-8555, Japan

<sup>2</sup>Department of Frontier Materials, Nagoya Institute of Technology, Nagoya 466-8555, Japan

<sup>3</sup>Department of Quantum Engineering, Graduate School of Engineering, Nagoya University, Nagoya 464-8603, Japan

Half-Heusler  $M\text{NiSn}$  and  $M\text{CoSb}$  ( $M = \text{Ti, Zr, Hf}$ ) alloys with a valence electron count of 18 are considered to be semiconductors with a narrow band gap [1] and a promising class of thermoelectric materials with their large dimensionless figure of merit  $ZT$  [2, 3]. Numerous half-Heusler ZrNiSn-based alloys have been investigated, and  $ZT$  values of 0.52 (p-type) and 1.0 (n-type) (at 1000 K) have been reported for the  $\text{Zr}_{0.5}\text{Hf}_{0.5}\text{CoSb}_{0.8}\text{Sn}_{0.2}$  [2] and  $\text{Zr}_{0.4}\text{Hf}_{0.6}\text{NiSn}_{0.98}\text{Sb}_{0.02}$  [3] alloys, respectively. Although the optimization of the thermoelectric performance of half-Heusler ZrNiSn-based alloys has been extensively investigated, the mechanism by which the thermoelectric properties are improved has not been clarified. To clarify the origin of the large thermoelectric properties, we investigate the electronic structures of the ZrNiSn alloy by photoemission spectroscopy (PES).

Soft X-ray and ultraviolet PES measurements were performed using the BL27SU and BL5U beamlines at the SPring-8 and UVSOR-III synchrotron radiation facilities. Clean surfaces for the PES measurements were obtained by *in-situ* fracturing with a knife edge at 10 K under ultra-high vacuum. The Fermi level ( $E_F$ ) and total energy resolution were determined by the Fermi edge of evaporated gold films. The total energy resolutions were set to 160 and 50 meV at the excitation photon energies ( $h\nu$ ) of 1000 and 50 eV, respectively.

Figure 1(a) shows the photon-energy-dependent valence band spectra and density of states (DOS) determined by electronic band structure calculations using a theoretical lattice parameter of  $a = 6.154 \text{ \AA}$ . The experimental spectra are normalized with respect to their integrated intensity on the whole valence band up to  $E_B = 12 \text{ eV}$ . The overall features of the photoemission spectra of ZrNiSn are in good agreement with the DOS results, even though a shift to higher binding energies is observed compared with the predicted values. Figures 1(b) shows the photoemission spectra near  $E_F$  at  $h\nu = 50$  for the ZrNiSn alloy and a Au film. The intensity of the photoemission spectra of the Au film gradually decreases from 0.4 eV to a value near the  $E_F$  and changes as a Fermi distribution curve at the  $E_F$ . The bandgap was not observed in the photoemission spectra within the total energy resolution of the present measurements. The observed intensity at  $E_F$

and the inflection point suggests the existence of a semi-metallic in-gap state, that is to say, pseudo-gap, which is inconsistent with the predicted semiconductor-like band structure for the ZrNiSn alloy [1].

Thus, an improvement in the thermoelectric properties can be achieved by material design based on the pseudo-gap electronic structure of half-Heusler ZrNiSn-based alloys.

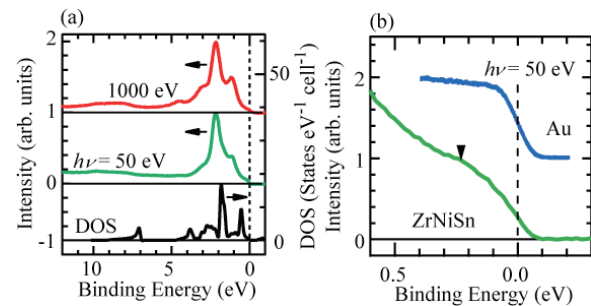


Fig. 1. (a) Photoemission spectra at excitation-photon energies  $h\nu$  of 50 and 1000 eV, and calculated DOS for the ZrNiSn alloy. (b) Photoemission spectra near the Fermi edge at  $h\nu = 50$  eV for the ZrNiSn alloy and a Au film.

[1] J. Tobola *et al.*, J. Phys. Condens. Mat. **10** (1998) 1013.

[2] S.R. Culp *et al.*, Appl. Phys. Lett. **93** (2008) 022105.

[3] C. Yu *et al.*, Acta Mater. **57** (2009) 2757.

BL5U

## Metal-Insulator Transition in Pyrite-Type $\text{Ni}_{1-x}\text{Cu}_x\text{S}_2$

K. Usui<sup>1</sup>, S. Osawa<sup>2</sup>, H. Kondo<sup>1</sup>, M. Kato<sup>1,2</sup>, J. Iwasaki<sup>3</sup>, K. Niwa<sup>2,3</sup>, K. Kusaba<sup>2,3</sup>,  
M. Hasegawa<sup>2,3</sup> and K. Soda<sup>1,2</sup>

<sup>1</sup>Department of Quantum Engineering, Graduate School of Engineering, Nagoya University,  
Nagoya 464-8603, Japan

<sup>2</sup>Department of Physical Science and Engineering, School of Engineering, Nagoya University,  
Nagoya 464-8603, Japan

<sup>3</sup>Department of Crystalline Materials Science, Graduate School of Engineering, Nagoya University,  
Nagoya 464-8603, Japan

Pyrite-type transition-metal dichalcogenides  $\text{MX}_2$  exhibit rich variety of electronic and magnetic properties due to the electron correlation and hybridization effects. In particular,  $\text{NiS}_2$  is classified as a charge-transfer-type insulator [1], while  $\text{CuS}_2$  is a p-band metal, showing superconductivity [2]. It is interesting to clarify the effects of solid solution between insulating  $\text{NiS}_2$  and metallic  $\text{CuS}_2$  on the electronic structure and related properties. In this study we have studied the valence band spectra near the Fermi level  $E_F$  of  $\text{Ni}_{1-x}\text{Cu}_x\text{S}_2$  to clarify the origin of the  $x$ -dependence of their electronic properties.

Photoelectron measurements were carried out at 10 K in angle-integrated mode. Specimens of  $\text{Ni}_x\text{Cu}_{1-x}\text{S}_2$  were polycrystals synthesized under a high pressure of 6.5 GPa at a temperature of  $\sim 920$  K with use of multi-anvil cell. Their clean surfaces were prepared for the measurement by scraping them with a diamond file. Total energy resolution was estimated as  $\sim 0.1$  eV at the excitation photon energy of 60 eV. The origin of the binding energy  $E_B$  was set to the Fermi energy  $E_F$  determined by measuring the Fermi edge of an evaporated Au film on the sample holder.

Typical valence-band spectra near  $E_F$  of  $\text{Ni}_x\text{Cu}_{1-x}\text{S}_2$  are compared with each other in Fig.1. Numerals in the right-hand side of the figure show the intensity at  $E_F$  normalized with the intensity (*i.e.* the edge jump) linearly extrapolated from the spectral intensity between  $E_B = 0.2 \sim 0.3$  eV to  $E_F$ . The normalized intensity at  $E_F$  is  $\sim 0.5$  of the edge jump for  $\text{CuS}_2$ , indicating its metallic nature, gradually decreases with the Cu content  $x$  decreasing, and becomes  $\sim 0.2$  for  $\text{NiS}_2$ , suggesting that  $\text{NiS}_2$  has a semimetallic or semiconducting (insulating) feature, as reported [2, 3]. For  $\text{NiS}_2$ , fine structures are also recognized near  $E_F$ , which might imply that  $\text{NiS}_2$  is not a simple semiconductor.

Figure 2 shows the electric conductivity at 300 K for  $\text{Ni}_{1-x}\text{Cu}_x\text{S}_2$  in comparison with the spectral intensity at  $E_F$ . The conductivity decreases gradually as the Cu content  $x$  reduces from 1 to 0.1, and then steeply from  $x = 0.1$  to 0, qualitatively consistent with the  $x$ -dependence of the spectral intensity at  $E_F$ ; the metal-insulator transition occurs between  $x = 0$  and 0.1. Here we propose a mechanism for the metal-insulator transition as follows; holes are

injected into the  $\text{S}3p$ -derived fully-occupied valence band of Mott-insulating  $\text{NiS}_2$  from the metallic  $\text{S}3p$ -band (or states) of  $\text{CuS}_2$ . Hence the substitution of Cu for Ni may make  $\text{Ni}_{1-x}\text{Cu}_x\text{S}_2$  metallic in a wide Cu content  $x$  range.

Cu and Ni 2p core-level spectroscopy will provide further support to the above-mentioned mechanism.

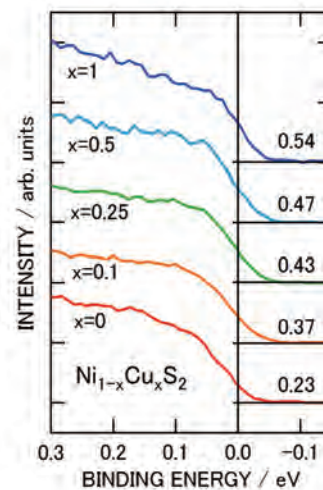


Fig. 1. Photoelectron spectra near  $E_F$  of  $\text{Ni}_{1-x}\text{Cu}_x\text{S}_2$ .

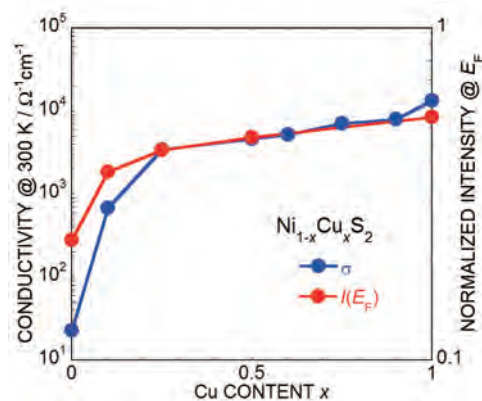


Fig. 2. Electric conductivity and spectral intensity at  $E_F$  of  $\text{Ni}_{1-x}\text{Cu}_x\text{S}_2$ .

[1] J. Kunes *et al.*, Phys. Rev. B **81** (2010) 025122.

[2] H. Ueda *et al.*, Phys.Rev.B **65** (2002) 155104.

[3] K. Mamiya *et al.*, Phys. Rev. B **58** (1998) 9611.

BL5U

## Angle-Resolved Photoemission Study of Insulator-to-Metal Transition of $\text{Sm}_{1-x}\text{Y}_x\text{S}$

M. Kaneko<sup>1,2</sup>, M. Sato<sup>3</sup>, T. Ito<sup>1,4</sup>, K. Imura<sup>3</sup>, T. Hajiri<sup>1,2</sup>,  
M. Matsunami<sup>2,5</sup>, S. Kimura<sup>2,6</sup>, H. S. Suzuki<sup>7</sup> and N. K. Sato<sup>3</sup>

<sup>1</sup>Graduate School of Engineering, Nagoya University, Nagoya 464-0818, Japan

<sup>2</sup>UVSOR Facility, Institute for Molecular Science, Okazaki 444-8585, Japan

<sup>3</sup>Graduate School of Science, Nagoya University, Nagoya 464-8603, Japan

<sup>4</sup>Nagoya University Synchrotron Radiation Research Center, Nagoya University, Nagoya 464-8603, Japan

<sup>5</sup>School of Physical Sciences, The Graduate University for Advanced Studies (SOKENDAI), Okazaki 444-8585, Japan

<sup>6</sup>Graduate School of Frontier Biosciences and Physics Department, Osaka University, Osaka 565-0871, Japan

<sup>7</sup>National Institute for Materials Science, Tsukuba 305-0047, Japan

Samarium monosulfide (SmS) is a prototypical valence fluctuating compound that exhibits an insulator (black) – to – metal (golden) phase transition by applying external pressure [1]. To elucidate the origin of this anomalous phase transition, the experimental investigation of the electronic structure across the phase transition has been desired.

By using the three-dimensional (3D) ARPES at UVSOR-III BL5U, we investigated the electronic structure near the Fermi level ( $E_F$ ) of  $\text{Sm}_{1-x}\text{Y}_x\text{S}$ , where the similar black-golden phase transition has been realized by the substitution of Sm by yttrium in SmS at ambient pressure [2]. For example, the color and electronic properties of  $\text{Sm}_{1-x}\text{Y}_x\text{S}$  changes from  $x = 0$ : black insulating (BI) ( $x = 0$ ), black metallic (BM) ( $x = 0.03, 0.13$ ), to golden metallic (GM) phase ( $x = 0.25, 0.32, 1$ ).

Figure 1 shows the band structure near  $E_F$  around the  $X$  point of  $\text{Sm}_{1-x}\text{Y}_x\text{S}$  obtained by the present 3D-ARPES experiment. From the comparison with our previous study [2], the electronic structure near  $E_F$  of  $\text{Sm}_{1-x}\text{Y}_x\text{S}$  consists of the  $\text{Sm}^{2+} 4f$  multiplet structures and the electron-pocket at the  $X$  point with Sm (Y)  $d$  character appearing at the metallic phase. With increasing  $x$ , the  $\text{Sm}^{2+} 4f$  multiplet structure gradually shifts to lower binding energies. Furthermore, we found that the Sm  $4f$  feature at the

black phase ( $x = 0 \sim 0.13$ ) shows sizable dispersion (dashed line), while one at the golden phase ( $x = 0.25, 0.32$ ) is non-dispersive. With respect to the electron pocket (circles), we found that there exists anomalous narrowing of the Sm  $5d$  feature at the BM phase, while the electron pocket shows a free-electron like parabolic dispersion at the GM phase. Furthermore, the high-energy shift of the electron pocket becomes intensively small from BM to GM phase. Taking account that the  $x = 1$  (YS) is a reference of the localized  $\text{Sm}^{3+}$  electron system, the present ARPES observation of the dispersive (non-dispersive) features of  $\text{Sm}^{2+} 4f$  multiplet structure as well as the narrowing (free-electron like dispersion) of Sm  $5d$  electron pocket at the BM (GM) phase might suggest the change of Sm  $4f$  electron character from itinerant to localized one across the BM-GM phase transition of  $\text{Sm}_{1-x}\text{Y}_x\text{S}$ .

[1] P. Wachter: in Handbook on the physics and chemistry of rare earths, edited by K. A. Gschneidner, Jr. *et al.*, (North-Holland, Amsterdam, 1994), Vol. 19, p. 383.

[2] K. Imura *et al.*, J. Korean Phys. Soc. **62** (2013) 2028.

[3] V. N. Antonov *et al.*, Phys. Rev. B **58** (1998) 6807.

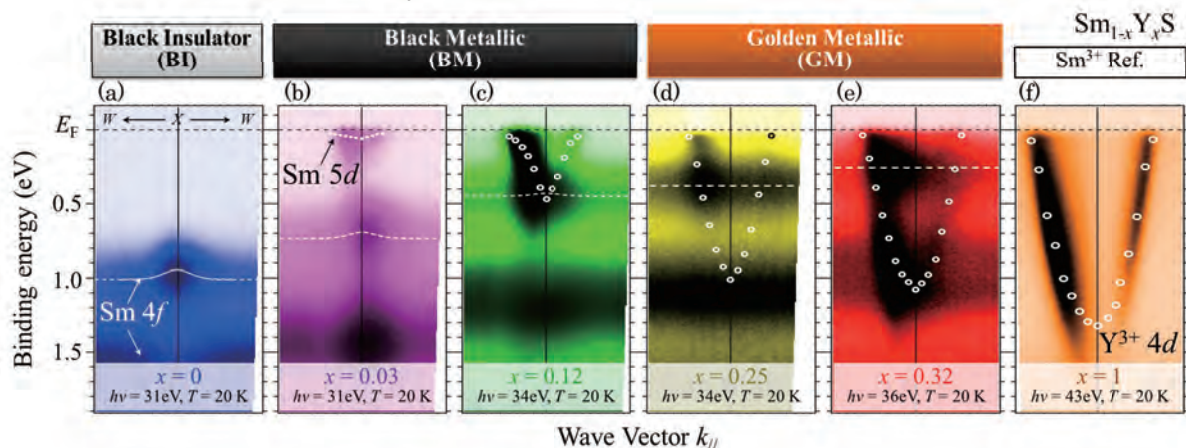


Fig. 1. Band structure of the  $\text{Sm}_{1-x}\text{Y}_x\text{S}$  ( $x = 0$  (a), 0.03 (b), 0.13 (c), 0.25 (d), 0.32 (e), and 1 (f)). Dashed lines (open circles) are guide for Sm  $4f$  (Sm  $5d$  (Y  $4d$ )) features, respectively.

BL5U

## Angle-Resolved Photoemission Study on LuPtSb

E. Tsuiki<sup>1</sup>, M. Kaneko<sup>1</sup>, T. Hosokawa<sup>1</sup>, T. Ito<sup>1,2</sup>, T. Hajiri<sup>1,3</sup>, S. Kimura<sup>3,4</sup>, M. Matsunami<sup>3,5</sup>, K. Imura<sup>6</sup> and S. Suzuki<sup>7</sup>

<sup>1</sup>Graduate School of Engineering, Nagoya University, Nagoya 464-8603, Japan

<sup>2</sup>Nagoya University Synchrotron Radiation Research Center, Nagoya University, Nagoya 464-8603, Japan

<sup>3</sup>UVSOR Facility, Institute for Molecular Science, Okazaki 444-8585, Japan

<sup>4</sup>Graduate School of Frontier Biosciences and Physics Department, Osaka University, Osaka 565-0871, Japan

<sup>5</sup>School of Physical Sciences, The Graduate University for Advanced Studies (SOKENDAI), Okazaki 444-8585, Japan

<sup>6</sup>Graduate School of Science, Nagoya University, Nagoya 464-8603, Japan

<sup>7</sup>National Institute for Materials Science, Tsukuba 305-0047, Japan

Several years ago, new kind of functional materials that are neither the metal nor the insulator, so called Topological Insulator, were discovered. In topological insulators, the bulk properties are characterized as semimetal or insulating, while the surface ones, as unique metal. In the surface metallic state, the band shows linear (Dirac cone) dispersion between the bulk, which in fact observed by angle-resolved photoemission spectroscopy (ARPES) on TlBiSe<sub>2</sub> [1].

Semi-metallic half-Heusler compound XYZ (X,Y: Rare earth or transition element, Z: pnictogen) with the lattice distortion have been expected to be a topological insulator [2]. By changing combination of X, Y, and Z atoms, the ground state changes from topologically trivial (semiconducting) to non-trivial (semi-metallic) as the characteristic energy difference between the  $\Gamma_6$  and  $\Gamma_8$  bands changes from negative to positive. Furthermore, it is predicted that there is a possibility of controlling functionalities (superconductivity, magnetism, and abnormal carrier) in addition to the topologically insulating states. On the other hand, there are few experimental evidences of the existence of the topologically trivial to non-trivial border at the electronic structure of half-Heusler ternary compounds so far.

In this study, we have performed angle-resolved photoemission spectroscopy (ARPES) on LuPtSb, which has been expected to be located on the non-trivial border [2, 3], to clarify the intrinsic electronic structure of this system as the starting point.

Figure 1(b) shows ARPES spectra along cut1 passing through the  $\Gamma$  point in the fcc Brillouin zone (BZ) (Fig. 1(a)) of LuPtSb obtained by utilizing  $h\nu = 61$  eV photons. To show the dispersive features clear, the second-derivative ARPES intensity plot of Fig. 1(b) is shown in Fig. 2 (a). We found that the highly-dispersive features around the  $\Gamma$  point seems to be similar between the experiment and the calculation (Fig. 2(b)).

On the other hand, we found two types of Fermi surfaces (FSs) around the BZ center and boundary, respectively. The former is formed by the small electron-pocket whose bottom merges with the hole-like dispersion around 100 meV, while the latter

by the large electron-pocket appearing symmetrically with respect to the  $\Gamma$  point. Thus the experimental electronic structure near  $E_F$  of the LuPtSb shows strong contrast to the calculation where the zero-gap states at  $E_F$  form a point-like FS at the BZ center. To elucidate the effect of the FS formation at LuPtSb to the systematic change of the electronic structure of half-Heusler ternary compounds, systematic ARPES study on the trivial border system, YPtSb etc., is intended.

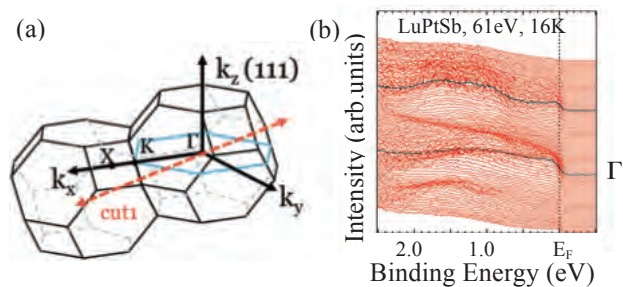


Fig. 1. (a) fcc Brillouin zone of LuPtSb. (b) ARPES spectra along cut1 from Fig.1(a) obtained by using  $h\nu = 61$  eV photons.

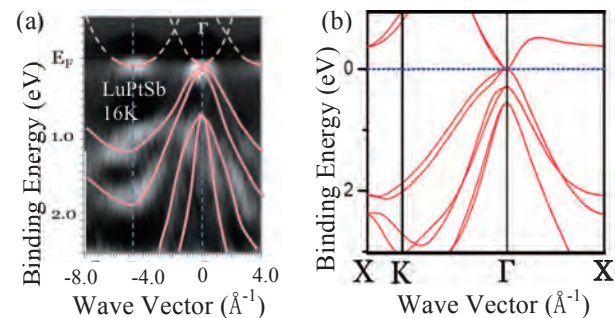


Fig. 2. (a) Second-derivative ARPES image of Fig. 1. Thick lines are guide for eyes. (b) Band structure calculation of LuPtSb along the  $\Gamma$  KX line.

[1] T. Sato *et al.*, Phys. Rev. Lett. **105** (2010) 136802.

[2] S. Chadov *et al.*, Nature Mat. **9** (2010) 541.

[3] W. Al-Sawai *et al.*, Phys. Rev.B **82** (2010) 125208.

BL5U

## Photoemission Study of $\text{Mg}_x\text{Zn}_{1-x}\text{O}$ Synthesized under High Pressure

K. Takahama<sup>1</sup>, R. Eguchi<sup>2</sup>, D. Shimada<sup>3</sup>, M. Kato<sup>1</sup>, K. Niwa<sup>2,3</sup>, K. Kusaba<sup>2,3</sup>, M. Hasegawa<sup>2,3</sup> and K. Soda<sup>1,3</sup>

<sup>1</sup>Department of Quantum Engineering, Graduate School of Engineering, Nagoya University, Nagoya 464-8603, Japan

<sup>2</sup>Department of Physical Science and Engineering, School of Engineering, Nagoya University, Nagoya 464-8603, Japan

<sup>3</sup>Department of Crystalline Materials Science, Graduate School of Engineering, Nagoya University, Nagoya 464-8603, Japan

Wide band-gap semiconductor ZnO and its related solid solutions have received much interest for a variety of applications such as electronic and optoelectronic devices, catalysts, gas sensors, and transparent conductive films. Under high pressures, ZnO crystalizes in NaCl structure (B1) with a band gap  $E_G$  of 2.45 eV and can form solid solutions with B1-type MgO of  $E_G \sim 7.7$  eV in wide concentration range. Hence it is expected from band structure calculations [1] that the band gap of  $\text{Mg}_x\text{Zn}_{1-x}\text{O}$  may increase with  $x$ . Thus we have investigated the electronic band structure, in particular band gap, of n-type semiconductor  $\text{Mg}_x\text{Zn}_{1-x}\text{O}$  by use of photoelectron spectroscopy.

Photoelectron measurement was performed at room temperature. Specimens of B1-type  $\text{Mg}_x\text{Zn}_{1-x}\text{O}$  were synthesized at high temperatures of 1173 K under high pressure of 6.5 GPa, and their clean surfaces for the photoelectron measurement were prepared by scraping them with a diamond file. The origin of the binding energy  $E_B$  was set to the Fermi energy  $E_F$  of an evaporated film on the sample holder.

Figure 1 shows valence-band spectra of  $\text{Mg}_x\text{Zn}_{1-x}\text{O}$  recorded with weak photon intensity to prevent from the charging-up effect as possible. Spectral intensities are normalized with the integrated intensity up to  $E_B = 20$  eV. Densities of states (DOS) for B1-type  $\text{Mg}_x\text{Zn}_{1-x}\text{O}$  are calculated by a full-potential linearized augmented plane wave (FLAPW) method with WIEN2k code [2] and GGA-PBE approximation [3] for the exchange-correlation energy and they are also presented for comparison in the figure, where the DOS's are plotted as a function of energy relative to the conduction minimum (CVM) indicated by a broken line and are shifted by 5 eV towards the high binding energy side (in the lower abscissa), compared to the experimental spectra.

Overall spectral features agree fairly well with the calculated DOS except for a band at  $E_B \sim 15$  eV, the origin of which is unknown at present. Taking account of the n-type semiconductor, the band gap can be estimated from the binding energy of the valence band onset, which is indicated by arrows in Fig.1. Observed band gaps are about 2~3 times larger than calculated ones, as known as the underestimation of the band gap by the band structure calculation [4].

As is already reported [1], the calculated band gap increases gradually with the Mg content  $x$ . For cubic  $\text{Mg}_x\text{Zn}_{1-x}\text{O}$  epitaxial films ( $x > 0.6$ ), it has been reported that  $E_G > 6$  eV [5]. However, the present experimental band gap seems almost unchanged or slightly decreased as  $x$  is increased. At present this discrepancy has not been clarified yet; it might arise from the Fermi level pinning due to surface defect states such as those of oxygen deficiency. Charging-up effects might smear out fine structures and the band onset. Further study is intended on the dependences on specimens and the content  $x$ .

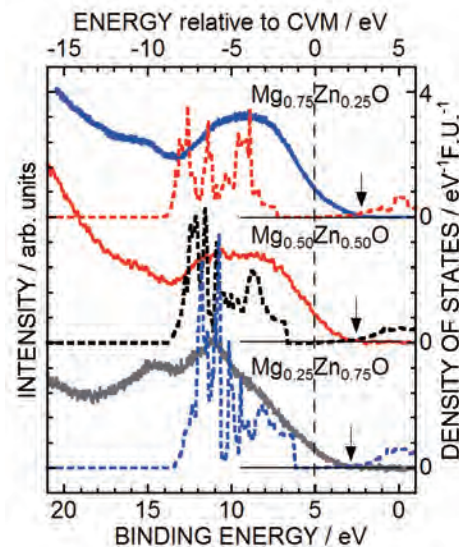


Fig. 1. Photoelectron spectra and calculated densities of states of  $\text{Mg}_x\text{Zn}_{1-x}\text{O}$ .

- [1] F. Z. Aoumeur-Benkabou *et al.*, Model. Num. Sim. Mater. Sci. **2** (2012) 60.
- [2] P. Blach *et al.*, Comput. Phys. Commun. **59** (1990) 399-415.
- [3] J. P. Perdew *et al.*, Phys. Rev. Lett. **77** (1996) 3865.
- [4] D. Fritsch *et al.*, Appl. Phys. Lett. **88** (2006) 134104
- [5] S. Choopun *et al.*, Appl. Phys. Lett. **80** (2002) 1529.

BL5U

## Resonance Photoemission Study on Electronic Structure of $\text{Fe}_{2-x}\text{VAl}_{1+x}$

S. Osawa<sup>1</sup>, Y. Yamada<sup>2</sup>, H. Miyazaki<sup>3</sup>, M. Kato<sup>1</sup>, Y. Nishino<sup>2</sup> and K. Soda<sup>1</sup>

<sup>1</sup>Department of Quantum Engineering, Graduate School of Engineering, Nagoya University, Nagoya 464-8603, Japan

<sup>2</sup>Department of Frontier Materials, Graduate School of Engineering, Nagoya Institute of Technology, Nagoya 466-8555, Japan

<sup>3</sup>Center for Fostering Young and Innovative Researchers, Nagoya Institute of Technology, Nagoya 466-8555, Japan

Heusler-type intermetallic compound  $\text{Fe}_2\text{VAl}$  and related alloys have attracted much attention as thermoelectric materials with a pseudogap around the Fermi level  $E_F$  in its electronic structure [1]. In  $\text{Fe}_{2-x}\text{VAl}_{1+x}$ , both the p-type and n-type thermoelectric powers are enhanced on the off-stoichiometric change in the Fe/Al ratio, while the semiconductor-like temperature dependence of the electrical conductivity is observed for  $x > 0.08$ ; it can be explained by thermal excitation between the pseudogap like semiconductor and the weak localization caused by the random occupation of the excess Al at the Fe sub-lattice for  $x > 0.12$  [2]. Analysis of the core-level spectra suggests that the V3d states may appear just below  $E_F$ . Thus we have performed the Fe3p-3d resonance photoemission study to clarify the V3d partial density of states (DOS) by suppressing the Fe3d states on the anti-resonance as well as the Fe3d partial DOS by the on-resonance enhancement.

The photoemission measurement was carried out at 7 K with the energy resolution of  $\sim 70$  meV in an angle integrated mode. Polycrystalline specimens of  $\text{Fe}_{2-x}\text{VAl}_{1+x}$  were *in situ* fractured with a knife edge to prepare clean surfaces for the measurement. Origin of the binding energy  $E_B$  is set to  $E_F$  by measuring a Fermi edge of a gold film evaporated onto the sample holder.

Figure 1 shows typical on-resonance (recorded at the excitation photon energy  $h\nu$  of 55 eV) and anti-resonance (at  $h\nu = 52$  eV) valence-band spectra for  $x = 0, 0.08$  and  $0.18$ . Here, the spectra are subtracted backgrounds due to the secondary electrons from by an iteration method [3] and normalized with the intensity of the V3d-derived band at  $E_B = 1.5$  eV, although the hybridized Fe3d states contribute to the band at 1.5 eV in the on-resonance spectra.

As seen in Fig. 1, the Fe3d-derived bands are located around  $E_B = 0.7$  and 3 eV; they are enhanced at  $h\nu = 55$  eV, compared to the V3d-derived band at 1.5 eV, due to the Fe3p-3d resonance. The band at  $E_B \sim 6$  eV in the anti-resonance spectra is attributed to the s-like hybridized states; it is shifted to the high binding energy side and enhanced in the on-resonance spectra, which is ascribed to the Auger-like emission near the 3p-3d resonance. Small shift of the main 3d valence-band as a whole is recognized to the low binding energy side with  $x$  increased. This is due to

the decrease in the valence electron counts by substitution of the excess Al for Fe, as expected in a rigid band model [1]. On the other hand, the anti-resonance spectra show that the spectral intensity near  $E_F$  is increased with  $x$ , while the intensity at  $E_F$ , in particular for  $x = 0.08$  and  $0.18$ , does not change so much for the on-resonance spectra. Thus the V3d states grow just below  $E_F$  with increasing  $x$  ( $x > 0.08$ ), as suggested [2], although the surface states may affect the spectra [4]. The Fe3d-derived states are also increased near  $E_F$  for  $x = 0.08$  and  $0.18$  in comparison with  $\text{Fe}_2\text{VAl}$ .

These states near  $E_F$  act as the impurity states at the edges of the semimetallic conduction and valence bands, leading to the weak localization and the mobility gap. This also suggests the importance of the relaxation time factor for thermoelectric properties as well as the factors of DOS and its energy derivative.

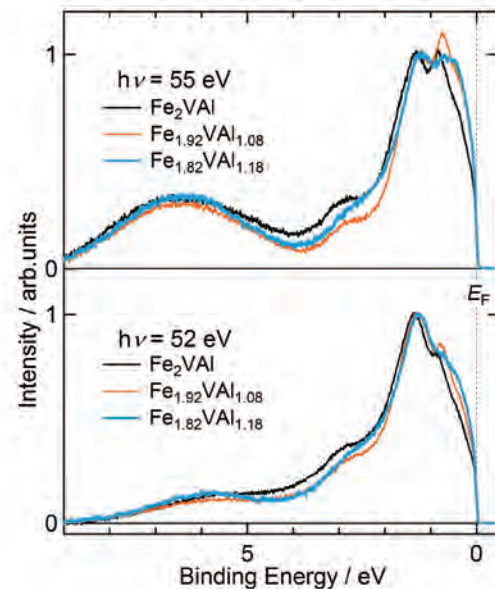


Fig. 1. Valence-band spectra of  $\text{Fe}_{2-x}\text{VAl}_{1+x}$ .

[1] Y. Nishino, IOP Conf. Series: Mater. Sci. Eng. **18** (2011) 142001.

[2] K. Soda *et al.*, J. Phys. Soc. Jpn. *in press*.

[3] K. Soda *et al.*, J. Phys. Soc. Jpn. **60** (1991) 3059.

[4] H. Miyazaki *et al.*, J. Vac. Sci. Technol. A **24** (2006) 1464.

BL5B

## Reflectance Measurement of Fluoride Output-Coupler for Cavity High-Harmonic Generation in VUV

K. Wakui, K. Hayasaka and T. Ido

*National Institute of Information and Communications Technology, Tokyo 184-8795, Japan*

Intracavity high-harmonic generation of near infrared femtosecond (fs) frequency combs using a passive enhancement cavity has extended accessible wavelength of frequency combs, realizing precision spectroscopy in the extreme ultraviolet [1]. Lower harmonics at 150-200 nm vacuum ultraviolet (VUV) also attract interests because conventional optics are barely available using fluoride material. In addition, each comb components are well separated thanks to high repetition rate, and rather small phase shift from the nonlinear media maintains the regular comb structures in this wavelength. Therefore its application to a precision spectroscopy at the VUV wavelengths is anticipated.

Among various important atomic transitions, the time and frequency community has been interested in the use of  $^1S_0 - ^1P_1$  transitions in alkaline-earth-like ions for state detection in the optical clock based on the proposal by Dehmelt in 1982 [2]. Moreover, a clock transition in a single thorium nucleus has been intensively studied for realizing hyper-accurate frequency standard [3]. However, they all exist in VUV region and the direct excitation has never been realized because of the difficulty in development of continuous-wave (CW) coherent laser source in that wavelength range. Alternatively, the single frequency-comb component of the high-rep VUV combs may be able to act as a “quasi-CW” laser and thus to work as a state detection laser. In the case of such ions including  $Al^+$ , a simple estimation indicates that single-mode VUV power in the order of 10 pW might yield fluorescent photons sufficient for the state detection. The single comb components of the high-rep VUV combs may supply this level of average intensity. This approach also opens a way to simultaneous detection of multiple ions, which may overcome limited stability of the single-ion clocks. Indium ion ( $^{115}In^+$ ) provides an ideal test bed for this approach [4], where the 159 nm radiation generated as the 5th harmonic of a Ti:S laser can excite the  $^1S_0 - ^1P_1$  transition. In our intracavity HHG setup with the repetition rate of 110 MHz, a total average intensity in the order of 10  $\mu W$  may provide sufficient for  $In^+$  detection, whereas it has been limited to 1.5  $\mu W$  in our previous report [5].

The output coupling of high harmonics from the cavity is the key to scale up the yield of intracavity HHG. Several methods were previously demonstrated using e.g. bulk sapphire windows as Brewster plates [6, 7], a diffraction grating carved onto a NIR mirror [8], and on an anti-reflection-coated grazing

incidence plate [9]. Here, we design and demonstrate a new type of VUV output-coupler (VUV-OC). The VUV-OC consists of a  $SiO_2$  substrate of  $\sim 100$   $\mu m$  thickness with a fluoride-multilayer coating on one of its surfaces. The VUV-OC's reflectance is designed to be  $>80\%$  at 153-163 nm and  $>90\%$  at 159 nm for p-polarized VUV light, while it works as a Brewster plate at the incident angle of  $\sim 55$  degree, that corresponds to a Brewster angle to  $SiO_2$  at 795 nm. We confirmed the reflectance in VUV using the beamline facility (BL5B) in UVSOR. As shown in Fig. 1, the reflectance of  $\sim 90\%$  was measured at 159 nm as designed. We also demonstrate an efficient output-coupling method using the VUV-OC for our HHG experiment. The final yield of the HHG currently amounts to 4.2  $\mu W$  at 159 nm, which is almost three times larger than previous work in spite of  $\sim 20\%$  reduction of the NIR inside the cavity.

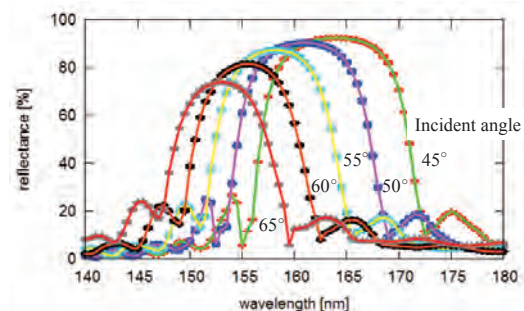


Fig. 1. Reflectance of the fluoride output coupler.

- [1] A. Cingös *et al.*, *Nature* **482** (2012) 68.
- [2] H. Dehmelt, *IEEE Trans. Instrum. Meas.* **31** (1982) **IM-31**.
- [3] E. Peik and Ch. Tamm, *Europhys. Lett.* **61** (2003) 181.
- [4] K. Hayasaka, *Appl. Phys. B* **107** (2012) 965.
- [5] K. Wakui, K. Hayasaka and T. Ido, *Proc. SPIE* **8132**, Time and Frequency Metrology III, 813204 (2011).
- [6] R. J. Jones, K. D. Moll, M. J. Thorpe and J. Ye, *Phys. Rev. Lett.* **94** (2005) 193201.
- [7] Ch. Gohle *et al.*, *Nature* **436** (2005) 234.
- [8] D. Yost, T. Schibli and J. Ye, *Opt. Lett.* **33** (2008) 1099.
- [9] Y. Y. Yang *et al.*, *Opt. Express* **19** (2011) 1954.

BL5B

## Reflectance of Hypothetical Meteors in EUV Spectral Range

T. Hamaguchi, M. Kuwabara, K. Isashiki, K. Uji and I. Yoshikawa  
*Graduate School of Science, the University of Tokyo, Hongo 113-8654, Japan*

We have measured the surface reflectivities in the EUV spectral ranges, of two examples (NWA 4423, NWA 645) which are hypothetical meteors. We have selected (3, 5) among the combinations of (G,M) and always employed Al/Mg/Al filter to avoid the higher-order spectral contamination. Each result is shown in Fig. (Fig. 2 shows the reflectivity of NWA 4423, Fig. 3 is NWA 645). Please note that the statistical error of NWA 4423 reflectivity measurement is over-plotted, but it is so small (approximately 1/1000) that you might not identify it.

These measurements will be useful, when the albedo of solid planets needs to be studied.

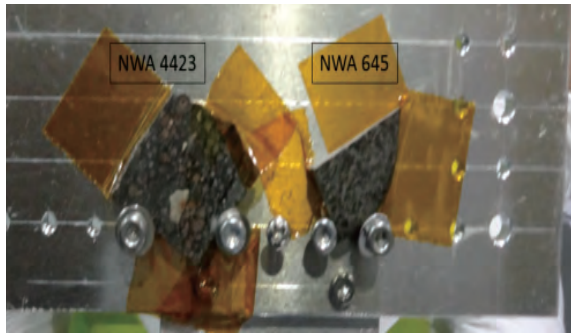


Fig. 1. Two examples of hypothetical meteors (left) NWA 4423, (right) NWA 645.

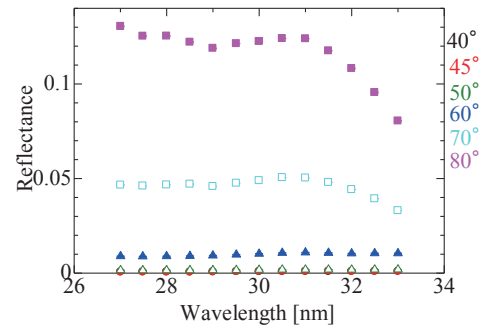


Fig. 2. NWA 4423 reflectivity.

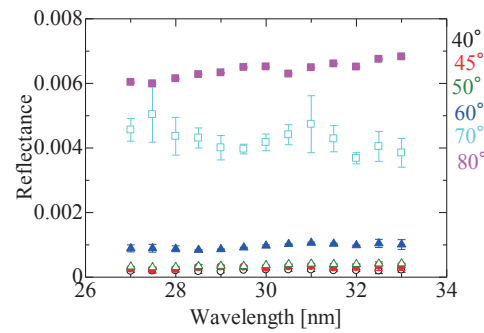


Fig. 3. NWA 645 reflectivity.

BL6B

## Far-Infrared Reflective Study of Alkali Niobate Ceramics

T. Yamazaki, M. Kato, K. Tsuchida and K. Kakimoto

Graduate School of Engineering, Nagoya Institute of Technology, Nagoya 466-8555, Japan

Alkali niobate ceramics are one of the promising candidates for lead-free piezoelectric materials. Especially,  $\text{Li}(\text{Na},\text{K})\text{NbO}_3$  solid solution shows excellent piezoelectric properties and high Curie temperature. In our previous work, we demonstrated that the small ionic diameter Li substitution induces monoclinic  $Pm$  phase using synchrotron X-ray, EXASF and FT-IR analyses. It is expected that  $Pm$  phase involves piezoelectric properties. The present work reports the spectroscopic characterization of  $Pm$  phase using infrared (IR) technique.

The  $\text{Li}_{0.02}(\text{Na}_{0.5}\text{K}_{0.5})_{0.98}\text{NbO}_3$  (LNKN02) ceramics were obtained by conventional solid state reaction. The surface of the LNKN sample was mirror polished for IR reflectivity measurement. The spectra were corrected by using Michelson interferometer (Bruker, IFS66v). The measured reflectivity data was fitted using the equation (1) and (2), as mentioned below.

$$R = \left[ \frac{\sqrt{\varepsilon(\omega)} - 1}{\sqrt{\varepsilon(\omega)} + 1} \right]^2 \quad (1)$$

$$\varepsilon(\omega) = \varepsilon_\infty + \sum_n \frac{\omega_{np}^2}{\omega_{no}^2 - \omega^2 - n\gamma_n\omega} \quad (2)$$

Where,  $\varepsilon_\infty$  is the high-frequency dielectric constant,  $\omega_p$  and  $\omega_o$  are the plasma and longitudinal frequencies, and  $\gamma$  is the damping constant.

The reflectivity spectra of LNKN02 in the temperature range from 10 to 290 K are shown in Fig.1. Remarkable difference in spectra is found below 30 K. Figure 2 shows the imaginary part of complex dielectric constant, which was calculated by fitting result using equations (1) and (2). Five peaks were assumed around  $600 \text{ cm}^{-1}$  using  $(\text{Na}_{0.5}\text{K}_{0.5})\text{NbO}_3$  (NKN) data[1] and group factor analysis. Three peaks are related to  $Bmm2$  phase which represents NKN and two peaks are related to  $Pm$  phase. The  $Pm$  ratio calculated by fitting peaks area was about 26 % at 290 K. Figure 3 shows the calculated  $Pm$  ratio for LNKN02 ceramics at various temperatures. The  $Pm$  ratio is found to independent of temperature with the decrease in temperature from 290 to 190 K. At 170 K,  $Pm$  ratio increased suddenly and further temperature induces the decrease in  $Pm$  ratio gradually. Finally, the  $Pm$  ratio decreases about 10 % at 30 K. It can therefore be suggested that LNKN02 ceramics indicate two phase transitions from 290 to 10 K which is different from those of the pure NKN phase.

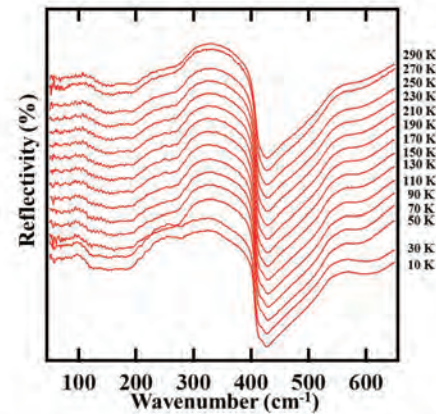


Fig. 1. The reflectivity spectra of LNKN02.

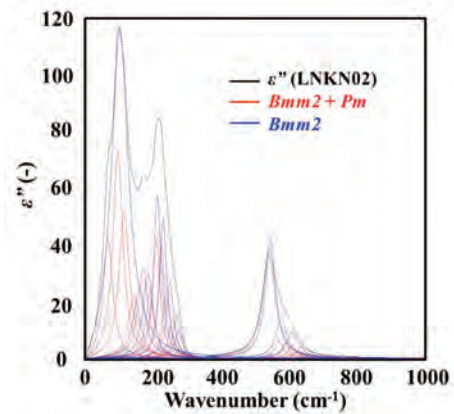


Fig. 2. The imaginary part of complex dielectric constant for LNKN02 at 290 K

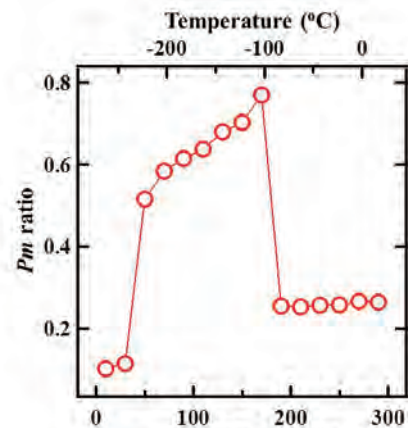


Fig. 3. Temperature dependence of the  $Pm$  ratio for LNKN02 ceramics.

[1] M. D. Fontana *et al.*, Phys. Stat. Sol. (b) **103** (1981) 211.

BL6B

## Final State of Ultrashallow Thermal Donors Formed in Carbon- and Hydrogen-Doped Czochralski Silicon Crystals

A. Hara and T. Awano

*Department of Electronic Engineering, Tohoku Gakuin University, Tagajo 985-8537, Japan*

In the past, we have reported on ultrashallow thermal donors (USTDs) formed in carbon- and hydrogen-doped Czochralski silicon (CZ Si) crystals after annealing at 480°C [1,2]. In this study, we evaluated the final state of USTDs.

Carbon-doped CZ Si samples were doped with hydrogen by annealing them in wet oxygen at 1300°C for 60 min. The samples were then cooled to room temperature by rapidly exposing them to air. For carbon doping, the Si melt for preparing the ingot was doped with carbon powder during CZ Si crystal growth. Transmission spectra were obtained using the far-IR spectrometer of the BL6B beamline at the liquid-He temperature using a flowing cryostat.

Figure 1(a) shows the spectra of USTDs and shallow thermal donors (STD(H)s) after annealing at 480°C for various durations. It has been reported that STD(H)s are hydrogen-like donors and are generated in hydrogen-doped CZ Si crystals at approximately 450°C [3]. USTD-A and USTD-B are generated in an initial stage of annealing at 480°C and eliminated after long-term annealing at the same temperature. Finally, the intensities of only two peaks, namely, USTD-C and USTD-D, are remarkable at 480°C-65h. Figure 1(b) shows USTDs formed after annealing for 40 hours at 450°C, 480°C, and 510°C, respectively. The spectrum of the USTDs at 450°C-40h is nearly the same as that at 480°C-20h in Fig. 1(a). Moreover, the spectrum at 510°C-40h is nearly the same as that at 480°C-65h in Fig. 1(a), and only two peaks, USTD-C and USTD-D, are remarkable. Figure 1(c) shows the spectra of the USTDs at 480°C-40h followed by additional annealing at each temperature higher than 480°C for 15 min. The spectrum with additional annealing at 550°C is nearly the same as that at 480°C-52h and the spectrum at 600°C is nearly the same as that at 480°C-65h. Also, in this case, only two peaks, namely, USTD-C and USTD-D, are remarkable, and their intensity decreases with annealing above 620°C.

As mentioned in our previous report, our model for generating USTDs comprises the following: in the first stage, STD(H)s are generated at high formation speeds and, in the second stage, carbon modulates the electronic structure of STD(H)s. The fact that similar spectra are obtained with short-duration annealing with increasing annealing temperature indicates that thermally activated processes are concerned with the generation of USTDs. According to our model, carbon acted as a modulator and had to migrate to STD(H)s. It is a thermally activated process.

USTD-A and USTD-B are generated in the initial stage of annealing at 480°C and eliminated after long-term annealing at the same temperature. Thus, these are not the final states of USTDs, but intermediate products. The USTD-C and USTD-D are believed to be the final states of USTDs, because all experimental results show the survival of only these two peaks. The final form of these two USTDs is consistent with the generation of two STD(H)s in the initial stage. These results support our proposed mechanism of formation.

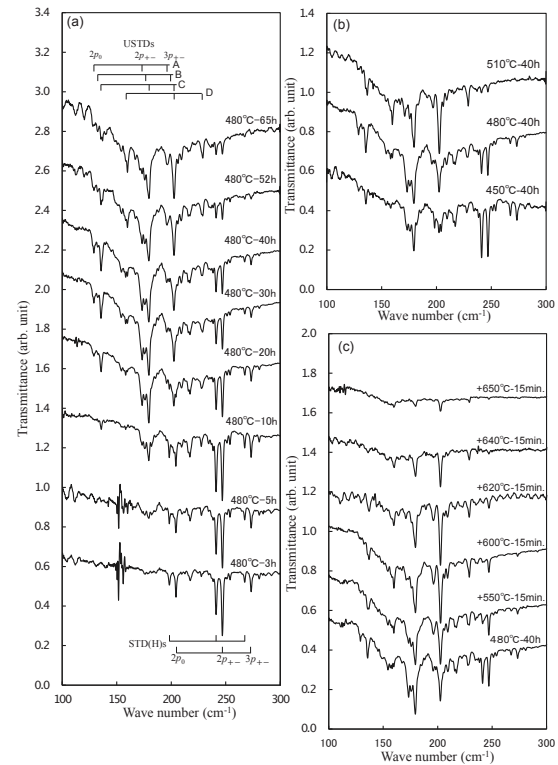


Fig. 1. (a) Annealing behavior of USTDs at 480°C; (b) temperature dependence of USTDs with annealing for 40 h; (c) annealing behavior of USTDs after 40 h followed by additional annealing for 15 min at a higher temperature than 480°C.

[1] A. Hara, T. Awano, Y. Ohno and I. Yonenaga, *Jpn. J. Appl. Phys.* **49** (2010) 050203.

[2] A. Hara and T. Awano, *UVSOR Activity Report* **40** (2013) 103.

[3] R. C. Newman, J. H. Tucker, N. G. Semaltianos, E. C. Lightowers, T. Gregorkiewicz, I. S. Zevenbergen and C. A. J. Ammerlaan, *Phys. Rev. B* **54** (1996) R6803.

BL6B

## Electronic States on Solids Probed by a FIR-THz Light Using the Synchrotron Radiation

A. Irizawa

*The Institute of Science and Industrial Research, Osaka University, Ibaraki 567-0047, Japan*

Optical study is one of the most powerful techniques for investigating electronic states on solids. There can be obtained the great deal of information about the electronic states, a band structure, a symmetry of crystal structure, and a dielectric response. In view of experimental affinity, the optical study is extremely compatible with multiple conditions such as low temperature, high magnetic field, and high pressure. The observation of electronic states can be concluded with only optical operations. In the case of strongly correlated electron systems, it is well known that the temperature is one of the decisive factors for the electronic state. The considerable types of phase transition are induced by the change of the temperature. Particularly, the multiferroic compounds can be controlled of its physical properties mutually by the external fields such as magnetic, electronic, and elastic ones. The other particular condition, the pressure will directly affect the electron-electron interactions through the change of lattice constants. The beamline 6B in UVSOR is adjusted for the investigations at low temperature and high pressure in the extremely low-energy region of FIR-THz. There equips two type interferometers of both Michelson and Martin-Puplett type. In this report, we have performed the optical transmittance measurements in the longest wavelength region for several compounds having peculiar absorption bands there.

The selected experimental components are the Michelson type interferometer and the Si-bolometer detector with the liquid-He flow type cryostat for controlling the temperature from 300 K down to 13 K. The transmittance was obtained from the ratio of optical transmission spectra between the sample and polypropylene as a matrix for samples. The concentration of samples is around 5%wt for the matrix. They were installed on the sample holder and the transmittance was measured through the tapered hole of 4mm in diameter.

The transmittances are obtained in the energy range between 40 and 600  $\text{cm}^{-1}$  as shown in Fig. 1. Here we can confirm the red shift of absorption bands with increasing temperature. The transmittances are nearly 1 at lower energies and go down to zero in higher energies. It means that both CuO and  $\text{Cu}_2\text{O}$  are insulating and the gaps are around there. Small amount of CuO can be recognized in  $\text{Cu}_2\text{O}$ , but the samples are almost single phases. We notice that the shift of absorption bands around 150  $\text{cm}^{-1}$  between CuO and  $\text{Cu}_2\text{O}$ . This must be due to the difference of

bonds between Cu and O and is originated in the difference of valence. At the same time, experiments in THz region using FEL in Osaka University are in execution. The information obtained using FT-IR is useful for the high power light source experiments.

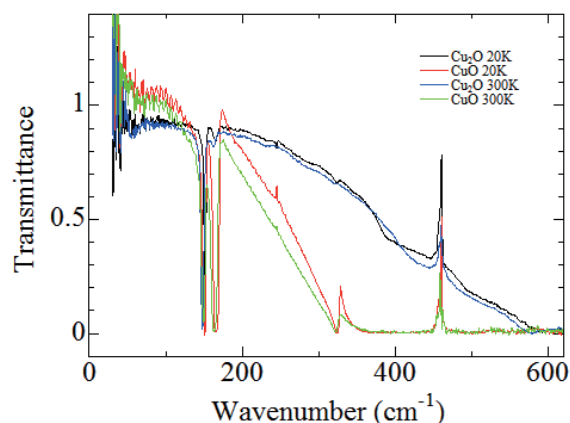


Fig. 1. Temperature change of transmittance of CuO and  $\text{Cu}_2\text{O}$  at the FIR-THz region.

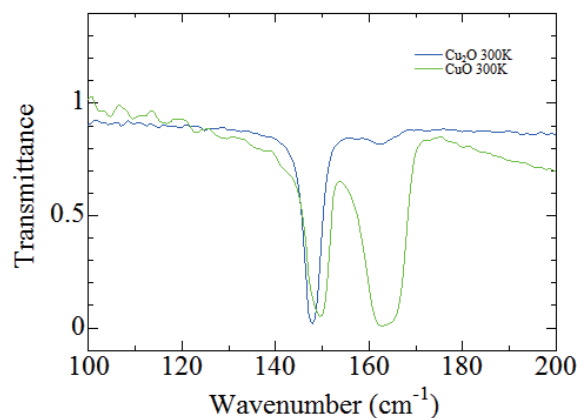


Fig. 2. Expansion near the absorption bands at 300 K.

BL6B

## Macroscopic Randomness of Carrier Density in $\text{Sm}_{0.83}\text{Y}_{0.17}\text{S}$

S. Kimura<sup>1</sup>, K. Imura<sup>2</sup> and N. K. Sato<sup>2</sup><sup>1</sup> Graduate School of Frontier Biosciences and Department of Physics, Osaka University, Suita 565-0871, Japan<sup>2</sup> Department of Physics, Nagoya University, Nagoya 464-8603, Japan

Inhomogeneity or randomness of samples is important to investigate the origin of the physical properties of materials because local distortion becomes a trigger of a phase transition [1]. The origin of the insulator-to-metal transition, namely black-golden phase transition (BG transition), of  $\text{SmS}$  by applying an external pressure is under debate [2], one of candidates of such phenomena, i.e., the BG transition originates from inhomogeneity and/or spatial distribution of distortion. However, it is difficult to obtain the information of local electronic structures of samples. In the study, to obtain the spatial distribution of carrier density in the vicinity of the BG transition, the spatial distribution of the infrared reflectivity spectrum of  $\text{Sm}_{0.87}\text{Y}_{0.17}\text{S}$ , which is located near the BG transition at ambient pressure [3].

The experiment was performed at the infrared imaging end station of BL6B using a 16-channel linear array MCT detector [4]. The spatial resolution and the sampling points were set to be about  $6\ \mu\text{m}$  and  $64 \times 64$  points, respectively. The total measurement time was about 40 min.

Figure 1a is a visible image of  $\text{Sm}_{0.87}\text{Y}_{0.17}\text{S}$ . Almost all the area is black (black phase), but tiny areas are changed to gold (golden phase), which indicates the coexistence of both phases. Reflectivity spectra taken at the four different points on the sample are shown in Fig. 1b. The spectra are much different from one another, two of four spectra have a bending part indicated by arrows, which wavenumber corresponds to the plasma edge of free carriers ( $\omega_p$ ).  $\omega_p^2$  is proportional to the carrier density. Other two spectra have the plasma edge above the accessible wavenumber of  $6000\ \text{cm}^{-1}$ , but the intensity at around  $6000\ \text{cm}^{-1}$  corresponds to the carrier density owing to the spectral shape of a free carrier Drude formula.

The images at several wavenumbers are shown in Figs. 1c1–1c4. The image at the wavenumber of  $800\ \text{cm}^{-1}$  shown in Fig. 1c1 is almost monochrome except for low reflectivity at cracks on the sample. This implies that the plasma edge of the monochrome area is located at the wavenumber above  $800\ \text{cm}^{-1}$ . At higher wavenumbers, the image becomes more inhomogeneous. The image at  $3000\ \text{cm}^{-1}$  in Fig. 1c3 is the most inhomogeneous owing to the distribution of the wavenumber of the plasma edge around  $3000\ \text{cm}^{-1}$ . In addition, the difference of the golden area from the black area in the visible image of Fig. 1a is only observed in the image at  $5700\ \text{cm}^{-1}$  in Fig. 1c4.

In comparison with the visible image in Fig. 1a, the

reflectivity of the golden area at  $3000\ \text{cm}^{-1}$  in Fig. 1c3 is similar to the black area but the part at the right lower side has a stripe pattern despite the constant black phase in the visible image. This suggests that the inhomogeneity of carrier density appears in the black phase.

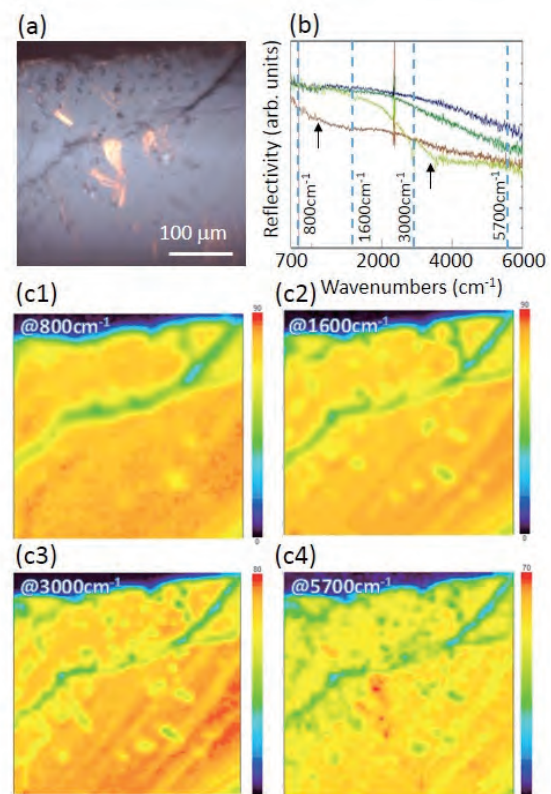


Fig. 1. (a) Visible image of a measured sample of  $\text{Sm}_{0.83}\text{Y}_{0.17}\text{S}$ . (b) Four spectra at different positions on the sample. Reflectivity intensities at  $800\ \text{cm}^{-1}$  (c1),  $1600\ \text{cm}^{-1}$  (c2),  $3000\ \text{cm}^{-1}$  (c3), and  $5700\ \text{cm}^{-1}$  (c4).

[1] e.g. L. Zhang, C. Israel, A. Biswas, R. L. Greene and A. de Lozanne, *Science* **298** (2002) 805.

[2] P. Wachter, *In Handbook on the Physics and Chemistry of Rare Earth* (North-Holland, 1994) **19** (1994) 383.

[3] K. Imura, T. Hajiri, M. Matsunami, S. Kimura, M. Kaneko, T. Ito, Y. Nishi, N. K. Sato and H. S. Suzuki, *J. Korean Phys. Soc.* **62** (2013) 2028.

[4] S. Kimura, T. Katsumata and J. Koshobu, *UVSOR Activity Report* **40** (2013) 45.

BL7U

## Observation of the Phonon Dispersion in Single-Crystalline Graphite by Angle-Resolved Photoelectron Spectroscopy

 S. Tanaka<sup>1</sup>, M. Matsunami<sup>2,3</sup> and S. Kimura<sup>2,3,4</sup>
<sup>1</sup>The institute of Scientific and Industrial Research, Osaka University, Ibaraki 567-0047, Japan.

<sup>2</sup>UVSOR Facility, Institute for Molecular Science, Okazaki 444-8585, Japan.

<sup>3</sup>School of Physical Sciences, The Graduate University for Advanced Studies (SOKENDAI), Okazaki 444-8585, Japan.

<sup>4</sup>Graduate School of Frontier Biosciences, and Department of Physics, Osaka University, Suita 565-0871, Japan.

Recently, we demonstrated an experimental method using the angle resolved photoelectron spectroscopy in which the elemental process of EPC (electron-phonon coupling), that is a scattering of the electron by the phonon in the solid, can be investigated in HOPG (highly oriented pyro-lytic graphite) [1]. Since HOPG is polycrystalline material, the dispersion of the phonon involved could not be discussed in detail in the previous work. Here, we report the phonon dispersion of the graphite involved in the indirect transition in single-crystalline graphite.

Figure 1(a) presents a series of angle-resolved photoelectron spectra of graphite at 12 K in the region near the Fermi level with the photon energies of 11.1eV, which gives a resonant enhancement in the intensity of step-like edges near 160meV[1]. Here we focus on these step-like edges, which are provided by the energy-shift from the Fermi-edge due to the electron-phonon scattering from the K(A)-point of the Brillouin zone, where the  $\pi$ -band crosses the Fermi level in graphite. The energy of the step, therefore, matches the energy of the phonon that is involved[1]. Two possible scattering geometry when the electron at the K and K' points are scattered into the point on the  $\Gamma$ -K line, along which the ARPES is measured, are displayed in Fig. 1(b). According to these schemes, phonon dispersions along the K'- $\Gamma$ (1) and K-M(2) lines are probed simultaneously in the present case. We applied the least squares method to fit the ARPES data by a phenomenological step-function as

$$f(x) = y_0 + c(X_c - x) + [a(X_c - x) + b] \left[ 1 - \operatorname{erf} \left\{ \frac{(X_c - x)}{\sqrt{2}w} \right\} \right],$$

[shown as grey lines in Fig.1(a)] in order to obtain a value ( $X_c$ ) of an energy for the step with respect to the Fermi level. The results are shown as dots in Fig. 1(c) for two directions of the phonon momentum vector simultaneously. Solid lines are results of GW-calculation for LO (longitudinal optical), LA (longitudinal acoustic), and TO (transverse optical) phonon branches. Dotted line presents that of the LDA-calculation of the TO branch [2]. Note that there are no practical differences reported between GW and LDA calculations for LO and LA branches. It is obvious that only the TO branch calculated with GW-method agrees with the experiments. It is known

that the difference between the LDA and GW calculations is usually caused by the Kohn anomaly, which is due to the electron-phonon coupling in the solid.

An important feature we should point out is the fact that the LO- or LA-phonon branches are not observed here. This indicates that the probability of the indirect transition accompanying with the electron scattering by the LO- and LA- phonons are significantly smaller than that by the TO-phonons. It is difficult to ascribe these to the dipole selection rule, since the  $K_5$  symmetry of the LO and LA-phonons and the  $K_1$  symmetry of the TO phonon cannot be distinguished when the initial state of the indirect transition is the  $K_6$  symmetry as in this case. Therefore, it should be attributed to the difference in the magnitude of the matrix element for the electron-phonon scattering of these phonon modes.

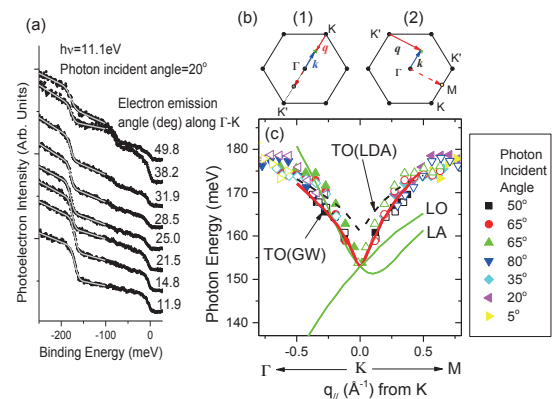


Fig. 1. (a) Angle-resolved photoelectron spectra of single-crystalline graphite. (b) Two possible electron-phonon scattering geometry when the electron at the K and K' points is scattered into the point on the  $\Gamma$ -K line. (c) Phonon dispersion derived from the ARPES (dots), GW-calculation (solid lines) and LDA-calculation (dotted lines)[2].

[1] S. Tanaka, M. Matsunami and S. Kimura, Sci. Rep. 3, 3031; DOI:10.1038/srep03031 (2013).

[2] A. Grüneis *et al.*, Phys. Rev. B. **80** (2009) 085423.

BL7U

## Photoemission Studies on Rashba & Dresselhaus Effect Systems

W. Jung<sup>1</sup>, S. Cho<sup>1</sup>, Y. Kim<sup>1</sup>, B. Kim<sup>1</sup>, Y. Koh<sup>1</sup>,  
J. Seo<sup>1</sup>, M. Matsunami<sup>2</sup>, S. Kimura<sup>2,3</sup> and C. Kim<sup>1</sup>

<sup>1</sup>Institute of Physics and Applied Physics, Yonsei University, Seoul, Korea

<sup>2</sup>UVSOR Facility, Institute for Molecular Science, Okazaki 444-8585, Japan

<sup>3</sup>Graduate School of Frontier Biosciences, Osaka University, Suita 565-0871, Japan

Topological insulators with strong spin-orbit coupling have recently been studied in our group. [1, 2]. We found existence of orbital angular momentum (OAM) through theoretical calculation as well as circular dichroism ARPES experiments. [1, 2] The OAM is found to greatly affect the surface electronic structure. We expect that OAM also greatly affect the electronic structures of semiconductors such as CdTe, InSb and GaAs that possess inversion symmetry breaking (ISB) and resulting electric field.

Semiconductor materials have recently been extensively studied for their spintronic applications. An important example is spin-field-effect transistor (spin-FET) proposed by Datta and Das [3] in the light of controllability of spin precession motion of electrons through the Rashba and Dresselhaus spin-orbit coupling effects. [4, 5, 6]. As we expect OAM in these materials greatly affects the electronic structure, it is also expected that OAM has strong influence on Rashba and Dresselhaus effects, therefore in turn on the spintronic properties.

Compound semiconductors such as InSb, CdTe, GaAs have zinc blende structure with ISB in the bulk. They have three hole bands at the  $\Gamma$ -point (occupied states). They are heavy and light hole bands with  $J=3/2$ , and a split off band with  $J = 1/2$ . The energy splitting ( $\Delta$ ) between  $J=3/2$  and  $1/2$  states due to spin-orbit coupling is the order of hundred meV. To explain this band splitting they normally apply Dresselhaus Hamiltonian. Then the effective one-body Hamiltonian becomes:

$$H = H_0 + H_D$$

$$H_D = \gamma[\sigma_x k_x(k_y^2 - k_z^2) + \text{cyclic permutations}]$$

Here,  $H_D$  is the Hamiltonian for the Dresselhaus effect,  $\sigma$  is Pauli matrix, and  $\gamma$  the material dependent spin-orbit coupling constant. However, we believe it is OAM instead of the spin that determines the energy. Therefore, we expect an OAM pattern similar to a spin pattern. To study the OAM pattern in semiconductors, we have performed circular dichroism ARPES on semiconductors.

CdTe single crystals were purchased as wafers. ARPES measurement was performed at the beam line 7U of UVSOR-III. Samples were cleaved in situ at room temperature and the chamber pressure was

better than  $5 \times 10^{-11}$  Torr. ARPES spectra were acquired with a hemispherical photoelectron analyzer (MBS A-1). We used linearly polarized as well as left and right circularly polarized (LCP and RCP) light with the photon energy in the range of 9–34 eV.

As for the OAM textures, we used circularly polarized light on GaAs, InP, InAs of zinc blende semiconductors. Figure 1 shows so obtained ARPES data. Clear band dispersions are observed. Circular dichroism data (LCP-RCP data) shows complex pattern, implying a complex OAM textures in the material. All these prove that there is significant OAM in the material. This is rather surprising, considering the strong crystal field in the system.

On the other hand, we could not reach the  $\Gamma$ -point with low-energy photons due to the limitation of the beam line in spite of the importance of the  $\Gamma$ -point data. It is expected that three-dimensional bulk band structure of GaAs and InSb should give us new information. Therefore, we will perform the three-dimensional ARPES to obtain the complete bulk electronic structure.

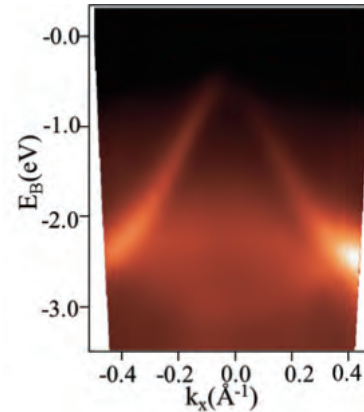


Fig. 1. ARPES results from GaAs (110) bulk state measured with 21 eV photons at the  $\Gamma$ -point.

- [1] S. R. Park *et al.*, PRL **107** (2011) 156803.
- [2] B. Y. Kim *et al.*, PRB **85** (2012) 195402.
- [3] S. Datta *et al.*, Appl. Phys. Lett. **56** (1990) 665.
- [4] Y. A. Bychkov *et al.*, JETP Lett. **39** (1984) 78.
- [5] J. Schliemann *et al.*, PRL. **90** (2003) 146801.
- [6] X. Cartoixa, D *et al.*, APL. **83** (2003) 1462.

BL7U

## Low-Photon-Energy Polarization-Dependent Angle-Resolved Photoemission Study on Quasi-One Dimensional Organic Conductor (TMTSF)<sub>2</sub>SbF<sub>6</sub>

M. Mitamura<sup>1</sup>, T. Hajiri<sup>1,2</sup>, T. Ito<sup>1,3</sup>, S. Kimura<sup>2,4</sup> and T. Nakamura<sup>4,5</sup>

<sup>1</sup> Graduated School of Engineering, Nagoya University, Nagoya 464-8603, Japan

<sup>2</sup> UVSOR Facility, Institute for Molecular Science, Okazaki 444-8585, Japan

<sup>3</sup> Nagoya University Synchrotron Radiation Research Center, Nagoya University, Nagoya 464-8603, Japan

<sup>4</sup> School of Physical Sciences, The Graduate University for Advanced Studies (SOKENDAI), Okazaki 444-8585, Japan

<sup>5</sup> Institute for Molecular Science, Okazaki 444-8585, Japan

The Bechgaard salts (TMTSF)<sub>2</sub>X (where X is one of the anions PF<sub>6</sub>, ClO<sub>4</sub>, etc.) belong to a family of highly anisotropic organic conductors [1]. The quasi-one-dimensional (Q1D) structure of these materials allows for a variety of ground states from a Peierl's-like spin density wave (SDW) insulator to a metallic state, to a superconducting state, as anion and/or pressure are changed [1].

In this study, we have performed polarization dependent angle-resolved photoemission spectroscopy (ARPES) on single-crystalline (TMTSF)<sub>2</sub>SbF<sub>6</sub> to clarify the effects of the Q1D TMTSF molecular chain and the interchain coupling on the electric structure. ARPES measurements were performed at UVSOR-III BL7U by utilizing the bulk-sensitive low photon energy ( $h\nu = 8$  eV) as well as the micro focus beam ( $15 \times 100 \mu\text{m}^2$ ).

Figure 1 (a) and (b) shows the polarization-dependent ARPES images near the Fermi level ( $E_F$ ) along TMTSF-chain direction ( $a$ -axis) measured at  $T = 30$  K with  $p$  ( $E \parallel a$ ) and  $s$  ( $E \perp a$ ) polarized photons, respectively. In Fig. 1 (a), we found a highly-dispersive feature which approaches  $E_F$  around  $k = 0.2 \text{ \AA}^{-1}$ . On the other hand, the dispersive feature becomes intensively weak in Fig. 1 (b). Taking account of the selection rules associated with the  $p$  orbital of TMTSF molecules, initial states with the even- (odd-) symmetry with respect to a mirror plane are selectively observed with  $p$ - ( $s$ -) polarized light. Thus the observed dispersive feature increasing with  $p$ -polarization geometry can be ascribed to the  $p$  orbital which forms the Q1D TMTSF chain along  $a$ -axis.

Figure 2 (a) and (b) shows the angle ( $\theta_{bc}$ ) dependent ARPES spectra near  $E_F$  measured with  $p$  and  $s$  polarized photons, respectively. We found a strong reduction of spectral weight near  $E_F$  as increasing (decreasing)  $\theta_{bc}$  from the normal emission angle ( $\theta_{bc} = 0^\circ$ ) in Fig. 2 (a). Since the mirror plane symmetry of  $p$ -polarization geometry does not change with  $\theta_{bc}$ , the observed reduction might come from the decreasing mean free path for the intrachain  $p$  orbital. On the other hand, the cross section for the interchain orbital will be changed with  $\theta_{bc}$  in  $s$ -polarization geometry. Though the change of the spectral weight

in Fig. 2 (b) is weak, we found slight increase of the spectral weight around 0.3 eV with increasing  $\theta_{bc}$  from  $5^\circ$  to  $-15^\circ$  (see Fig. 3). We expect that the observed change of the spectral weight in Fig.3 is suggestive of the existence of the weak interchain coupling in (TMTSF)<sub>2</sub>SbF<sub>6</sub>. To elucidate the role of the interchain coupling in the anomalous properties, the further study is intended.

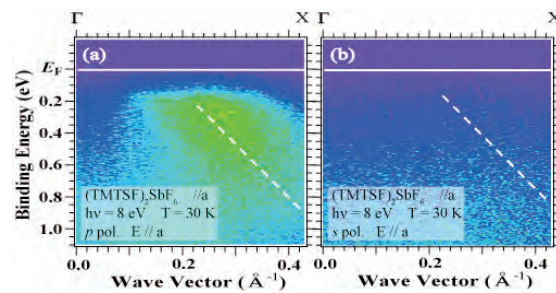


Fig. 1. ARPES images of (TMTSF)<sub>2</sub>SbF<sub>6</sub> along TMTSF-chain direction measured at  $T = 30$  K with  $p$  (a) and  $s$  (b) polarized light. Dashed line is guide for TMTSF band dispersion.

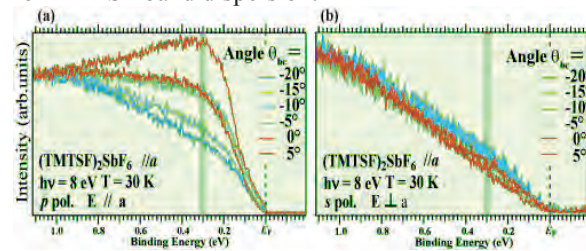


Fig. 2. Interchain angle-dependence of EDC at  $k = k_F$  ( $0.2 \text{ \AA}^{-1}$ ) of (TMTSF)<sub>2</sub>SbF<sub>6</sub> measured at  $T = 30$  K with  $p$  (a) and  $s$  (b) polarized light.

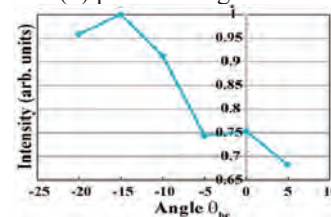


Fig. 3.  $\theta_{bc}$  dependence of the ARPES spectral weight around 0.3 eV in Fig. 2 (b).

[1] T. Ishiguro *et al.*, *Organic Superconductors* (Springer - Verlag, Berlin, 1998).

BL7U

## High-Resolution ARPES Study of SnTe(111): Observation of Two Types of Dirac-Cone Surface States

Y. Tanaka<sup>1</sup>, T. Shoman<sup>1</sup>, K. Nakayama<sup>1</sup>, S. Souma<sup>2</sup>, T. Sato<sup>1</sup>, T. Takahashi<sup>1,2</sup>,  
M. Novak<sup>3</sup>, K. Segawa<sup>3</sup> and Y. Ando<sup>3</sup>

<sup>1</sup>Department of Physics, Tohoku University, Sendai 980-8578, Japan

<sup>2</sup>WPI Research Center, Advanced Institute for Materials Research, Tohoku University, Sendai 980-8577, Japan

<sup>3</sup>Institute of Scientific and Industrial Research, Osaka University, Ibaraki, Osaka 567-0047, Japan

Topological crystalline insulators (TCIs) are a new class of topological materials where an inverted bulk-band gap leads to unusual gapless surface states (SSs) that are protected by point-group symmetries of the crystal, in particular, mirror symmetry [1, 2]. The TCI phase has been experimentally verified on the (001) surface of the narrow-gap semiconductor SnTe, in which characteristic double-Dirac-cone SSs are observed on the projection of the (110) mirror plane [3]. While the existence of topologically protected Dirac-cone SSs is theoretically guaranteed on *any surface containing a mirror plane*, it has not been experimentally verified whether the topological SSs indeed exist on other surface-plane orientations like (111) and how the surface band structure depends on the symmetry of each surface orientation. This point is of crucial importance for understanding the interplay between the crystal symmetry and the topological protection in TCIs.

In this study, we have performed angle-resolved photoemission spectroscopy (ARPES) on the (111) surface of SnTe whose bulk and surface Brillouin zones (BZs) are displayed in Fig. 1(a). By utilizing the high-resolution and variable-photon-energy ( $h\nu$ ) capabilities of the beamline BL7U, we have succeeded in revealing two types of mirror-symmetry-protected Dirac-cone SSs, which originate from the bulk-band inversion at the L points [4].

Figure 1(b) represents Fermi-surface mapping results on the (111) surface of SnTe with  $h\nu = 23$  eV. We identify bright intensity centered at the  $\bar{\Gamma}$  point as well as relatively weak intensity at the  $\bar{M}$  point, which reflects the periodicity of the (111) surface. The observed intensity at  $E_F$  around the  $\bar{\Gamma}$  point originates from a linearly dispersive hole-like band near  $E_F$  as seen from Fig. 1(c). The near- $E_F$  band dispersion [Fig. 1(d)] extracted from the numerical fittings of the MDCs with two Lorentzians reasonably overlaps with each other within the experimental uncertainties irrespective of photon energies. This result strongly suggests the existence of a Dirac-cone SS centered at the  $\bar{\Gamma}$  point. We also found a linearly dispersive hole-like band which crosses  $E_F$  around the  $\bar{M}$  point as displayed in Fig. 1(e). The  $h\nu$  independence in the dispersion [see Fig. 1(f)] demonstrates that the observed linearly dispersive band originates from a Dirac-cone SS centered at  $\bar{M}$ ,

indicating that there exist four Dirac cones in the surface BZ, one centered at  $\bar{\Gamma}$  and three at  $\bar{M}$ . As seen from Fig. 1(a), the (110) mirror plane of the bulk BZ lies along the  $\bar{\Gamma}$ - $\bar{M}$  line of the surface BZ. Since a single L point at which bulk-band inversion takes place is projected onto either the  $\bar{\Gamma}$  or  $\bar{M}$  points, a single Dirac cone is produced centered at those time-reversal-invariant momenta (on the projection of the mirror plane), consistent with the present observation. The present ARPES result on the (111) surface, together with our previous study on the (001) surface [3], establishes an essential role of the crystal mirror symmetry and the bulk-band inversion in realization of the TCI phase.

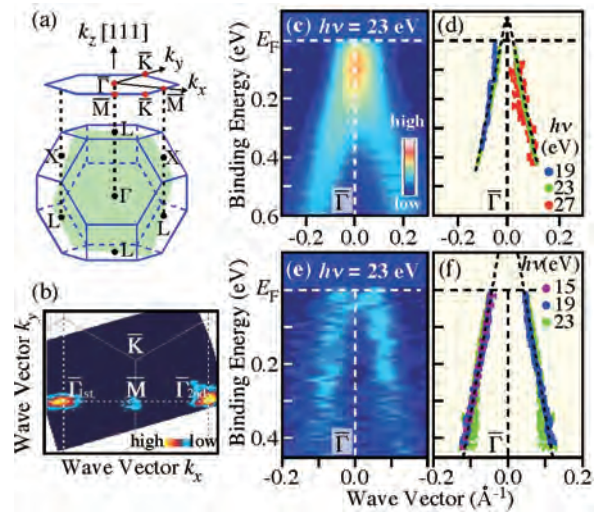


Fig. 1. (a) Bulk fcc BZ and corresponding hexagonal (111) surface BZ of SnTe. Green shaded area represents the (110) mirror plane. (b) ARPES intensity mapping at  $E_F$  at  $T = 30$  K plotted as a function of in-plane wave vector. (c) Intensity plot of the second derivatives of the momentum distribution curves (MDCs) across the cut crossing the  $\bar{\Gamma}$  point for  $h\nu = 23$  eV. (d) Comparison of the band dispersions for different photon energies extracted by fitting the MDCs. (e) and (f) Same as (c) and (d), respectively, but measured along the cut crossing the  $\bar{M}$  point.

- [1] L. Fu, Phys. Rev. Lett. **106** (2011) 106802.
- [2] T. H. Hsieh *et al.*, Nature Commun. **3** (2012) 982.
- [3] Y. Tanaka *et al.*, Nature Phys. **8** (2012) 800.
- [4] Y. Tanaka *et al.*, Phys. Rev. B **88** (2013) 235126.

BL7U

## An ARPES Study of the Electronic Structure of CsBi<sub>4</sub>Te<sub>6</sub>

S. T. Cui<sup>1</sup>, S. Kong<sup>1</sup>, G. B. Zhang<sup>1</sup>, Z. Sun<sup>1</sup>, C. Xiao<sup>2</sup>, Y. Xie<sup>2</sup>, M. Matsunami<sup>3</sup> and S. Kimura<sup>3,4</sup>

<sup>1</sup>National Synchrotron Radiation Laboratory, University of Science and Technology of China, Hefei, Anhui 230029, People's Republic of China

<sup>2</sup>Hefei National Laboratory for Physical Sciences at Microscale, University of Science and Technology of China, Hefei, Anhui 230026, People's Republic of China

<sup>3</sup>UVSOR Facility, Institute for Molecular Science, Okazaki 444-8585, Japan

<sup>4</sup>Graduate School of Frontier Biosciences, Osaka University, Suita 565-0871, Japan

Topological insulators are a new quantum state of matter with gapless surface states inside of the bulk energy gap. (Bi, Sb)<sub>2</sub>(Te, Se)<sub>3</sub> series of compounds have been extensively studied as topological insulators. On the other hand, (Bi, Sb)<sub>2</sub>(Te, Se)<sub>3</sub> series have been widely used as thermoelectric materials. Indeed, the excellent properties of thermoelectric materials are mainly due to the nature of the novel electronic structures of these topological insulators. Thus, it is an interesting topic to search (Bi, Sb)<sub>2</sub>(Te, Se)<sub>3</sub>-derived thermoelectric materials for topological insulators.

CsBi<sub>4</sub>Te<sub>6</sub> is an excellent thermoelectric material [1], with thermoelectric properties better than (Bi, Sb)<sub>2</sub>(Te, Se)<sub>3</sub> at low temperature. Recently, it has also been found that a slight hole-doping can induce superconductivity in this compound [2]. Figure 1 shows the crystal structure of CsBi<sub>4</sub>Te<sub>6</sub>. In this material, the Bi<sub>2</sub>Te<sub>3</sub> framework is reconstructed, so CsBi<sub>4</sub>Te<sub>6</sub> bears no resemblance to the corresponding binary compound. Thus it is important to investigate whether this excellent thermoelectric material can host topological insulating states. Moreover, it is of great interest to study whether the topological insulator states can coexistence with superconductivity in this material.

We performed ARPES experiments on CsBi<sub>4</sub>Te<sub>6</sub> at BL7 of UVSOR at T=30K, with 20 meV energy resolution and 0.5° angular resolution, under an ultrahigh vacuum of 6×10<sup>-11</sup> mbar.

Figure 1 shows the electronic band structure over a large energy scale near the zone center. The band structure calculations show that CsBi<sub>4</sub>Te<sub>6</sub> is a narrow-gap semiconductor [3], while the electrical conductance measurements show that this material bears metallic properties. The inset of Fig. 1(a) exhibits evident spectral weight near the Fermi level, which is consistent with the metallic conductivity in this material [3]. These metallic spectral weight however could arise from the conduction band with slight electron doping.

A close inspection of the near-*E<sub>F</sub>* states can reveal more details of the electronic structure. Figure. 2(b) shows the spectral weight distribution in the yellow frame in Fig. 2(a). It is very interesting that there likely exists Dirac-cone-like spectral weight within

the band gap of this material. Although more experiments should be carried out to reveal the true nature of these states, it is possible that novel electronic states may exist in this thermoelectric material.

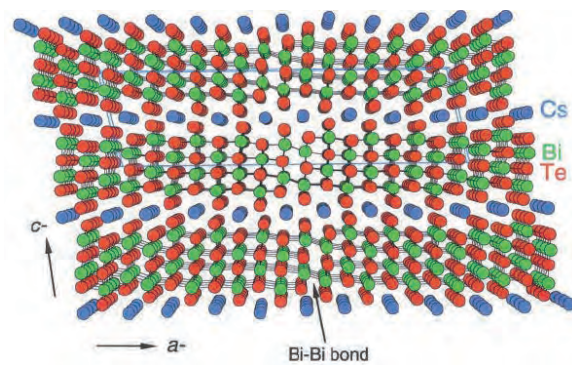


Fig. 1. The crystal structure of CsBi<sub>4</sub>Te<sub>6</sub> looking down the *b* axis.

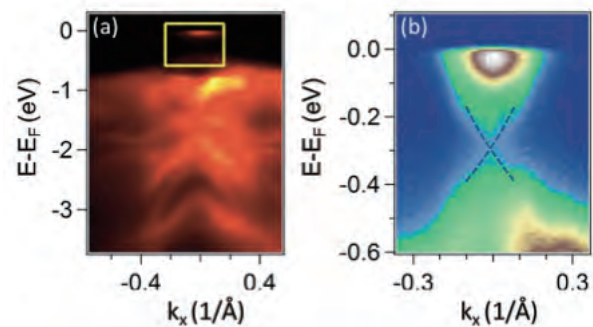


Fig. 2. (a) Band structure of CsBi<sub>4</sub>Te<sub>6</sub>. (b) Near-*E<sub>F</sub>* Dirac-cone-like dispersions, which were taken from the yellow frame in (a).

[1] D. Y. Chung *et al.*, *Science* **287** (2000) 1024.

[2] C. D. Malliakas *et al.*, *J. Am. Chem. Soc.* **135** (2013) 14540.

[3] D. Y. Chung *et al.*, *J. Am. Chem. Soc.* **126** (2004) 6414.

BL7U

## Three-Dimensional Anisotropic Superconducting Gap of Over-Doped $\text{BaFe}_{1.8}\text{Co}_{0.2}\text{As}_2$

 T. Hajiri<sup>1,2</sup>, T. Ito<sup>1,3</sup>, M. Matsunami<sup>2,4</sup>, B. H. Min<sup>5</sup>, Y. S. Kwon<sup>5</sup> and S. Kimura<sup>2,4</sup>
<sup>1</sup>Graduate School of Engineering, Nagoya University, Nagoya 464-8603, Japan

<sup>2</sup>UVSOR Facility, Institute for Molecular Science, Okazaki 444-8585, Japan

<sup>3</sup>Nagoya University Synchrotron Radiation Research Center, Nagoya University, Nagoya, 464-8603, Japan

<sup>4</sup>School of Physical Sciences, The Graduate University for Advanced Studies (SOKENDAI), Okazaki 444-8585, Japan

<sup>5</sup>Department of Emerging Materials Science, DGIST, Daegu 711-873, Republic of Korea

In iron pnictide superconductors, one of the most attractive issues is the position of nodes in the three-dimensional (3D) electronic structures, because the position of nodes is the most important information for the origin of the superconductivity as well as the symmetry of the superconducting (SC) order parameter. Angle-resolved photoemission spectroscopy (ARPES) is one of the most powerful tools to investigate the SC-gap structures. Importantly, the SC-gap structure in the 3D momentum space can be revealed by ARPES using synchrotron radiation. In this report, we show the 3D-ARPES results of the over-doped  $\text{BaFe}_{1.8}\text{Co}_{0.2}\text{As}_2$  ( $T_c \sim 22.5$  K) using UVSOR BL7U “SAMRAI” end-station. In this material, the nodal behavior was reported [1,2].

Figures 1(a) and 1(b) show the out-of-plane electron Fermi surfaces (FSs) in the  $\Gamma\text{MAZ}$  plane and in-plane FSs determined by experiments, respectively. The symmetrized ARPES spectra above  $T_c$  ( $T = 35$  K) and below  $T_c$  ( $T = 12$  K) at several FS angles ( $\theta$ ) measured with the photon energy  $h\nu = 14$  eV are shown in Figs. 1(c) and 1(d). At the outer electron FS in Fig. 1(c), the spectral weight at Fermi level at  $|\theta| = 177.2^\circ$  are suppressed with decreasing temperature, indicating the opening the SC gap. At  $|\theta| = 92.3^\circ$ , however, no temperature dependence appears. In contrast to the outer electron FS, the inner electron FS shows substantially isotropic SC gaps as shown in Fig. 1(d). We summarized the  $\theta$ -dependence of the SC-gap size of both electron FSs around the A and M points in Figs. 1(e) and 1(f), respectively. The only outer electron FS has an anisotropic SC gap with nodes or gap minima around the longer axis of the ellipsoid-shaped FS.

Focusing on the electron FSs at the intermediate region between the M and A points taken at  $h\nu = 19$  eV shown in Figs. 1(g) and 1(h), both electron FSs show substantially isotropic SC gaps. Therefore, the nodes exist only around the longer axis of the ellipsoid-shaped outer electron FS at around the M ( $h\nu = 24$  eV) and A ( $h\nu = 14$  eV) points. Our observation suggests that the appearance of superconductivity of this material originates from not only spin fluctuation but also orbital fluctuation.

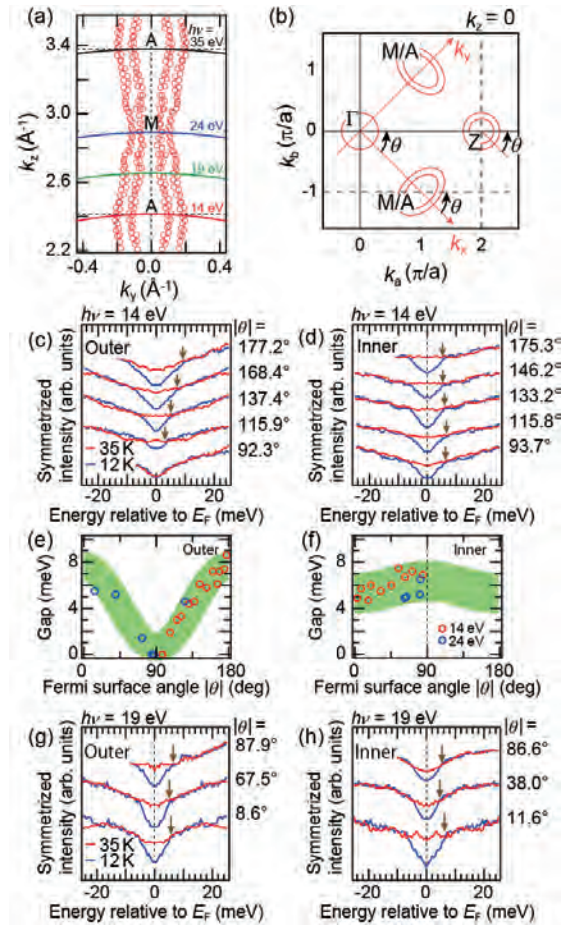


Fig. 1. (a) Out-of-plane electron FSs in the  $\Gamma\text{MAZ}$  plane. (b) Schematic in-plane FSs. (c,d) Symmetrized ARPES spectra taken at  $h\nu = 14$  eV with selected  $\theta$  of the outer and inner electron FSs, respectively. (e,f)  $\theta$ -dependence of the SC-gap size around the M and A points. (g,h) Same as (c,d) but taken at  $h\nu = 19$  eV.

[1] D. -J. Jang *et al.*, New J. Phys. **13** (2011) 023036.

[2] T. Hajiri *et al.*, arXiv:1311.4990 (2013).

BL7U

## Carrier Concentration Dependence of Superconducting Gap in $\text{Bi}_2(\text{Sr,RE})_2\text{CuO}_{6+d}$ (RE = La, Nd, Sm)

H. Sakamoto<sup>1</sup>, A. Yamamoto<sup>1</sup>, M. Matsunami<sup>2</sup>, S. Kimura<sup>2</sup> and T. Takeuchi<sup>1,3,4,5</sup>

<sup>1</sup>Department of Crystalline Materials Science, Nagoya University, Nagoya 464-8603, Japan

<sup>2</sup>UVSOR Facility, Institute for Molecular Science, Okazaki 444-8585, Japan

<sup>3</sup>Ecotopia Science Institute, Nagoya University, Nagoya 464-8603, Japan

<sup>4</sup>Toyota Technological Institute, Nagoya 468-8511, Japan

<sup>5</sup>Promoting Individual Research to Nurture the Seeds of Future Innovation, Japan Science and Technology Agency, Tokyo 102-8666, Japan

The relation between the pseudogap and the stability of superconducting state had been intensively discussed. Some experimental results supported the scenario of the pseudogap as the pre-formed superconducting gap, but many other experiments suggested that the pseudogap developing around the anti-node direction is caused by an unidentified mechanism that is different from the Cooper pair formation and, therefore, prevents the electrons near the anti-nodal region from forming the Cooper pairs. The electrons near the node, on the other hand, are not affected by the pseudogap, and the Bose condensation of the Cooper-pairs still takes places to stabilize the superconducting state.

Despite a huge number of investigations being performed after the discovery of high- $T_c$  cuprate superconductors, the collective excitation leading to the formation of Cooper-pairs has not been fully identified yet. In order to gain deep insight into such collective excitation, it is of great importance to know the temperature-, momentum-, and carrier concentration- dependences of superconducting gap. Unfortunately, however, the pseudogap developing at the underdoped condition has made it difficult to reveal the temperature-, momentum-, and carrier concentration- dependences of superconducting gap.

The relation between the carrier concentration dependence of superconducting gap and the carrier concentration dependence of  $T_c$  especially at the underdoped region, on the other hand, has not been fully investigated yet, because the highly developed pseudogap covers the very wide momentum and the superconducting gap persists only in the limited portion in the vicinity of nodal direction where the energy-width of superconducting gap stays in very small values.

In this study, therefore, we carefully investigated the very small superconducting-gap  $\Delta(\phi) = \Delta_0 \cos \phi$  persisting near the nodal direction ( $\phi = 0$ ) for a series of  $\text{Bi}_2(\text{Sr,RE})_2\text{CuO}_{6+d}$  (RE = La, Nd, Sm) superconductors of various hole-concentrations by means of ultra-high-energy-resolution laser induced ARPES. By additionally employing the synchrotron radiation ARPES measurements at BL7U in UVSOR, we investigated the shape of the Fermi surface and the size of the pseudogap as a function of carrier concentration.

Figure 1 shows the hole concentration dependence of superconducting gap  $\Delta_0$  and  $T_c$  of  $\text{Bi}_2(\text{Sr,RE})_2\text{CuO}_{6+d}$  (RE = La, Nd, Sm) determined by means of ARPES measurements. The pseudogap develops when the rare earth element of small ionic radius is used for the substitute of Sr. The difference in  $T_c$  for the different series of  $\text{Bi}_2(\text{Sr,RE})_2\text{CuO}_{6+d}$  is, therefore, attributed to the development of pseudogap.

The hole-concentration dependence of  $\Delta_0$  shows universal behavior regardless of the rare earth element involved in the samples. It obviously increases with decreasing hole concentration at overdoped region. After becoming maximal at around  $p = 0.23$  holes/Cu, it turns out to be reduced with decreasing hole concentration. The value of  $p = 0.23$  holes/Cu providing maximum  $\Delta_0$  is definitely different from  $p = 0.16$  holes/Cu that has been generally considered for the optimally doped condition.

We should stress, as a consequence of this study, that the formability of Cooper-pair is less sensitive to out-of-plane disordering. It is also very important to find the collective excitation that can strongly affect the energy and momentum of conduction electrons at  $p = 0.23$  holes/Cu.

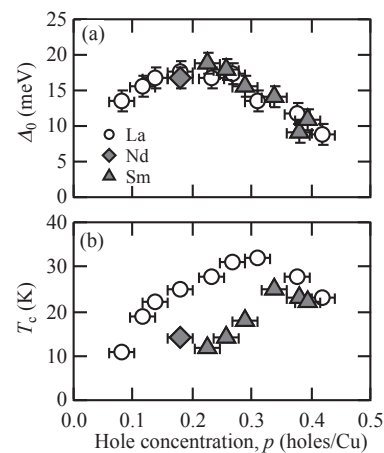


Fig. 1. Hole concentration dependence of (a) superconducting gap  $\Delta_0$  and (b)  $T_c$  of  $\text{Bi}_2(\text{Sr,RE})_2\text{CuO}_{6+d}$  (RE = La, Nd, Sm) determined by means of ARPES measurements and (b) that of.

BL7B

## Electronic Status of Ce<sup>3+</sup> in Glass Host by Characterizing Photoluminescence of Ce<sup>3+</sup> Doped 20Al(PO<sub>3</sub>)<sub>3</sub>-80LiF Glass Scintillator

T. Shimizu<sup>1</sup>, Y. Minami<sup>1</sup>, R. Arita<sup>1</sup>, M. Tsuboi<sup>1</sup>, T. Nakazato<sup>2</sup>, T. Hori<sup>1</sup>,  
K. Fukuda<sup>1</sup>, K. Yamanoi<sup>1</sup>, Y. Shinzato<sup>1</sup>, R. Sogi<sup>1</sup>, N. Sarukura<sup>1</sup>, H. Azechi<sup>1</sup>,  
M. Cadatal-Raduban<sup>3</sup>, T. Murata<sup>4</sup>, S. Fujino<sup>5</sup>, H. Yoshida<sup>6</sup>, T. Suyama<sup>7</sup>, K. Fukuda<sup>7</sup>,  
A. Yoshikawa<sup>8</sup>, N. Sato<sup>9</sup>, H. Kan<sup>9</sup> and K. Kamata<sup>9</sup>

<sup>1</sup>Institute of Laser Engineering, Osaka University, Suita 565-0871, Japan

<sup>2</sup>Research Institute for Science & Technology, Tokyo University of Science, Noda 278-8510, Japan

<sup>3</sup>Centre for Theoretical Chemistry and Physics, Institute of Natural and Mathematical Sciences, Massey University, Albany, Auckland, 0632 New Zealand

<sup>4</sup>Kumamoto University, Kumamoto 860-8555, Japan

<sup>5</sup>Kyushu University, Fukuoka 812-8581, Japan

<sup>6</sup>Ceramic Research Center of Nagasaki, Higashisonogi-gun 859-37, Japan

<sup>7</sup>Hamamatsu Photonics K.K., Hamamatsu 430-8587, Japan

<sup>8</sup>Institute for Materials Research, Tohoku University, Sendai 980-8577, Japan

<sup>9</sup>Furukawa Co. Ltd., Tokyo 100-8370, Japan

The realization of nuclear fusion is highly expected to satisfy the energy demand in the future. Fusion plasma diagnostics at higher plasma areal density than 3 g/cm<sup>2</sup> is one of the biggest breakthrough in nuclear fusion research. Scattered-neutron diagnostics [1] utilizing Pr<sup>3+</sup>-doped 20Al(PO<sub>3</sub>)<sub>3</sub>-80LiF (APLF+Pr) glass scintillator is expected to achieve plasma areal density measurement in fusion core. APLF+Pr, which have high sensitivity for scattered neutrons and fast response time about 5.4 ns, is the key factor of the measure. In addition, recent research indicated that APLF+Ce also have great characteristics as neutron scintillator [2]. In this work, we report the optical properties of APLF+Ce at various temperature for investigation of electronic status of Ce<sup>3+</sup>.

We have measured Photoluminescence (PL) spectra and Photoluminescence Excitation (PLE) spectra of APLF+Ce for 0.5 and 3.0 mol % Ce<sup>3+</sup> concentrations at 30K, 100K, 200K, and 300K. APLF+Ce glass samples which size are 25 mm in diameter and 10 mm in thickness are used. The experiment was conducted at BL7B utilizing G2 grating. Each sample was put inside a vacuum chamber maintained at a vacuum level of 10<sup>-6</sup> Pa and was excited by the synchrotron radiation. An optical fiber was used to guide luminescence from the sample to the spectrometer. The spectrometer consists of a liquid nitrogen-cooled charge coupled device (CCD) camera for PL measurement and a photomultiplier tube (PMT) for PLE measurement. The temperature of samples was controlled by liquid helium cryostat and heater.

The PL spectra of APLF+Ce for 0.5 and 3.0 mol % Ce<sup>3+</sup> concentrations excited by 220 nm radiation at 30 K and 300 K are shown in Fig. 1. The luminescence intensity of both samples remain nearly unaffected by temperature change. The emission peak of APLF+0.5 mol % Ce<sup>3+</sup> was around 330 nm wavelength. On the other hand, one of APLF+3.0 mol % Ce<sup>3+</sup> was around 343 nm wavelength. This difference result from

expanding of 5d bandwidth in Ce<sup>3+</sup> with increasing of Ce<sup>3+</sup> concentration. The PLE spectra of samples, emission wavelength is 331 nm, at various temperature are shown in Fig. 2. Both crystal show broad excitation spectrum and the peak wavelength are around 270 nm.

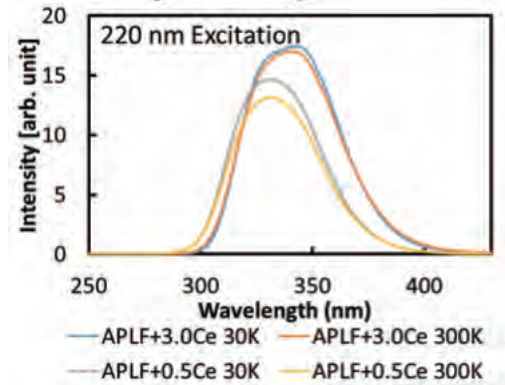


Fig. 1. PL spectra of APLF+Ce.

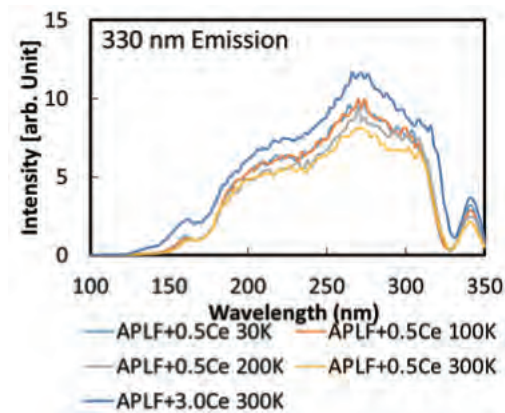


Fig. 2. PLE spectra of APLF+Ce.

[1] M. Moran *et al.*, Rev. Sci. Instrum. **75** (2004) 3592.

[2] IEEE TRANSACTIONS ON NUCLEAR SCIENCE. **59** (2012) 2256.

BL7B

## Reflection Spectra of Ternary Zinc Bismuth Phosphate Glasses in the Ultraviolet Region

N. Kitamura

National Institute of Advanced Industrial Science and Technology, Osaka 563-8577, Japan

Bismuth phosphate glasses, which have high refractive index and low deformation temperature, are candidate materials for producing high performance optical components such as compact lenses and diffractive optics. It is of interest that a zinc bismuth phosphate glass system has two distinct glass-forming regions; orthophosphate and isolated phosphate structures are dominant in the region that the atomic ratio O/P is higher than 3.5 and metaphosphate and pyrophosphate structures are dominant in the region of  $O/P < 3.5$  [1, 2]. We have reported the glass structure and local structure around bismuth ions in a previous work [2, 3]. Absorption edge energy is related to the interconfigurational transition from  $6s^2$  to  $6s^16p^1$  of the  $Bi^{3+}$  ion. However, the energy level in the glass system is not clear yet. In the present study, reflectivity of the bismuth phosphate glasses has been measured to investigate compositional dependence of the band structure in the vacuum ultraviolet region.

Binary  $xBi_2O_3-(100-x)P_2O_5$  glasses ( $x=15, 25$  and  $30$  mol%), ternary  $yZnO-(30-y/2)Bi_2O_3-(70-y/2)P_2O_5$  glasses ( $y=10, 20$  and  $30$  mol%) and  $50ZnO-50P_2O_5$  glass were prepared by using a conventional liquid-quench method. Reflectivity of optically polished samples was measured in the photon energy region of 4-12 eV with an incident angle of  $10^\circ$  at the BL7B. Figure 1 shows reflection spectra of the binary and un-doped ZnO- $P_2O_5$  glass. Distinct reflection peak and broad contour were respectively observed at around 5 eV and 6-8 eV by comparing the spectrum for the undoped ZnO- $P_2O_5$  glass. The peak and contour are assigned to the  $6s^2 \rightarrow 6s^16p^1$  transition in the  $Bi^{3+}$  ion [2, 4]. We know that transitions from the ground state ( $^1S_0$ ) to excited states  $^3P_0$  and  $^3P_2$  are spin-forbidden. Therefore, the lower distinct peak is expected to the  $^1S_0 \rightarrow ^3P_1$  transition and the next contour could be due to the  $^1S_0 \rightarrow ^1P_1$  transition. In the binary  $Bi_2O_3-P_2O_5$  glass system, the distinct peak shifted toward lower energy side with  $Bi_2O_3$  concentration. Moreover, both the band structure tended to broaden with increasing the concentration. It could be due to distortion of  $BiO_6$  tetrahedron which was found in high energy diffraction measurement [5].

On the other hand, reflection spectra of ternary  $yZnO-(30-y/2)Bi_2O_3-(70-y/2)P_2O_5$  glasses are shown in Fig. 2. As shown in the figure, the distinct peak did not shifted with the change of  $Bi_2O_3$  concentration, while the intensity of the band increased with the concentration. It was consistent with that the absorption edge energy was less dependent on the

concentration in the ternary glass system with  $O/P < 3.5$  [2]. The band structure of ternary glass with  $O/P > 3.5$  will be measured in near future.

This work was supported by Nippon Sheet Glass Foundation for Materials Science and Engineering.

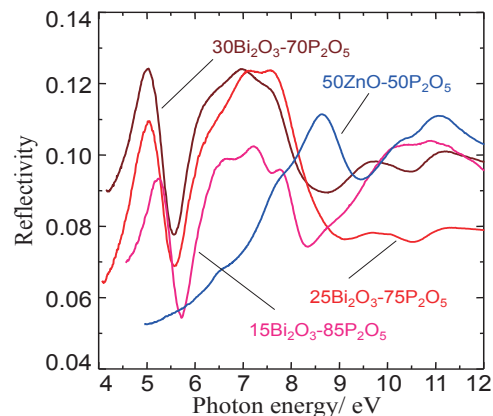


Fig. 1. Reflection spectra of binary  $xBi_2O_3-(100-x)P_2O_5$  and  $ZnO-50P_2O_5$  glasses.

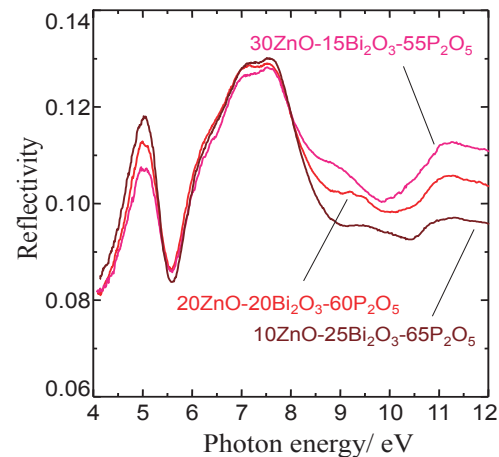


Fig. 2. Reflection spectra of ternary  $yZnO-(30-y/2)Bi_2O_3-(70-y/2)P_2O_5$  glasses.

- [1] B. Elouadi *et al.*, Phase Trans. **13** (1988) 219.
- [2] N. Kitamura, K. Fukumi, J. Nakamura, T. Hidaka, H. Hashima, Y. Mayumi and J. Nishii, Mater. Sci. Eng. B **161** (2009) 91-95.
- [3] N. Kitamura and K. Fukumi, J. Ceram. Soc. Jpn. **121** (2013) 355-360.
- [4] G. Blasse and A. Bril, J. Chem. Phys. **48** (1968) 217-222.
- [5] N. Kitamura, *et al.*, 23th International Congress on Glass 2013, in preparation.

BL7B

## Anomalous Domain-Wall Conductance in Pyrochlore-Type $\text{Nd}_2\text{Ir}_2\text{O}_7$ on the Verge of the Metal-Insulator Transition

J. Fujioka<sup>1</sup>, K. Ueda<sup>1</sup>, Y. Takahashi<sup>1</sup>, T. Suzuki<sup>2</sup>, S. Ishiwata<sup>1</sup>, Y. Taguchi<sup>2</sup>, M. Kawasaki<sup>1,2</sup> and Y. Tokura<sup>1,2</sup>

<sup>1</sup>Department of Applied Physics, University of Tokyo, Tokyo 113-8656, Japan

<sup>2</sup>RIKEN Center for Emergent Matter Science (CEMS), Wako 351-0198, Japan

The topological quantum phase of condensed matter has been of great interest since the discovery of the topological insulator. A spectacular feature of topological insulator is the emergence of the topologically protected surface state, whereas the bulk is characterized by a gapped electronic state. Recently, Wan *et al.* have predicted another class of unconventional topological quantum state, that is, Weyl semimetal (WSM). WSM is a zero gap semiconductor(semimetal) which is characterized by the  $k$ -linearly dispersing bands near the Fermi energy and by the emergence of topologically-protected edge state at the sample surface.

Pyrochlore-type  $R_2\text{Ir}_2\text{O}_7$  ( $R$  = trivalent rare-earth or Y ion) has attracted much attention since it is one of the promising candidates for the realization of WSM due to the interplay between electron correlation and strong spin-orbit coupling inherent to heavy  $5d$  elements. Among a series of  $R_2\text{Ir}_2\text{O}_7$ ,  $R = \text{Nd}$  undergoes metal-insulator transition accompanying with all-in all-out type magnetic ordering at  $T_N = 32$  K, where all the spins on the vertices of tetrahedron point either inwards or outwards to its center. Recent study suggests that its ground state could be a Mott insulator in vicinity to WSM [2]. In order to characterize this unconventional phase, the observation of edge state at sample surface or magnetic domain wall (DW) is essential.

In this article, we report the spectroscopic observation of metallic state at antiferromagnetic DW in  $\text{Nd}_2\text{Ir}_2\text{O}_7$  [3]. The antiferromagnetic DW shows Drude-like optical response with minimal damping constant of  $\sim 2$  meV, contrary to the fully-gapped electronic structure in bulk.

We measured reflectivity spectra for polycrystals of  $\text{Nd}_2\text{Ir}_2\text{O}_7$  between 12 meV and 5 eV using Fourier-transform spectrometer and grating-type spectrometer in temperature range between 5 K and 290 K. We obtained the reflectivity between 5 and 40 eV at room temperature by using synchrotron radiation at BL7B in UVSOR. We determined complex optical constants through the Kramers-Kronig transformation with proper extrapolations of reflectivity in the low and high energy regions. We also obtained the optical conductivity spectra below 8 meV by the terahertz time-domain spectroscopy in a transmission configuration.

Figure 1 (a) shows the reflectivity spectra up to 40

eV. Below  $T_N$ , the reflectivity in low energy region is significantly suppressed, indicative of the opening of the charge gap. Figure 1 (b) shows the real parts of the optical conductivity spectra below 8 meV at 4 K. Here, the black solid line denotes the conductivity for multi-domain state [ $\sigma_{\text{ut}}'(\omega)$ ] obtained at 0 T after cooling under zero magnetic field(untrained state), whereas the red one denotes the spectra for single-domain state [ $\sigma_{\text{t}}'(\omega)$ ] obtained at 0 T once the field applied(trained state).  $\sigma_{\text{ut}}'(\omega)$  shows Drude response below 4 meV, whereas  $\sigma_{\text{t}}'(\omega)$  monotonically decreases as lowering energy. In order to examine the charge dynamics of DW in more detail, we have deduced the real ( $\Delta\sigma'(\omega) = \sigma_{\text{ut}}'(\omega) - \sigma_{\text{t}}'(\omega)$ ) and imaginary ( $\Delta\sigma''(\omega) = \sigma_{\text{ut}}''(\omega) - \sigma_{\text{t}}''(\omega)$ ) part of the DW optical conductivity spectra. Figure 1 (c) shows  $\Delta\sigma'(\omega)$  (red solid line) and  $\Delta\sigma''(\omega)$  (blue solid one). The broken lines corresponds to fitting 1 curve with Drude model with scattering rate of 2 meV, indicating that highly metallic state is realized at the magnetic DW. Such anomalous DW conductance could be relevant with the topological edge state relevant to WSM

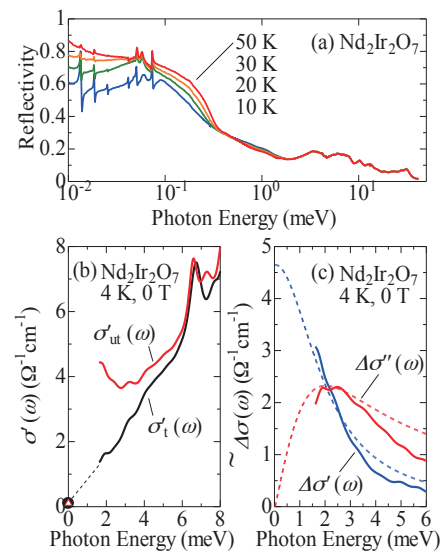


Fig. 1. (a) Reflectivity and (b) (c) optical conductivity spectra for  $\text{Nd}_2\text{Ir}_2\text{O}_7$  at various temperatures.

[1] X. Wan *et al.*, Phys. Rev. B **83** (2011) 205101.

[2] K. Ueda *et al.*, Phys. Rev. Lett. **109** (2012) 136402.

[3] K. Ueda *et al.*, Phys. Rev. B **89** (2014) 075127.

BL7B, BL8B

## Measurement of Transmittance and Reflectance of $\text{LiTi}_2\text{O}_4$ and UPS Measurement of Multi-Alkali Surface

R. Inagaki<sup>1,2</sup>, T. Konomi<sup>2</sup>, T. Tokushi<sup>2</sup>, M. Katoh<sup>2</sup>, E. Kako<sup>3</sup>, S. Yamaguchi<sup>3</sup>, Y. Kobayashi<sup>3</sup>,  
N. Yamamoto<sup>4</sup>, M. Hosaka<sup>4</sup>, Y. Takashima<sup>4</sup>, S. Shiraki<sup>5</sup>, T. Hitosugi<sup>5</sup>, K. K. Rasika<sup>6</sup>  
and Y. Okano<sup>7</sup>

<sup>1</sup>Graduate School of Engineering, Nagoya University, Nagoya 464-8603, Japan

<sup>2</sup>UVSOR facility, Institute for Molecular Science, Okazaki 444-8585, Japan

<sup>3</sup>High Energy Accelerator Research Organization, KEK, Tsukuba, 305-0801, Japan

<sup>4</sup>Nagoya University Synchrotron radiation Research center, Nagoya 464-8603, Japan

<sup>5</sup>WPI-AIMR, Tohoku University, Sendai 980-8577, Japan

<sup>6</sup>Graduate School of Advanced Integration Science, Chiba 263-8522, Japan

<sup>7</sup>Laser center, Institute for Molecular Science, Okazaki 444-8585, Japan

In UVSOR, a VUV free electron laser based on superconducting linear accelerator with high pulse repetition about 1MHz is being designed for the next generation light sources. We are developing an electron gun for the new accelerator by combining superconducting RF cavity and photocathode. We propose a back-illuminated multi-alkali photocathode with transparent superconductor  $\text{LiTi}_2\text{O}_4$  [1]. We consider that to clarify the transmittance / reflectance of the substrate and deposition state of multi-alkali is important in making the photocathode.

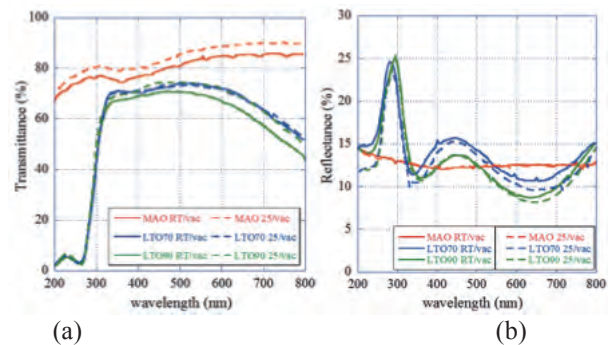
In this study we measured the transmittance and reflectance of  $\text{LiTi}_2\text{O}_4$  in R.T. and 25.5K at BL7B, UVSOR-III. Furthermore, we performed a Ultraviolet Photoelectron Spectroscopy of gold surface was deposited multi-alkali ( $\text{K}_2\text{CsSb}$ ) at BL8B, UVSOR-III to elucidate the bonding state of alkali metal atoms in the course of deposition.

Figure 1(a) shows a transmittance of  $\text{LiTi}_2\text{O}_4$  of 70nm and 90nm thickness at R.T. and 25.5K. Figure 1(b) shows a reflectance of  $\text{LiTi}_2\text{O}_4$  of 70nm and 90nm thickness at R.T. and 25.5K. The transmittance at R.T. is about 70% in the range of 350nm and 600nm. These results are consistent with the measurement results at Tohoku University [2]. At 25.5K, the transmittance of only substrate ( $\text{MgAl}_2\text{O}_4$ ) was higher than that of at R.T. in all measurement wavelength range but transmittance and reflectance of  $\text{LiTi}_2\text{O}_4$  did not change significantly.

Figure 2 shows a spectrum of Au surface deposited  $\text{K}_2\text{CsSb}$ . The results suggests that three alkali metals were not compounded, it was only stacked. This is because the substrate temperature during the deposition was lower than the bonding temperature.

We plan to measure the transmittance and reflectance below superconducting transition temperature (<12K) and to perform a UPS in the actual deposition condition.

We are grateful to T. Hitosugi and S. Shiraki, WPI-AIMR Tohoku Univ. for provision of  $\text{LiTi}_2\text{O}_4$  samples.



(a) (b)  
Fig. 1. (a) Transmittance comparison of 70nm and 90nm thickness of  $\text{LiTi}_2\text{O}_4$  at R.T. and 25.5K (b) Reflectance comparison of 70nm and 90nm thickness of  $\text{LiTi}_2\text{O}_4$  at R.T. and 25.5K.

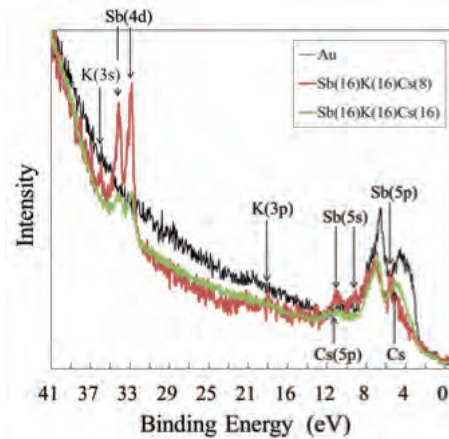


Fig. 2. Spectrum of Au surface was deposited K, Cs and Sb. (Black; Spectrum of Au, Red; Spectrum of surface deposited Sb: 16nm, K: 16nm and Cs: 8nm, Green; Spectrum of surface deposited Cs: 8nm on the sample of the red line)

[1] T. Hitosugi, N. Yamada, S. Nakao, Y. Hirose, and T. Hasegawa, Phys. Status Solidi A 207, No.7, 1529-1537 (2010).

[2] A. Kumatani, T. Ohsawa, R. Shimizu, Y. Takagi, S. Shiraki *et al.*, Appl Phys. Lett. **101** (2012) 123103.

BL7B

## Ultraviolet Photoluminescence of Gd<sup>3+</sup> in Inorganic Materials under Vacuum Ultraviolet Excitation

K. Ueda<sup>1</sup>, Y. Shimizu<sup>1</sup>, Y. Taira<sup>2</sup> and Y. Inaguma<sup>2</sup>

<sup>1</sup> Department of Materials Science, Graduate school of Engineering, Kyushu Institute of Technology, Kitakyushu 804-8550, Japan

<sup>2</sup> Department of Chemistry, Faculty of Science, Gakushuin University, Tokyo 171-8588, Japan

Several ions such as Gd<sup>3+</sup>, Ce<sup>3+</sup>, Pb<sup>2+</sup>, Bi<sup>3+</sup> and Eu<sup>2+</sup> are known as UV luminescent centers. Among them, only the Gd<sup>3+</sup> emission center gives a sharp emission peak at approximately 310 nm in UV-B region. The sharp emission, which is attributed to the inner shell 4f–4f transition from <sup>6</sup>P<sub>1</sub> to <sup>8</sup>S<sub>7/2</sub> in the Gd<sup>3+</sup> ions, can be used as a light source for not only lighting application but also medical application such as phototherapy for skin disease [1], transillumination for DNA analysis [2]. Because Gd<sup>3+</sup> doped phosphors usually have large band gaps in the VUV region, efficient UV emission from doped Gd<sup>3+</sup> ions necessitates intense VUV excitation. In this study, Gd<sup>3+</sup> doped YAlO<sub>3</sub> were prepared and the fundamental UV photoluminescence (PL) properties were investigated by VUV excitation.

The polycrystalline samples of (Y<sub>1-x</sub>Gd<sub>x</sub>)AlO<sub>3</sub> (x=0.00-0.30) were prepared by a polymerized complex method, using Y<sub>2</sub>O<sub>3</sub>, Gd<sub>2</sub>O<sub>3</sub>, Gd(NO<sub>3</sub>)<sub>3</sub>·6H<sub>2</sub>O, Al(NO<sub>3</sub>)<sub>3</sub>·9H<sub>2</sub>O as starting materials. Citric acid monohydrate and propylene glycol (PG) were used to form the polymerized complex gels. The sample powders were obtained by heating at 1400 °C in air. The obtained powders were pressed into pellets and sintered at 1400 °C in air. The phases in the samples were identified by the powder X-ray diffraction (XRD) using a Rigaku RINT 2100 diffractometer (CuKα radiation). The emission and excitation spectra were measured in the beamline BL7B at the UVSOR facility.

Each sample was identified as a distorted perovskite type phase with a space group Pnma. Because the unit cell volumes increased with Gd<sup>3+</sup> concentration x, it was confirmed that Gd<sup>3+</sup> was dissolved into the host lattices. Figure 1 shows PL spectra observed in (Y<sub>1-x</sub>Gd<sub>x</sub>)AlO<sub>3</sub> at room temperature along with the excitation energies for host lattice as a function of x. All samples showed Gd<sup>3+</sup> emission peaks at 314 nm originating from <sup>6</sup>P<sub>7/2</sub> to <sup>8</sup>S<sub>7/2</sub> transition. The maximum PL intensity was observed at x=0.03 and concentration quenching occurred above x=0.03. The excitation energies for host lattices, that gave the maximum PL intensity, decreased with increasing x.

Figure 2 shows PL excitation spectra of (Y<sub>1-x</sub>Gd<sub>x</sub>)AlO<sub>3</sub>. Intense peaks, that were assignable to host excitation, were observed in the wavelength range from 150 to 180 nm. The variation of the wavelength probably indicates the decrease in the band gaps of the host materials. Although shoulder peaks were observed at 120 nm and 200 nm, their

origins are unknown at the present time.

Consequently, (Y<sub>1-x</sub>Gd<sub>x</sub>)AlO<sub>3</sub> was found to exhibit intense Gd<sup>3+</sup> UV emission and showed promise as a UV phosphor upon VUV excitation.

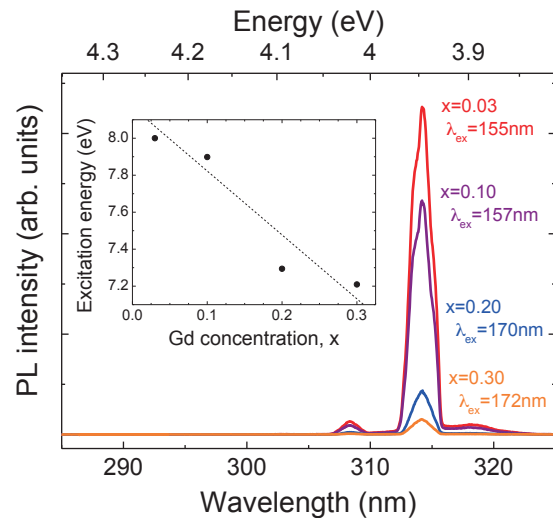


Fig. 1. Gd<sup>3+</sup> photoluminescence spectra in (Y<sub>1-x</sub>Gd<sub>x</sub>)AlO<sub>3</sub>. Inset shows excitation energies for host lattices as a function of x.

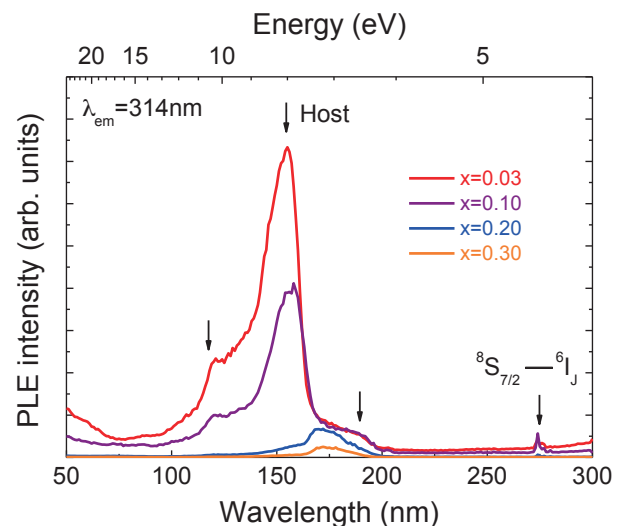


Fig. 2. PL excitation spectra of (Y<sub>1-x</sub>Gd<sub>x</sub>)AlO<sub>3</sub>.

[1] R. P. Sonekar, S. K. Omanwar, S. V. Moharil, S. M. Dhopte, P. L. Muthal and V. K. Kondawar, *Opt. Mater.* **30** (2007) 622.

[2] S. Okamoto, R. Uchino, K. Kobayashi and H. Yamamoto, *J. Appl. Phys.* **106** (2009) 013522.

BL7B

## Scintillation and Luminescence Properties of a Single CsCaCl<sub>3</sub> Crystal

M. Koshimizu<sup>1</sup>, N. Yahaba<sup>1</sup>, R. Haruki<sup>2</sup>, F. Nishikido<sup>3</sup>, S. Kishimoto<sup>4</sup> and K. Asai<sup>1</sup>

<sup>1</sup> *Department of Applied Chemistry, Graduate School of Engineering, Tohoku University, Sendai 9800-8579, Japan*

<sup>2</sup> *Advanced Science Research Center, Japan Atomic Energy Agency, Ibaraki 319-1195, Japan*

<sup>3</sup> *Molecular Imaging Center, National Institute of Radiological Sciences, Chiba 263-8555, Japan*

<sup>4</sup> *Institute of Materials Structure Science, High Energy Accelerator Research Organization, Tsukuba 305-0801, Japan*

Auger-free luminescence (AFL), or core-valence luminescence, is a radiative electronic transition between the valence band and the outermost core band. This luminescence is observed only for insulator crystals in which the band-gap energy is larger than the energy difference between the valence band and the outermost core band. AFL is known to be a fast luminescence process whose decay time constant is typically of the order of nanoseconds or less. Therefore, insulator materials that exhibit AFL are applicable as to fast-response scintillators.

Thus far, BaF<sub>2</sub> has been the most successful example of scintillators exhibiting AFL. Its scintillation has a fast component corresponding to AFL, whose decay time constant is as short as 0.8 ns [1]. Owing to this fast decay combined with relatively high light yields, BaF<sub>2</sub> has been used for applications in which good timing characteristics are necessary. However, its scintillation also has a long decay component corresponding to self-trapped excitons (STEs). The decay time constant of the long component has been reported to be 600 ns [1]. Thus, the long component limits the usage of BaF<sub>2</sub> in several applications, such as measurements with a high counting rate. AFL has also been observed in other binary halide crystals.

In this paper, we report the scintillation properties of a ternary halide crystal, CsCaCl<sub>3</sub>. The origin of the scintillation is discussed on the basis of the luminescence characteristics under VUV irradiation.

Figure 1 shows the luminescence time profiles for excitation at 84 and 200 nm. For the excitation at 84 nm, we observed fast luminescence decay in the entire range of the broad band at 300 nm, and Fig. 1 illustrates the time profiles at short- and long-wavelength regions of the band. The decay time constant was estimated to be 2.3 ns, which is consistent with the result reported in a previous paper [2].

Figure 2 shows the scintillation time profile of CsCaCl<sub>3</sub>. The decay behavior was satisfactorily fitted with a sum of two exponential-decay components and a time-independent component. The fast component had a decay time constant of 2.3 ns, which is consistent with that of the luminescence shown in Fig. 1. Thus, a fast scintillation component due to AFL was successfully obtained. The fast component accounts for 58% of the total scintillation. The slow component had a decay time constant of 14 ns, and

this component accounts for only 4% of the scintillation. The time-independent component accounts for 38%, and this component is considered to have a decay time constant much longer than 624 ns, which is the period of the successive X-ray pulses. The components having a long decay time constant are presumably ascribed to the luminescence at defects or impurities and STE emission.

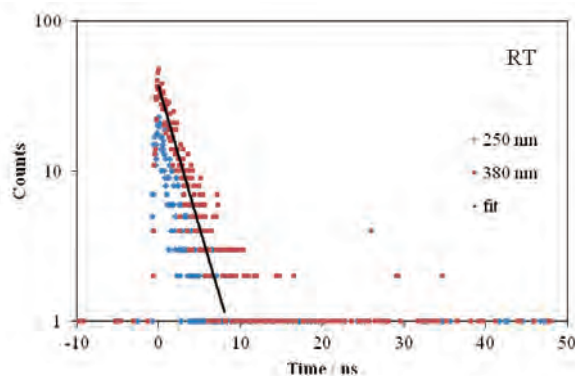


Fig. 1. Luminescence time profiles of CsCaCl<sub>3</sub> under irradiation of VUV photons at 88 nm.

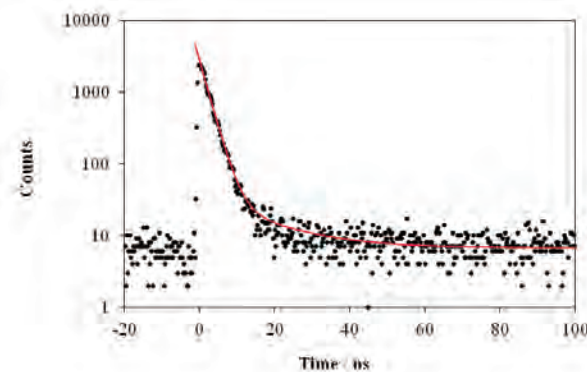


Fig. 2. Scintillation time profile of CsCaCl<sub>3</sub>.

[1] M. Laval, *et al.*, Nucl. Instrum. Methods **206** (1983) 169.

[2] I. A. Kamenskikh, *et al.*, Rev. Sci. Instrum. **63** (1992) 1447.

BL7B

## Insulator-to-Metal Transition of $\text{Sm}_{1-x}\text{Y}_x\text{S}$

K. Imura<sup>1</sup>, M. Saito<sup>1</sup>, M. Matsunami<sup>2,3</sup>, H. S. Suzuki<sup>4</sup>, S. Kimura<sup>2,3</sup> and N. K. Sato<sup>1</sup>

<sup>1</sup>Department of physics, Graduate School of Science, Nagoya University, Nagoya 464-8602, Japan

<sup>2</sup>UVSOR Facility, Institute for Molecular Science, Okazaki 444-8585, Japan

<sup>3</sup>School of Physical Sciences, The Graduate University for Advanced Studies, Okazaki 444-8585, Japan

<sup>4</sup>Nuclear Scattering Group, National Institute for Materials Science, Tsukuba 305-0047, Japan

Samarium monosulfide ( $\text{SmS}$ ) is a prototypical compound that exhibits a phase transition by applying external pressure. This phase transition is accompanied by a color change from black to golden-yellow, namely black-to-golden (BG) transition [1]. It is well known that the electrical resistivity shows an energy gap of about  $E_g \sim 0.1$  eV at ambient pressure. Although this energy gap decreases as increasing pressure, it is still unsolved how energy gap changes in the vicinity of the critical pressure of the BG transition.

In order to study an electronic structure as well as a mechanism of this phase transition, angle resolved photoemission spectroscopy or optical conductivity measurements are powerful techniques. However, pressure studies are very difficult for these experiments.

On the other hand, it has been reported that the BG transition is also induced by site substitution [2]. Then we focused onto the  $\text{Sm}_{1-x}\text{Y}_x\text{S}$  system and performed optical conductivity measurement in order to reveal the relationship between the insulator to metal transition and the BG transition.

A detailed description of single crystal growth of  $\text{Sm}_{1-x}\text{Y}_x\text{S}$  ( $x = 0, 0.17, 0.33$ ) was shown in elsewhere [3]. The reflectivity measurement in the vacuum-ultraviolet, ultraviolet and visible region i.e., the photon energy region of 1.2-25 eV, was performed at the BL7B which consists of a 3-m normal incidence monochromator. The optical conductivity spectra were obtained from the Kramers-Kronig (KK) analysis of the reflectivity spectra.

The BG transition of  $\text{Sm}_{1-x}\text{Y}_x\text{S}$  is observed in the vicinity of  $x = 0.17$ . Figure 1 shows photon energy dependence of the reflectivity spectra [ $R(\omega)$ ] of  $x = 0$  (black color), 0.17 (black color) and 0.33 (gold color) at room temperature. The reflectivity in the infrared region of  $x = 0$  is low in the whole energy region excepting a sharp reflection at  $\hbar\omega \sim 23$  meV due to an optical phonon, reflecting an insulating behavior of pure  $\text{SmS}$ . At  $x = 0.17$ , however, a large reflectivity is observed although the system is still in black phase. The plasma edge of  $x = 0.33$  is located at higher energy than  $x = 0.17$  reflecting an increasing of carrier density.

Figure 2 shows the optical conductivity [ $\sigma(\omega)$ ] as a function of photon energy calculated using the KK transformation from the reflectivity spectra. Closed circles show the DC conductivity values. The Drude

structure is clearly observed at  $x = 0.17$  and 0.33, and the systems show metallic behavior. These results indicate that the insulator-to-metal transition is not a trigger of the BG transition of Y-substituted  $\text{SmS}$ .

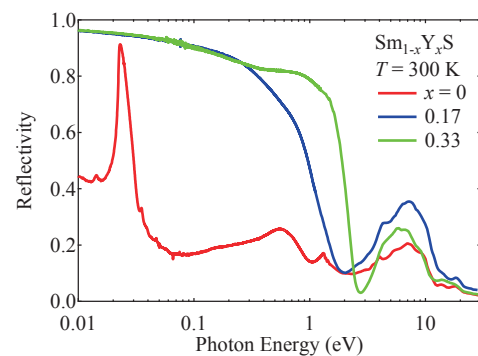


Fig. 1. The reflectivity spectra as a function of photon energy of  $\text{Sm}_{1-x}\text{Y}_x\text{S}$  ( $x = 0, 0.17, 0.33$ ) at  $T = 300$  K.

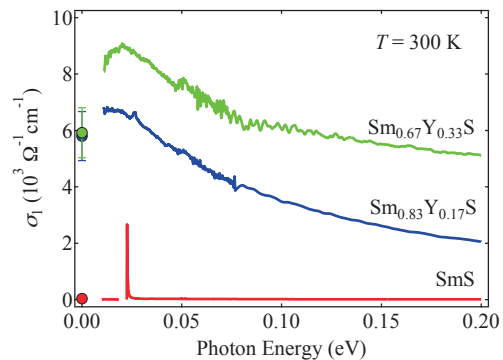


Fig. 2. Photon energy dependence of the optical conductivity calculated using the Kramers - Kronig transformation. Closed circles show DC conductivity value obtained from the conventional 4 probe method.

[1] P. Wachter, *In Handbook on the Physics and Chemistry of Rare Earth* (North-Holland, 1994) **19** (1994) 383.

[2] T. Penny and F. Holtzberg, *Phys. Rev. Lett.* **34** (1975) 322.

[3] K. Imura, T. Hajiri, M. Matsunami, S. Kimura, M. Kaneko, T. Ito, Y. Nishi, N. K. Sato and H. S. Suzuki, *J. Korean Phys. Soc.* **62** (2013) 2028.

BL7B

## Anomalous Energy Transfer Route from $Gd^{3+}$ to $Ce^{3+}$ Ions in $Ce:Gd_3Al_2Ga_3O_{12}$ Crystals

A. Sato<sup>1</sup>, M. Kitaura<sup>1</sup>, S. Kurosawa<sup>2,3</sup>, K. Kamada<sup>3</sup>, A. Ohnishi<sup>1</sup>, M. Sasaki<sup>1</sup> and K. Hara<sup>4</sup>

<sup>1</sup>Department of Physics, Faculty of Science, Yamagata University, Yamagata 990-8560, Japan

<sup>2</sup>Institute for Materials Research, Tohoku University, Sendai 980-8577, Japan

<sup>3</sup>New Industry Creation Hatchery Center, Tohoku University, Sendai 980-8579, Japan

<sup>4</sup>Research Institute for Electronics, Shizuoka University, Hamamatsu 432-8011, Japan

It is well known that the addition of  $Gd^{3+}$  ions works effectively for an enhancement of  $Ce^{3+}$   $5d-4f$  emission in inorganic phosphors [1]. The fundamental process is elucidated by the energy transfer from  $Gd^{3+}$  to  $Ce^{3+}$  ions ( $Gd^{3+} \rightarrow Ce^{3+}$  energy transfer). The spectral overlap between the  $Gd^{3+}$   $4f-4f$  emission and  $Ce^{3+}$   $4f-5d$  absorption bands are necessary for the  $Gd^{3+} \rightarrow Ce^{3+}$  energy transfer, and the route is usually opened from the lowest energy ( $4f$ )<sup>7</sup> excited state of the  $Gd^{3+}$  ion to the ( $5d$ )<sup>1</sup> excited state of the  $Ce^{3+}$  ion. Beside the spectral overlap, an appearance of phosphorescence in the  $Ce^{3+}$   $5d-4f$  emission is also worthwhile to note. The  $Gd^{3+}$   $4f-4f$  emission is electric-dipole forbidden, while the  $Ce^{3+}$   $5d-4f$  emission is electric-dipole allowed. When the  $Ce^{3+}$   $4f-5d$  excitation occurs through the energy transfer from the  $Gd^{3+}$  ion excited, the decay curve for the  $Ce^{3+}$   $5d-4f$  emission ranges from  $\mu s$  to  $ms$ .

The Ce-doped  $Gd_3Al_2Ga_3O_{12}$  (Ce:GAGG) crystal attracts much attention as an inorganic scintillator for the detection of X- and  $\gamma$ -rays [2]. So far, we have investigated photoluminescence (PL) properties of Ce:GAGG crystals at the BL3B beamline of UVSOR [3, 4]. The PL-excitation (PLE) spectra for the  $Ce^{3+}$   $5d-4f$  emission exhibited narrow peaks around 4 and 4.5 eV, which are due to  $Gd^{3+}$   $4f-4f$  absorption. This fact suggests that the  $Gd^{3+} \rightarrow Ce^{3+}$  energy transfer process occurs in Ce:GAGG. This process is supported by the existence of phosphorescence in the decay curve for the  $Ce^{3+}$   $5d-4f$  emission.

In the present study, we have found an anomalous  $Gd^{3+} \rightarrow Ce^{3+}$  energy transfer route in Ce:GAGG crystals under the single bunch operation of UVSOR. Figure 1(a) demonstrates that a fast rise component with the lifetime of dozens of nanosecond appears in only the decay curve for  $Ce^{3+}$   $4f-5d$  emission measured under excitation in the  $Gd^{3+}$   $4f-4f$  absorption around 4.5 eV. This component was not observed under excitation in the  $Ce^{3+}$   $4f-5d$  absorption (Fig. 1(b)) and host GAGG absorption (Fig. 1(c)). Furthermore, it was confirmed that the fast rise does not appear under excitation in the  $Gd^{3+}$   $4f-4f$  absorption around 4 eV. Therefore, it is most likely that the fast rise component is caused by the excitation in  $Gd^{3+}$   $4f-4f$  absorption around 4.5 eV. Details of such an anomalous energy transfer route are unknown at present, so we are analyzing the route using the Dieke diagram.

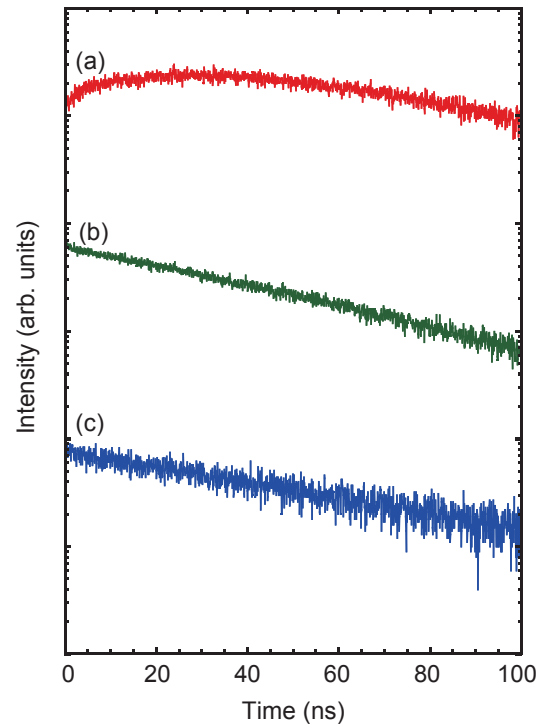


Fig. 1. Decay curves for the  $Ce^{3+}$   $5d-4f$  emission from the Ce:GAGG crystal, which were measured at 11 K under excitation at 4.5 eV (a), 3 eV (b) and 6.5 eV (c). The concentration of  $Ce^{3+}$  ion was 1.5 mol%. The decay curves were vertically shifted for clarity.

- [1] M. Nikl *et al.*, Appl. Phys. Lett., **77** (2000) 2159.
- [2] K. Kamada *et al.*, J. Cryst. Growth **352** (2012) 88.
- [3] M. Kitaura *et al.*, J. Appl. Phys. **115** (2014) 083517.
- [4] A. Satoh *et al.*, Jpn. J. Appl. Phys. (in press).

# UVSOR User 3

